

STUDIES OF THE INFLUENCE, AND ITS CONTROL, OF GRAIN BOUNDARIES
ON MINORITY-CARRIER TRANSPORT IN POLYSILICON DEVICES

By

RAVISHANKAR SUNDARESAN

A DISSERTATION PRESENTED TO THE GRADUATE SCHOOL
OF THE UNIVERSITY OF FLORIDA IN
PARTIAL FULFILLMENT OF THE REQUIREMENTS
FOR THE DEGREE OF DOCTOR OF PHILOSOPHY

UNIVERSITY OF FLORIDA

1983

To my parents

ACKNOWLEDGMENTS

I express my sincere gratitude to the chairman of my supervisory committee, Dr. Jerry G. Fossum, for his expert guidance and encouragement. His research insight into semiconductor device physics combined with superb tutoring has been of immense value in developing my interests. I also express my gratitude to the co-chairman of my supervisory committee, Dr. Dorothea E. Burk, for her guidance and encouragement. I gratefully acknowledge her assistance and cooperation in acquiring my experimental data.

I am thankful to the members of my supervisory committee, Drs. Paul H. Holloway, Fredrik A. Lindholm, Arnost Neugroschel, and Arun K. Varma, for stimulating discussions and for their participation on my committee.

I express my appreciation to Bill Axson, James Chamblee, Bruce Chovnick, Victor de la Torre, Jerry Goeke, E. J. Jenkins, Donna Ray, and Bruce Rushing for their technical assistance and cooperation. I am thankful to my colleagues, Franklin Gonzalez, Bor-Yuan Hwang, Dersun Lee, and Adelmo Ortiz, for useful discussions.

I am grateful to my friends, Ashok, Bhaskar, Chaiti, Gautam, Kumar, Liley, Shiv, Tiru, and Vishu, for their moral support. I am indebted to my brothers for their constant encouragement and continued support throughout my graduate study.

The financial support of the Solar Energy Research Institute is gratefully acknowledged.

I commend my typist, Carole Boone, on her excellent work.

TABLE OF CONTENTS

	PAGE
ACKNOWLEDGEMENTS.....	iii
ABSTRACT	vi
CHAPTER	
1 INTRODUCTION.....	1
2 ANALYSIS OF MINORITY CARRIER TRANSPORT IN POLYSILICON DEVICES.....	9
2.1 Introduction.....	9
2.2 Analysis.....	14
2.3 Discussion.....	48
3 DETERMINATION OF GRAIN-BOUNDARY RECOMBINATION VELOCITY FROM ELECTRON-BEAM-INDUCED-CURRENT MEASUREMENTS.....	53
3.1 Introduction.....	53
3.2 Formulation of the Problem.....	58
3.3 The Volume Distribution of the Generation Rate.....	63
3.4 Results.....	71
3.5 Discussion.....	82
4 POTENTIAL IMPROVEMENT OF POLYSILICON SOLAR CELLS BY GRAIN-BOUNDARY AND INTRAGRAIN DIFFUSION OF ALUMINUM.....	87
4.1 Introduction.....	87
4.2 Cell Fabrication.....	91
4.3 Results.....	94
4.4 Discussion.....	109
5 ALUMINUM GETTERING IN (CAST) POLYSILICON.....	114
5.1 Introduction.....	114
5.2 Description of the Mechanisms.....	117
5.3 Results.....	122
5.4 Discussion.....	131
6 SUMMARY, DISCUSSION, AND RECOMMENDATIONS.....	135

	PAGE
APPENDIX	
A NUMERICAL SOLUTION OF POISSON'S EQUATION IN THE GRAIN-BOUNDARY SPACE-CHARGE REGION.....	141
B MATHEMATICAL JUSTIFICATION FOR USING THE FOLDING TECHNIQUE.....	164
C NUMERICAL ALGORITHM FOR SOLVING THE TWO-DIMENSIONAL CONTINUITY EQUATION UNDERLYING THE EBIC RESPONSE.....	168
C.1 Numerical Solution of the Steady-State Continuity Equation..	168
C.2 Numerical Evaluation of the Currents.....	172
D POLYSILICON CELL FABRICATION.....	201
D.1 Standard Cleaning Process.....	201
D.2 Bulk Process (Large Area Cells).....	200
D.3 Photolithography.....	202
D.4 Bulk Process (Small-Area Cells).....	202
D.5 Thin-Film Process (Large-Area Cells).....	204
REFERENCES.....	205
BIOGRAPHICAL SKETCH.....	212

Abstract of Dissertation Presented to the Graduate School
of the University of Florida in Partial Fulfillment of the
Requirements for the Degree of Doctor of Philosophy

STUDIES OF THE INFLUENCE, AND ITS CONTROL, OF GRAIN BOUNDARIES
ON MINORITY-CARRIER TRANSPORT IN POLYSILICON DEVICES

By

Ravishankar Sundaresan

December 1983

Chairman: Dr. Jerry G. Fossum
Co-Chairman: Dr. Dorothea E. Burk
Major Department: Electrical Engineering

In this dissertation we develop an analytic model for minority-carrier transport in polysilicon devices, and provide experimental corroboration for the model. The model is used to facilitate the development of experimental techniques, compatible with conventional device processing, to control the effects of grain boundaries. Techniques are investigated to reduce bulk recombination current by gettering intragrain impurities in polysilicon.

Key assumptions are made, with justification, to simplify the three-dimensional, nonlinear boundary-value problem that defines minority-carrier transport, including recombination, in polysilicon devices. These assumptions enable the separation of the grain-boundary recombination analysis, which is based on quasi-equilibrium, from the intragrain transport analysis, which is done by partitioning the grain into subregions in which the minority-carrier flow is predominantly one-dimensional. The analyses are coupled through the effective minority-carrier recombination velocity at the grain boundary, which generally is

dependent on the minority-carrier density in the adjacent quasi-neutral grain.

The dependence of the recombination velocity on the carrier density (excitation) at the grain boundary is experimentally demonstrated using electron-beam-induced-current (EBIC) measurements. To facilitate quantitative interpretation of the EBIC measurements, we solve the underlying carrier transport problem subject to the nonlinear boundary condition at the grain boundary using computer-aided numerical analysis. By comparing the theoretical and experimental EBIC responses, we predict values for the surface-state density at typical grain boundaries and the minority-carrier diffusion length in the grains.

Experimental results are presented that imply potential improvements afforded by aluminum diffusion in both bulk and thin-film polysilicon solar cells. For bulk cells, a high-temperature aluminum diffusion (alloying) is shown to increase the minority-carrier diffusion length by gettering intragrain impurities. For thin-film cells, a low-temperature aluminum diffusion is shown to substantially passivate grain boundaries and hence decrease the recombination velocity. The decrease is evaluated using EBIC measurements, the interpretation of which is aided by the numerical carrier transport model developed.

CHAPTER 1 INTRODUCTION

Polycrystalline silicon (polysilicon) is being widely used in the semiconductor industry to fabricate unipolar as well as bipolar devices [1]. The emergence of polysilicon devices has motivated studies of majority-carrier transport through the grain boundaries [2-6], which defines the resistivity of the polysilicon, as well as studies of minority-carrier recombination at the grain boundaries [7-11], which defines the bipolar characteristics of the polysilicon.

Compared to silicon (majority- and minority-carrier) devices, polysilicon devices perform poorly. The grain boundaries, in general, are responsible for the poor performance of the polysilicon devices. For example, in polysilicon MOSFETs the presence of grain boundaries causes a turn-on characteristic that is beyond the strong-inversion threshold [5], while in thin-film polysilicon solar cells [12] the conversion efficiency is lowered due to recombination at the grain boundaries. The understanding of how grain boundaries influence the transport of carriers in polysilicon is hence of engineering significance.

To enable the design and development of polysilicon solar cells that are cost-competitive with silicon cells, we must understand how the grain boundaries influence the minority-carrier transport and then devise fabrication techniques to minimize this influence. Although several approximate models [7-10, 13, 14] for the minority-carrier transport in polysilicon have been developed, they are inadequate in the

general case. The reason for this is that the models [7-10, 13] are based on restricting assumptions that limit their ranges of validity; furthermore, the solution of the minority-carrier transport equation is obtained by truncating an infinite series [8, 14], and hence the accuracy of the models is questionable. Many processing (passivating) techniques [15-19] have also been developed to control the grain-boundary recombination. However none of these techniques is easily adapted to solar cell processing and/or is totally effective [15-19].

The purpose of this research is to develop a general minority-carrier transport model for polysilicon that is based on a good physical understanding of grain boundaries, and to use it to develop experimental techniques, compatible with conventional device processing, to control the effects of grain boundaries; for example, to passivate grain boundaries and thereby improve the efficiency of polysilicon solar cells. Another limitation on the efficiency of polysilicon solar cells is due to the base minority-carrier lifetime, which is typically shorter than that in silicon cells due to high intragrain defect densities. Hence another purpose of this research is to develop experimental techniques to getter intragrain impurities. The primary tasks of the research are

- (1) to develop an analytic model for the minority-carrier transport in polysilicon;
- (2) to provide experimental corroboration for the transport model and to determine values for the pertinent grain-boundary parameters;
- (3) to develop experimental techniques to improve the performance of bulk and thin-film polysilicon solar cells and other bipolar devices.

Polycrystalline silicon, as the nomenclature implies, has more than one crystalline orientation (grain), each orientation is separated by a plane of dislocations (grain boundary). At the grain boundaries are defects [1], e.g., dangling bonds, which produce localized electron states (traps) throughout the energy gap. The net charge on these states, which results from majority-carrier trapping, gives rise to a potential barrier which influences the conduction properties of the polysilicon [6]. In minority-carrier devices, such as solar cells, the grain-boundary states serve as recombination centers for the minority carriers and hence constitute a source of recombination current. Thus the development of the minority-carrier transport model for polysilicon is complicated by the presence of randomly oriented surfaces (grain boundaries) at which significant recombination can occur.

Impedance measurements [20], current-voltage measurements [15, 16], and electron-beam-induced-current (EBIC) measurements [21, 22] have been used to characterize the barrier, or the defect density at the grain boundary, either of which is a measure of the grain-boundary recombination. We use the EBIC measurements to infer the grain-boundary parameters since it facilitates isolation of the grain boundary from the bulk grain. Such an isolation is beneficial in order to study the grain-boundary characteristics, e.g., the influence of the excitation on grain-boundary recombination. Furthermore the EBIC measurements do not require tedious sample preparation as do current-voltage measurements [15, 16] to obtain the grain-boundary parameters. An additional advantage is that we can infer the lifetime in the grain from EBIC measurements.

The presence of defect states results in current loss at the grain boundary and hence deteriorates the performance of polysilicon devices. To control the detrimental influence of the grain boundaries, it is necessary to reduce the defect states at the grain boundary. This reduction can be achieved by selective (preferential) diffusion of certain impurities [16-19] down the grain boundaries or by fabrication of special structures to eliminate them from the active portions of the device [15]. Furthermore, polysilicon contains high intragrain defect densities which cause short minority-carrier lifetimes. Hence it is necessary to consider processes that can getter the intragrain impurities and hence increase the minority-carrier lifetime.

In Chapter 2, we develop an analytic model for the minority-carrier transport in polysilicon. The general transport problem, which is three-dimensional and nonlinear [23], is simplified by making key assumptions with physical justification. The main feature of the model is the separation of the grain-boundary analysis, which yields an expression for the effective recombination velocity, from the grain analysis, which yields an expression for the base recombination current. The analyses are coupled through the effective recombination velocity at the grain boundary.

Our results indicate that the effective recombination velocity is, in general, dependent on the excitation (minority-carrier density) at the grain boundary, and in fact decreases with increasing excitation. This result renders most transport analyses [13, 14], which are based on the common assumption that the effective recombination velocity is a constant, not valid in general. Our results also indicate that at low and intermediate forward voltages, the base recombination current in a

polysilicon diode comprises a component independent of the grain-boundary parameters and a component strongly dependent on the grain-boundary parameters. Contrarily, at high forward voltages, the grain-boundaries have negligible effect on the base recombination current, and the polysilicon virtually behaves like single-crystal silicon.

In Chapter 3, we characterize the nonlinear effective recombination velocity at the grain boundary using EBIC measurements [21, 22]. The electron beam is incident from the top surface of a polysilicon cell and generates electron-hole pairs, predominantly in the base region of the cell. The generation (short-circuit) current is measured directly using an ammeter. The EBIC response of a grain in the vicinity of a grain boundary is obtained by measuring the generation current as a function of the distance of the center of the beam from the grain boundary.

To facilitate quantitative interpretation of the EBIC response, we develop a computer-aided numerical analysis of the underlying minority-carrier transport problem. Several numerical [24] and analytical [25, 26] solutions have been derived for the transport problem. However their ranges of validity are limited owing to simplifying assumptions of a point [26] or a spherical [24, 25] generation source, and a constant grain-boundary recombination velocity [24-26]. Our analysis removes these restricting assumptions, and hence is more general. The computer-aided numerical analysis, in this respect, is advantageous. The experimentally obtained EBIC response shows excellent agreement with our numerical analysis and demonstrates clearly the dependence of the effective recombination velocity on the excitation at the grain boundary, which provides corroboration for the transport model in Chapter 2. By comparing the theoretical and experimental EBIC

responses, we predict values for the defect density at typical grain boundaries and the minority-carrier diffusion length in the grains.

Having demonstrated the detrimental influences of the grain-boundary recombination on the minority-carrier transport, we next focus our attention on experimental methods to improve the performance of polysilicon solar cells. In Chapter 4, we describe an experimental technique, using aluminum diffusion, to passivate the grain boundaries, i.e., to reduce the defect density at the grain boundaries. Aluminum was chosen owing to its compatibility with solar cell processing, and to its large diffusion coefficient down the grain boundaries. It can also concomitantly getter the intragrain impurities, i.e., reduce the defect density in the grains, which results in an increase in the minority-carrier lifetime. The minority-carrier lifetime in polysilicon is typically lower than that in silicon due to high intragrain defect densities, and hence it is useful to consider processes that improve lifetime.

For the development of bulk polysilicon solar cells, in which the intragrain recombination is dominant, we propose a high-temperature (above eutectic, 577°C) aluminum-diffusion process from the back surface. For the development of thin-film cells, in which the grain-boundary recombination is dominant, we propose a low-temperature (below eutectic) aluminum-diffusion process from the front surface of the polysilicon. We use forward current-voltage and reverse-bias capacitance measurements to demonstrate the intragrain gettering, and EBIC measurements to show the grain-boundary passivation. Our results indicate that the high-temperature aluminum-diffusion process effectively getters intragrain impurities, whereas the low-temperature

aluminum-diffusion process produces significant grain-boundary passivation. We also find that the grain boundaries emit impurities during the high-temperature process and that these emitted impurities are effectively gettered by the aluminum.

Although we attribute the benefits produced by the high-temperature aluminum-diffusion process in Chapter 4 to intragrain gettering, the observed improvement in polysilicon device performance is also commensurate with the formation of a back-surface field (BSF) [27]. The BSF, which is nonuniform and nonplanar, is produced as a result of the preferential dissolution of silicon during the high-temperature aluminum-diffusion process [28]. In Chapter 5, we examine the mechanisms of gettering and BSF formation in an attempt to isolate the actual mechanism that is instrumental in improving the polysilicon device performance. The studies are based on forward current-voltage measurements of aluminum-diffused Wacker (cast) polysilicon cells, made before and after lapping off the back p^+p junction. Our results indicate that the observed improvement in the polysilicon device performance is due to effective gettering of intragrain impurities that occurs during the high-temperature aluminum-diffusion process, and that the nonuniform BSF is ineffective. No improvement in the performance of semiconductor-grade and solar-grade [29] silicon cells is observed, and hence we conclude that the benefits resulting from the aluminum-diffusion process are peculiar to the (cast) polysilicon. The benefits result possibly because of unique impurities prevalent in the polysilicon that are readily gettered by the aluminum. We surmise that aluminum getters oxygen and/or oxygen related defects which are present in higher densities in Wacker (cast) polysilicon than in semiconductor grade and solar-grade silicon.

We summarize our studies and review the main conclusions and accomplishments of this dissertation in Chapter 6. We also discuss the scope and limitations of this work and provide suggestions for future research.

CHAPTER 2
ANALYSIS OF MINORITY-CARRIER TRANSPORT IN
POLYSILICON DEVICES

2.1 Introduction

The performance of bipolar polycrystalline silicon devices can be limited because of minority-carrier recombination losses at the grain boundaries [7-11]. For example, the efficiency of thin-film polysilicon solar cells [12], which can potentially be used to produce cost-competitive terrestrial photovoltaic energy-conversion systems, is lower than that of silicon cells because of grain-boundary recombination. Hence a complete theoretical understanding of the influence of grain boundaries on minority-carrier transport is essential in order to optimize the design and performance of polysilicon solar cells and other bipolar polysilicon devices.

In the general case this influence is described by a complicated, three-dimensional boundary-value problem having nonlinear boundary conditions [23]. For example, in the forward-biased polysilicon n^+p junction with columnar grains illustrated in Fig. 2.1, the electron current injected into the quasi-neutral p-type base is governed, for low-injection conditions, by the three-dimensional electron continuity equation subject to nonlinear boundary conditions at the grain boundaries [7-11]. The three-dimensionality results basically because the carriers are injected at a surface (i.e., the pn junction) that is not parallel to the grain-boundary surface. The boundary conditions,

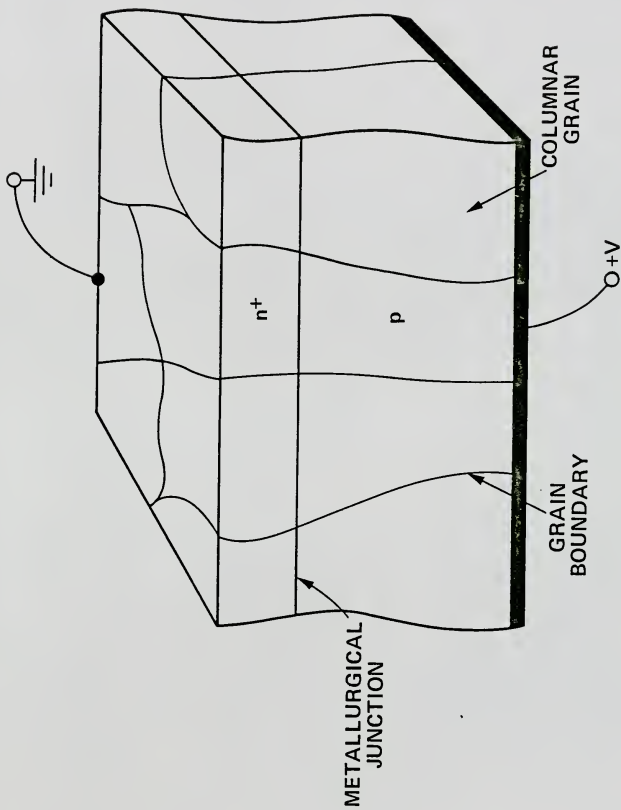


Fig. 2.1 Forward-biased polysilicon n^+p junction with columnar grains.

which characterize carrier recombination through energy-gap states at the grain boundaries, can be expressed by an effective recombination velocity that, in general, is dependent on the intragrain electron density and on position. Approximate solutions [7-11, 13, 14, 30] for this and related problems have been derived, but their ranges of validity have not been checked.

To help advance our understanding of minority-carrier transport in polysilicon, and to aid the engineering design of optimal polysilicon bipolar devices, including the solar cell, we describe in this chapter the development of an analytic model for the minority electron current injected into the base of the n^+p junction in Fig. 2.1. The model, which is subject to the uncertainties and inhomogeneities in the morphology and in the electrical properties of polysilicon, is not exact, but is, we believe, sufficiently representative of the physics to ensure its utility. Although we emphasize polysilicon, the analytical methods used in the model development are applicable to other polycrystalline semiconductors.

The electron current I_G^B injected into the base of each grain in Fig. 2.1 derives from recombination at the grain boundaries (I_{GB}^B) and within the quasi-neutral p-region (I_{QN}^B). A key feature of the model is the separation of the grain-boundary recombination analysis, which defines the effective recombination velocity $S_{n(eff)}^{GB}$, from the quasi-neutral grain transport analysis, which, with $S_{n(eff)}^{GB}$, defines I_G^B . The model differs from previous ones [7-11, 13, 14, 30] in the following ways: (a) it is based on a computer-aided numerical solution of Poisson's equation within the grain-boundary space-charge region, which provides the physical insight necessary to analytically characterize

$S_{n(\text{eff})}^{\text{GB}}$; (b) it unifies previous analyses based on the restricting assumptions of carrier depletion [7, 9, 10] and of quasi-equilibrium [7, 8] in the grain-boundary space-charge region, as well as those analyses based on the common assumption that $S_{n(\text{eff})}^{\text{GB}} = \infty$ [13], by incorporating into the quasi-equilibrium analysis the physical upper limit on $S_{n(\text{eff})}^{\text{GB}}$, i.e., the kinetic-limit velocity $S_{\text{KL}} (\approx 5 \times 10^6 \text{ cm/sec}$ at 300° K) imposed by the random thermal motion of the conduction-band electrons [31]; (c) it avoids possible errors involved in truncating infinite-series solutions for the three-dimensional electron continuity equation in the quasi-neutral grain [8, 14, 23, 30] by reducing the problem to coupled one-dimensional ordinary differential equations that are formulated based on "gradual-case" approximations [32]; (d) it is the first analytic model for minority-carrier transport in polysilicon derived from the physical insight provided by computer-aided numerical solutions.

The model development begins with the computer solution of Poisson's equation in the grain-boundary space-charge region adjoining quasi-neutral p-type grains, assumed to be in low injection. The numerical analysis is based on the quasi-equilibrium assumption [7, 8,] but the inherent limitations are effectively removed by accounting for the kinetic-limit electron velocity. The calculation of the grain-boundary potential barrier height is based on the assumption of an "effective" monoenergetic density of donor-type traps located near the middle of the energy gap. This assumption is commensurate with the experimental observation [20] that the "neutral Fermi level" of polysilicon grain boundaries is near midgap. Once the barrier height is determined, the composite recombination rate of hole-electron pairs

through both donor-type and acceptor-type traps is calculated accounting for the commonly large difference between the carrier capture parameters for neutral and ionized traps [9]. This recombination rate is then used to derive $S_{n(\text{eff})}^{\text{GB}}$, which is a function of the electron density. Empirical dependencies, implied by the numerical analysis, of $S_{n(\text{eff})}^{\text{GB}}$ on the grain-boundary surface-state densities, on the grain doping density, and on the "excitation" of the grain boundary, i.e., the separation of the electron and hole quasi-Fermi levels, are used to formulate an expression for $S_{n(\text{eff})}^{\text{GB}}$. The expression is supported by qualitative discussion of the underlying physics, including mention of the effects of assuming different trap energy levels.

To complete the model, the electron continuity equation in the quasi-neutral p-type base of a representative grain, assumed to be a right-circular cylinder, is analytically solved subject to the nonlinear boundary condition [$S_{n(\text{eff})}^{\text{GB}}$] at the grain boundaries, which varies with excitation along the boundaries, and to the excess electron density at the edge of the junction space-charge region resulting from the forward bias V . This complicated three-dimensional problem is solved analytically for relatively large grains by partitioning the grain into subregions in which the electrons are assumed to flow predominantly in one dimension. The one-dimensional solutions are then coupled to give the composite solution, which is approximate but nevertheless illustrates well the effects of the nonlinearity. The result is an analytic expression for I_G^{B} in terms of V and the parameters defining the morphology and electrical properties of the grain and the encompassing grain boundaries.

2.2 Analysis

The assumed representative grain, a right circular cylinder, of the polysilicon n^+p junction in Fig. 2.1 is illustrated in Fig. 2.2(a). The grain and grain boundary are assumed to be isotropic. Hence rotational symmetry exists about the central axis, and the carrier transport problem can be reduced to two dimensions as indicated in Fig. 2.2(b). Our objective is to analytically characterize the injected electron current $I_G^B = I_{GB}^B + I_{QN}^B$ that results from the junction forward bias V . (Note that we are accounting for recombination at the portion of the grain boundary adjacent to a quasi-neutral region. Recombination at the grain boundary within the junction space-charge region, which can be significant [33], is discussed in Section 2.3.) Rigorously this would require the solution of the complicated two-dimensional electron continuity equation in the quasi-neutral p -region of the grain subject to appropriate boundary conditions at the grain-boundary and junction space-charge regions [23]. The derived electron density $N(r,z)$ must be integrated over the volume of the p -region to determine I_{QN}^B , and its gradient integrated over the encompassing grain-boundary surfaces to determine I_{GB}^B . Such a rigorous solution would, even with simplifying assumptions, require a computer-aided numerical analysis [13].

To facilitate the engineering design of polysilicon bipolar devices, and to advance our understanding of the pertinent physics underlying their performance, an approximate analytic solution is useful. To derive such a solution, we separate the analysis of the grain-boundary recombination from that of the intragrain transport, even though the mechanisms are interrelated. This interrelationship

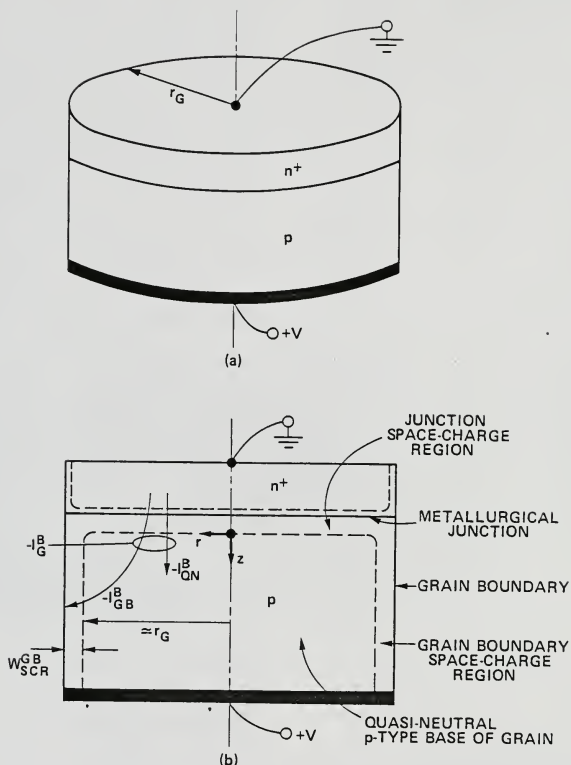


Fig. 2.2 Representative grain (a) of the forward-biased n^+p junction and its cross-section (b). We assume $r_G \gg w_{SCR}^{GB}$; hence the z -dependence of w_{SCR}^{GB} deriving from the z -dependence of the grain-boundary excitation is inconsequential and has not been shown.

materializes when we combine the results of the analyses to determine $N(r,z)$ and to characterize $I_G^B(V)$.

2.2.1 Grain Boundary

We first consider the grain-boundary space-charge region, which is identified in Fig. 2.2(b). By describing the hole-electron recombination rate U_{GB} along the grain boundary, assumed to involve only band-bound transitions, we can define the effective surface recombination velocity $S_{n(eff)}^{GB}$ for minority electrons at the edge of the grain-boundary space-charge region.

At an arbitrary depth z in the base region, we consider the energy-band diagram in the grain-boundary space-charge region. This diagram, which follows from the solution of Poisson's equation to be discussed, is illustrated for non-equilibrium conditions ($V > 0$) in Fig. 2.3. The existence of the potential barrier height ϕ_B is due to majority-carrier (hole) charging of the grain-boundary surface states and has been discussed extensively in previous papers [2, 7-10, 20].

To describe ϕ_B of the polysilicon grain boundary adjacent to a p-type grain, we assume an "effective" monoenergetic density $N_{ST(eff)}^D$ of donor-type grain-boundary surface states, or traps, which are either neutral or positively ionized, is representative of the grain-boundary potential barriers for p-type polysilicon because the "neutral Fermi level" of polysilicon grain boundaries, which is related to the unknown nature of the surface states, is experimentally observed to be near midgap [20]. This means that the electron energy bands will bend down at the grain boundaries in p-type polysilicon (see Fig. 2.3); this will be predicted by an analysis based on donor-type traps. Indeed $N_{ST(eff)}^D$

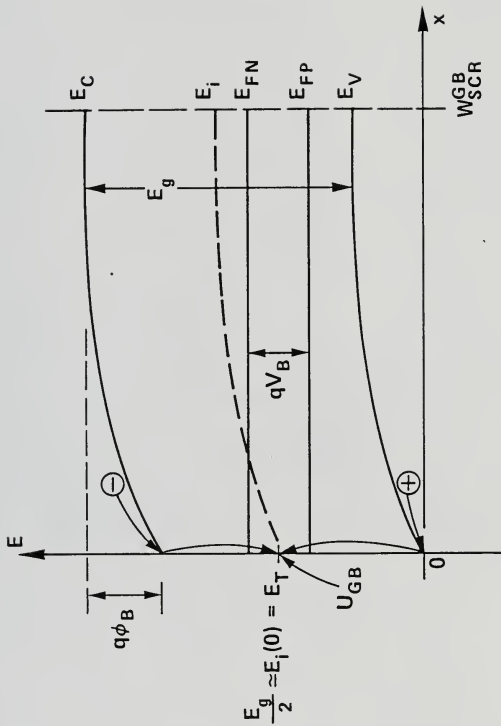


Fig. 2.3 Non-equilibrium energy-band diagram in the grain-boundary space-charge region characterized by quasi-equilibrium (nearly flat quasi-Fermi levels) and an effective monoenergetic density of grain-boundary surface states. Note that $V_B(z) < V$.

is the grain-boundary trap density that would be inferred from conductance or capacitance measurements [2, 20] of p-type polysilicon. Although the assumption of a monoenergetic density of traps at $E_T = E_i(0)$ may not characterize exactly actual grain boundaries in p-type polysilicon [34], it is sufficiently representative to describe their basic influence on the minority electron transport. The utility of a monoenergetic-trap-density analysis in characterizing the electrical behavior of polysilicon has been previously demonstrated [8, 10, 20, 23].

We recognize however that U_{GB} , which depends on ϕ_B , must be calculated based on the possible existence of both donor-type (N_{ST}^D) and acceptor-type (N_{ST}^A) trap densities. We later describe this calculation and the resulting description of $S_{n(eff)}^{GB}$, which depend critically on the large difference between the carrier capture parameters of neutral (C^n) and ionized (C^i) traps [9]. We also later discuss qualitatively the effects of moving E_T away from midgap.

For steady-state conditions, i.e., ϕ_B time-independent, the energy-band diagram in Fig. 2.3 and U_{GB} , which defines the rate of flow of electrons and holes to the grain boundary, are determined by the condition that the grain-boundary charge that produces overall neutrality in the grain-boundary space-charge region be commensurate with equal net capture rates for electrons and holes at the grain-boundary surface. Mathematically, the quasi-equilibrium assumption enables us to express this condition by combining Poisson's equation for the grain-boundary space-charge region with Shockley-Read-Hall capture-emission statistics [35] for the grain-boundary surface states.

Referring to Fig. 2.3, in which the grain boundary is located at $x = 0$, we write Poisson's equation in the space-charge region ($0 < x < W_{SCR}^{GB}$) as

$$\frac{d^2 E_i(x)}{dx^2} = \frac{q^2}{\epsilon} [P(x) - N(x) - N_{AA}] \quad (2.1)$$

where P and N are the hole and electron densities, N_{AA} is the grain (acceptor) doping density, q is the electron charge, ϵ is the dielectric constant of silicon, and E_i is the intrinsic Fermi level, whose derivative with respect to x defines the electric field. The electric field at $x = 0$ is determined by the grain-boundary surface-state charge through Gauss' law and provides one of the two boundary conditions necessary to solve (2.1):

$$\left. \frac{dE_i}{dx} \right|_{x=0} = \frac{q^2 N_{ST}^D (eff) (1 - f)}{2\epsilon} \quad (2.2)$$

where f is the steady-state probability of electron occupancy for the surface states. The factor of $1/2$ in (2.2) reflects our implicit assumption of symmetrical energy bands on either side of the grain boundary, i.e., identical adjacent grains.

Assuming a unity degeneracy factor for the grain-boundary surface states, we get from the Shockley-Read-Hall theory [35]

$$f = \frac{C_n N(0) + C_p n_i \exp\left[\frac{E_i(0) - E_T}{kT}\right]}{C_n N(0) + C_n n_i \exp\left[\frac{E_T - E_i(0)}{kT}\right] + C_p P(0) + C_p n_i \exp\left[\frac{E_i(0) - E_T}{kT}\right]}, \quad (2.3)$$

which simplifies under our assumption that $E_T = E_i(0)$. In (2.3), n_i is

the intrinsic carrier density in silicon; C_n is the capture coefficient for electrons, which we assume is $C_n^i \approx 10^{-7} \text{cm}^3/\text{sec}$ (at 300°K) because the trap is (positively) ionized prior to the electron capture [36]; and C_p is the capture coefficient for holes, which we assume is $C_p^i \approx 10^{-9} \text{cm}^3/\text{sec}$ (at 300°K) because the trap is neutral prior to the hole capture [36].

To write the second boundary condition, we assume low injection in the uniformly doped quasi-neutral p-region:

$$\left. \frac{dE_i}{dx} \right|_{x > W_{\text{SCR}}^{\text{GB}}} \approx 0 \quad . \quad (2.4)$$

This assumption also means that

$$P(W_{\text{SCR}}^{\text{GB}}) \approx N_{\text{AA}} \quad . \quad (2.5)$$

Within the grain-boundary space-charge region, P and N are related to E_i through the respective quasi-Fermi levels E_{FP} and E_{FN} :

$$P(x) = n_i \exp\left[\frac{E_i(x) - E_{\text{FP}}}{kT}\right] \quad , \quad (2.6)$$

$$N(x) = n_i \exp\left[\frac{E_{\text{FN}} - E_i(x)}{kT}\right] \quad . \quad (2.7)$$

The difference between E_{FN} and E_{FP} reflects the "excitation" of the grain boundary that results from the forward bias on the n^+p junction. To facilitate the separation of the grain-boundary recombination analysis from the intragrain transport analysis, we assume that conditions of quasi-equilibrium exist in the grain-boundary space-charge

region. This assumption implies that E_{FN} and E_{FP} are nearly flat (i.e., that their variations are less than kT) in this region, and will be valid if N and P are sufficiently large and the electron and hole currents sufficiently small, as we discuss later. This will be the case for sufficiently high excitations (see Fig. 2.3),

$$qV_B \triangleq E_{FN} - E_{FP} \quad , \quad (2.8)$$

and sufficiently low potential barriers,

$$q\phi_B \triangleq E_i(W_{SCR}^{GB}) - E_i(0) \quad . \quad (2.9)$$

Note that V_B defined in (2.8) decreases with z in accordance with $N(r_G, z)$, and that necessarily $V_B(z)$ is everywhere less than V because of the electron density gradient in the grain.

As we will see, the quasi-equilibrium assumption enables us to characterize U_{GB} without having to describe the mechanism, e.g., thermionic emission [10], by which majority carriers (holes) are transported from the quasi-neutral region to the grain-boundary surface. This simplification is made without loss of generality because when the quasi-equilibrium assumption is invalid, for example, when the grain-boundary space-charge region is virtually depleted of free carriers [7, 9, 10], the minority electrons are approaching the grain-boundary surface with velocities about equal to their kinetic limit S_{KL} ($\approx 5 \times 10^6$ cm/sec at 300°K) [31]. Hence, as we show later, when (2.8) becomes inapplicable, the grain boundary can be adequately modeled as a surface having a recombination velocity equal to S_{KL} . A detailed

analysis of grain-boundary recombination based on the depletion approximation thus is unnecessary and, in fact, is invalid.

The solution of (2.1)-(2.7), with arbitrary excitation V_B in (2.8), is impossible to derive analytically. Thus to aid the development of an analytic model for $S_{n(\text{eff})}^{\text{GB}}$ in terms of V_B and the polysilicon properties, we use computer-aided numerical techniques. A Harwell subroutine [37], which represents (2.1) using finite-difference approximations for the derivatives, has been slightly modified to solve (2.1)-(2.9). Details of the numerical algorithm and the listing of the computer program are given in Appendix A. We now discuss results of this numerical analysis of the grain-boundary region.

Consider first the thermal-equilibrium case ($V = 0$) for which $V_B = 0$ and E_{FN} and E_{FP} are coincident with the Fermi level E_F . Equilibrium barrier heights ϕ_{B0} at polysilicon grain boundaries have been previously calculated [7] and measured [20, 34, 38], and comparison of our numerical results with these earlier ones provides an assessment of the assumptions underlying the analyses. For example, it implies the validity of the depletion approximation for equilibrium conditions. In Fig. 2.4 we have plotted ϕ_{B0} versus N_{AA} for representative values of the effective grain-boundary surface-state density $N_{ST(\text{eff})}^D$. When $N_{ST(\text{eff})}^D$ is very low ($< 10^{10} \text{ cm}^{-2}$), ϕ_{B0} is extremely small, and electrically the polysilicon resembles single-crystal silicon. For intermediate values of $N_{ST(\text{eff})}^D$ ($\sim 10^{11} \text{ cm}^{-2}$), ϕ_{B0} decreases monotonically with increasing N_{AA} . This is explained by the fact that ϕ_{B0} is small enough that E_F is below E_T (see Fig. 2.3), and hence virtually all of the (donor) surface states are empty (positively ionized) for all N_{AA} . Thus as N_{AA} increases, the space-charge region width, which contains charge

(including ionized acceptor impurities) that neutralizes the grain-boundary charge, diminishes and hence ϕ_{B0} decreases. When $N_{ST(eff)}^D$ is high ($> 10^{12} \text{ cm}^{-2}$), ϕ_{B0} is large enough that E_F is essentially fixed at, or slightly above, E_T (see Fig. 2.3). Thus as N_{AA} increases and E_F moves closer to the valence-band edge in the quasi-neutral grain [i.e., farther away from E_i as described by (2.5) and (2.6)], E_T follows E_F at $x = 0$, and hence ϕ_{B0} increases slightly.

We note that the calculated values of ϕ_{B0} in Fig. 2.4 are generally higher than those derived from measurements [34] of the activation energy for the zero-bias conductance of grain boundaries in p-type polysilicon. This discrepancy results because of our assumption $E_T = E_i(0)$, which is not, as we mentioned earlier, strictly valid. Assuming $E_T < E_i(0)$ brings the ϕ_{B0} predictions and measurements into better agreement, but does not significantly augment the physical insight provided by our analysis. It is interesting to note that for n-type polysilicon, analogous calculations based on an assumed monoenergetic density of acceptor-type traps at midgap yield values of ϕ_{B0} that are roughly consistent with those derived experimentally [38].

Consider now non-equilibrium cases ($V > 0$) for which $V_B > 0$ in accordance with the quasi-equilibrium assumption in the grain-boundary space-charge region. Non-equilibrium conditions for which this assumption fails, alluded to earlier, will be treated explicitly later. The relationship between $V_B(z)$ and V is complex and follows from the electron continuity equation in the quasi-neutral p-region of the grain, which we solve in the next subsection.

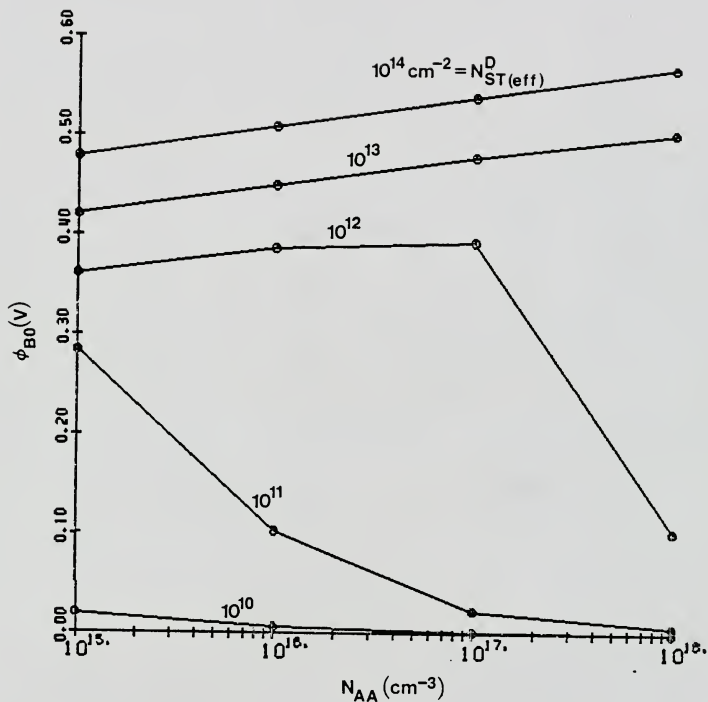


Fig. 2.4 Calculated thermal-equilibrium barrier height versus grain doping density (p-type) for representative values of effective grain-boundary surface-state density ($T = 300^\circ\text{K}$).

Figs. 2.5 and 2.6 show plots of calculated barrier heights ϕ_B versus V_B for representative values of $N_{ST}^D(\text{eff})$ and for $N_{AA} = 10^{15} \text{ cm}^{-3}$ and 10^{17} cm^{-3} respectively. These plots are restricted to conditions of low injection in the quasi-neutral p-region. They imply that

$$\frac{\partial \phi_B}{\partial V_B} = -\frac{1}{2} \quad (2.10)$$

for V_B greater than a few thermal voltages ($kT/q = 0.026 \text{ V}$), a condition that validates the quasi-equilibrium assumption. The monotonic reduction of ϕ_B with increasing V_B is consistent with the results in [8] and is qualitatively explained as follows. The electron capture rate at the grain boundary, which is proportional to $N(0)$, increases with increasing excitation. Consequently the net charge at the grain boundary and hence the grain-boundary barrier height, which is directly proportional to the net charge, decrease with increasing excitation. The slope of $-1/2$ in (2.10) has a physical basis as we now describe.

For steady-state conditions with sufficient excitation, the electron and hole capture rates at the grain-boundary surface states, including both donor and acceptor types, are nearly equal. Thus, for either type of state, we can write

$$\frac{\partial}{\partial V_B} [C_n(1 - f)N(0)] = \frac{\partial}{\partial V_B} [C_p f P(0)] \quad (2.11)$$

From (2.3), for the assumed conditions, we see that $f = C_n N(0) / [C_n N(0) + C_p P(0)]$, which is always between zero and one. Because the change in f induced by a small variation in V_B will be much smaller than the corresponding changes in $N(0)$ and $P(0)$, (2.11) implies

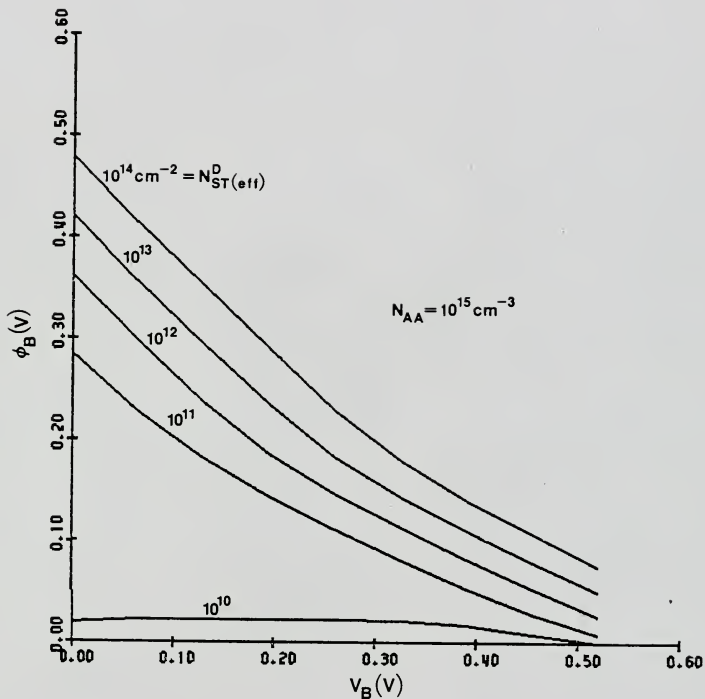


Fig. 2.5 Calculated non-equilibrium barrier height versus grain-boundary excitation for representative values of effective grain-boundary surface-state density and for a grain doping density of 10^{15} cm^{-3} ($T = 300^\circ\text{K}$).

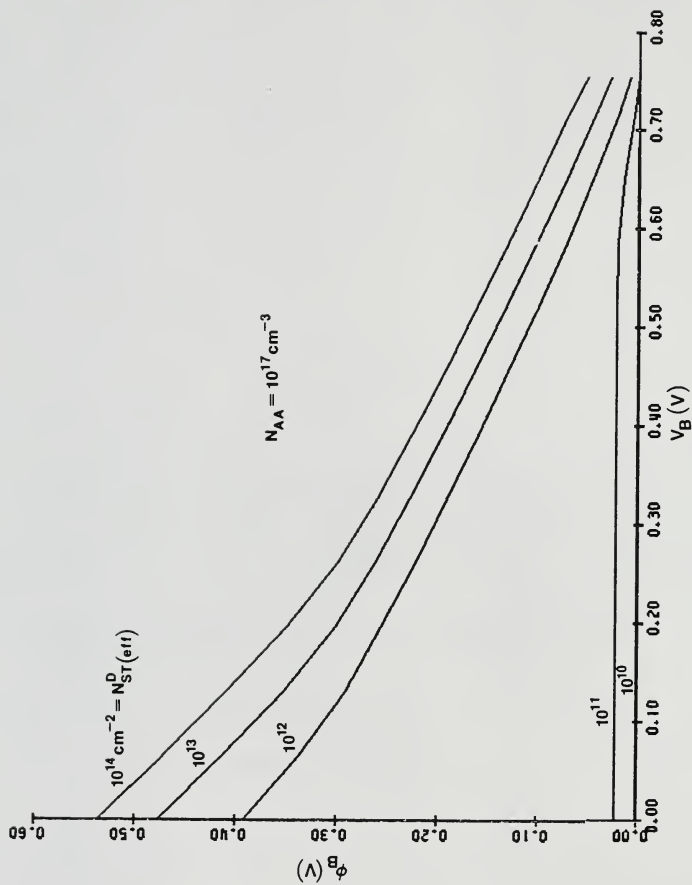


Fig. 2.6 Calculated non-equilibrium barrier height versus grain-boundary excitation for representative values of effective grain-boundary surface state density and for a grain doping density of 10^{17} cm^{-3} ($T = 300^\circ \text{K}$).

$$\frac{1}{N(0)} \frac{\partial N(0)}{\partial V_B} = \frac{1}{P(0)} \frac{\partial P(0)}{\partial V_B} \quad (2.12)$$

The relation in (2.12) is a general result of invoking the steady-state condition ($d\phi_B/dt = 0$) at a sufficiently excited grain-boundary surface. Combining it with

$$P(0)N(0) = n_i^2 \exp\left(\frac{qV_B}{kT}\right) \quad (2.13)$$

which follows from (2.6)-(2.8), reveals that

$$\frac{1}{P(0)} \frac{\partial P(0)}{\partial V_B} = \frac{q}{2kT} \quad (2.14)$$

Then substituting

$$P(0) = N_{AA} \exp\left(\frac{-q\phi_B}{kT}\right) \quad (2.15)$$

which results from (2.5), (2.6), and (2.9) with the assumption that E_{FP} is nearly flat, into (2.14) yields (2.10). (Note that this analytic description of the grain-boundary physics, as well as others to follow, are facilitated by the numerical solutions.)

The important conclusion to be drawn from (2.10) and the associated relationships mentioned above is that

$$P(0), N(0) \propto \exp\left(\frac{qV_B}{2kT}\right) \quad (2.16)$$

and consequently, as we detail later, $U_{GB} \approx \exp(qV_B/2kT)$. We now discuss the dependencies of ϕ_B , $P(0)$, and $N(0)$ on $N_{ST}^D(\text{eff})$ and on N_{AA} as derived from the numerical solutions of (2.1).

These solutions, those plotted in Figs. 2.5 and 2.6 and others, imply further that

$$\frac{\partial \phi_B}{\partial [\log N_{ST}^D(\text{eff})]} \approx \frac{kT}{q} \quad (2.17)$$

for sufficient excitation (V_B) as defined earlier. The implications of (2.17) regarding $P(0)$ and $N(0)$ follow from (2.13) and (2.15):

$$P(0) \approx [N_{ST}^D(\text{eff})]^{-\log(e)} = [N_{ST}^D(\text{eff})]^{-1/2} \quad (2.18)$$

and

$$N(0) \approx [N_{ST}^D(\text{eff})]^{\log(e)} = [N_{ST}^D(\text{eff})]^{1/2}, \quad (2.19)$$

which are also seen directly from the numerical results.

A physical explanation for (2.18) and (2.19) can be given, again based on the condition of nearly equal electron and hole capture rates through the (effective) grain-boundary traps:

$$C_n(1 - f)N_{ST}^D(\text{eff})N(0) = C_p f N_{ST}^D(\text{eff})P(0) \quad (2.20)$$

For sufficient V_B , partly because of the large discrepancy between C_n (C_n^j) and C_p ($= C_n$), $f = 1$; i.e., most of the traps are filled with electrons. Therefore the factor $(1 - f)N_{ST}^D(\text{eff})$ in (2.20) must be a

sublinear function of $N_{ST}^D(\text{eff})$; i.e., f must increase slightly with increasing $N_{ST}^D(\text{eff})$. Thus (2.20) suggests that

$$\frac{N(0)}{P(0)} \approx N_{ST}^D(\text{eff}) \quad (2.21)$$

Then (2.13) and (2.21) give approximately the observed dependencies (2.18) and (2.19).

Finally, the numerical solutions of (2.1) for sufficient excitation reveal that

$$\frac{\partial \phi_B}{\partial [\log N_{AA}]} \approx \frac{3kT}{2q} \quad (2.22)$$

and that

$$P(0) \approx N_{AA} \left[1 - \frac{3}{2} \log(e) \right] \approx N_{AA}^{1/3} \quad (2.23)$$

and

$$N(0) \approx N_{AA} \left[-1 - \frac{3}{2} \log(e) \right] \approx N_{AA}^{-1/3} \quad (2.24)$$

These approximate dependencies can be supported by physical argument as follows. From (2.15), we get

$$\frac{\partial \phi_B}{\partial N_{AA}} = \frac{kT}{qN_{AA}} \left[1 - \frac{\frac{\partial P(0)}{\partial N_{AA}}}{\frac{P(0)}{N_{AA}}} \right] \quad (2.25)$$

For $\phi_B > 0$, the second term within the brackets of (2.25) is less than one, and, typically, considerably so as evidenced by (2.15), Fig. 2.3,

and the exponential relationship between P and E_{FP} , which defines the modification in the energy-band diagram resulting from a change in N_{AA} . Thus (2.25) implies that

$$\frac{\partial \phi_B}{\partial N_{AA}} \approx \frac{kT}{qN_{AA}}, \quad (2.26)$$

which is approximately equivalent to the observation (2.22).

Our computer-aided determination of the dependencies of ϕ_B and of $P(0)$ and $N(0)$ on V_B , $N_{ST}^D(\text{eff})$, and N_{AA} enables the characterization of the steady-state hole-electron recombination rate U_{GB} through the grain-boundary surface states, provided the active surface-state densities are specified. This calculation is based on the Shockley-Read-Hall capture-emission model [35] for recombination-generation through localized states in the energy gap.

Because the exact nature of the grain-boundary surface states in polysilicon is not known, we allow for the possible existence of both donor-type (N_{ST}^D) and acceptor-type (N_{ST}^A) states in our calculation of U_{GB} . We assume that all states are located at $E_T = E_i(0)$. Note that N_{ST}^D and N_{ST}^A are different from $N_{ST}^D(\text{eff})$, which was used to calculate ϕ_B , and $P(0)$ and $N(0)$. Physically, based on this model, N_{ST}^D and N_{ST}^A produce grain-boundary charge that is effectively characterized by $N_{ST}^D(\text{eff})$.

If we neglect bound-bound carrier transitions between the donor and acceptor traps, the composite recombination rate through N_{ST}^D and N_{ST}^A is simply

$$U_{GB} = U_{GB}^D(N_{ST}^D) + U_{GB}^A(N_{ST}^A) \quad (2.27)$$

where U_{GB}^D and U_{GB}^A are Shockley-Read-Hall representation [35] of the recombination rates through the donor and acceptor traps respectively:

$$U_{GB}^D = \frac{P(0)N(0) - n_i^2}{P(0) + n_i} \frac{N(0) + n_i}{C^i N_{ST}^D + C^n N_{ST}^D} ; \quad (2.28)$$

$$U_{GB}^A = \frac{P(0)N(0) - n_i^2}{P(0) + n_i} \frac{N(0) + n_i}{C^n N_{ST}^A + C^i N_{ST}^A} . \quad (2.29)$$

In (2.28) and (2.29) we have used the previously assumed capture parameter values $C^i = 10^{-7}$ cm³/sec and $C^n = 10^{-9}$ cm³/sec for the ionized (positively or negatively) and neutral states of the traps.

The dependencies of U_{GB} on the excitation V_B and on the grain-boundary surface-state densities, $N_{ST}^D(\text{eff})$, N_{ST}^D , and N_{ST}^A , and on the grain doping density N_{AA} are implicitly given by (2.27)-(2.29) and the explicit dependencies of $P(0)$ and $N(0)$ derived from the solutions of (2.1). For example, (2.16) and (2.27)-(2.29) show

$$U_{GB} = \exp\left(\frac{qV_B}{2kT}\right) \quad (2.30)$$

for the sufficient excitations needed to formulate the analytic relationships discussed earlier. The result (2.30) agrees with [7] and [8], but is not equivocal like [7] and [8] because of questionable assumptions, which, in fact, are shown to be invalid by our numerical results. Furthermore (2.30) has been derived here for the general case

in which both donor- and acceptor-type traps are present at the grain-boundary surface, and the constant of proportionality for (2.30) is related correctly to the assumed model for the surface states, in contrast to [7] and [8].

If we neglect recombination in the grain-boundary space-charge region (see Fig. 2.3), U_{GB} defines the effective recombination velocity for minority electrons at the edge of the space-charge region [7, 8]:

$$S_{n(eff)}^{GB} = \frac{U_{GB}}{2N(w_{SCR}^{GB})} \quad (2.31)$$

where, from (2.5)-(2.8),

$$N(w_{SCR}^{GB}) \approx \frac{n_i^2}{N_{AA}} \exp\left(\frac{qV_B}{kT}\right) ; \quad (2.32)$$

V_B and $N(w_{SCR}^{GB})$, both dependent on z , define the grain-boundary excitation and are determined from the coupled solution to the electron continuity equation to be discussed in the following subsection. Note the nonlinearity associated with $S_{n(eff)}^{GB}$ as defined by (2.30)-(2.32):

$$S_{n(eff)}^{GB} = S_0 [N_{ST(eff)}^D, N_{ST}^D, N_{ST}^A, N_{AA}] \exp\left(-\frac{qV_B}{2kT}\right) = S_0 \left[\frac{n_i^2}{N_{AA} N(w_{SCR}^{GB})} \right]^{1/2} \quad (2.33)$$

where the pre-exponential coefficient S_0 reflects the functional dependencies derived from the numerical solutions. An expression for S_0 , derived empirically from the numerical solutions, is given by

$$S_0 = \frac{c^n c^i N_{AA}}{2n_i} \left[\frac{N_{ST}^D}{\left[c^n \left(\frac{N_{AA}}{10^{15}} \right)^{\log 2} \left(\frac{5 \times 10^{10}}{N_{ST}^D} \right)^{1/2} + c^i \left(\frac{10^{15}}{N_{AA}} \right)^{\log 2} \left(\frac{N_{ST}^D}{5 \times 10^{10}} \right)^{1/2} \right]} + \frac{N_{ST}^A}{\left[c^i \left(\frac{N_{AA}}{10^{15}} \right)^{\log 2} \left(\frac{5 \times 10^{10}}{N_{ST}^A} \right)^{1/2} + c^n \left(\frac{10^{15}}{N_{AA}} \right)^{\log 2} \left(\frac{N_{ST}^A}{5 \times 10^{10}} \right)^{1/2} \right]} \right] \quad (2.34)$$

Values of $S_{n(\text{eff})}^{\text{GB}}$ have been numerically calculated for two cases involving assumed trap densities N_{ST}^D and N_{ST}^A . In the first case, we let $N_{ST}^D = N_{ST}^D(\text{eff})$ and $N_{ST}^A = 0$, which corresponds to the simple common assumption that only donor-type traps are effective on a polysilicon grain boundary between p-type grains [23]. Plots of $S_{n(\text{eff})}^{\text{GB}}$ versus V_B for this case are shown in Figs. 2.7 and 2.8 for $N_{AA} = 10^{15} \text{ cm}^{-3}$ and 10^{17} cm^{-3} respectively. In the second case, we let $N_{ST}^D = 2N_{ST}^D(\text{eff})$ and $N_{ST}^A = N_{ST}^D(\text{eff})$ to approximately represent a possible situation involving both donor- and acceptor-type traps at the grain boundary. Figs. 2.9 and 2.10 show $S_{n(\text{eff})}^{\text{GB}}$ for this case, and emphasize the possibility of certain traps influencing U_{GB} but not significantly affecting ϕ_B or the conductance or capacitance associated with the grain boundary.

Superimposed on the plots in Figs. 2.7-2.10 is an indication of the kinetic-limit velocity S_{KL} ($\approx 5 \times 10^6 \text{ cm/sec}$ at 300°K), which is defined by the random thermal motion of electrons in the conduction band [31]. The velocity S_{KL} is the average directional thermal velocity defined by Maxwell-Boltzmann statistics for conduction-band (free) electrons, and is the physical upper limit for $S_{n(\text{eff})}^{\text{GB}}$. We therefore recognize that our plots of $S_{n(\text{eff})}^{\text{GB}}$ in Figs. 2.7-2.10 must be truncated at S_{KL} . This

recognition effectively removes any uncertainty or restriction of our model due to the possible invalidity of the quasi-equilibrium assumption. We now demonstrate this.

The quasi-equilibrium assumption is valid if the variations in the quasi-Fermi levels across the grain-boundary space-charge region (see Fig. 2.3) are less than kT [8, 9]. A quantitative self-consistency check for the validity of this assumption is described in [8]. Using this check and our results shown in Figs. 2.7-2.10, we find that generally the quasi-equilibrium assumption is justified provided $S_{n(\text{eff})}^{\text{GB}}$ is less than S_{KL} . Since $S_{n(\text{eff})}^{\text{GB}}$ cannot physically exceed S_{KL} , our model is then generally valid if, as indicated in Figs. 2.7-2.10, we stipulate that

$$\text{MAX}\left[S_{n(\text{eff})}^{\text{GB}}\right] = S_{\text{KL}} \quad . \quad (2.35)$$

Hence for all conditions under which the grain-boundary space-charge region is depleted of free carriers, which obviously preclude quasi-equilibrium, $S_{n(\text{eff})}^{\text{GB}} \approx S_{\text{KL}}$, and a depletion-approximation analysis [7, 9, 10] is unnecessary. In fact, a recent such analysis [10] yielded results that comply with these conclusions.

Note in Figs. 2.7-2.10 that for low values of $N_{\text{ST}(\text{eff})}^{\text{D}}$, depending on N_{AA} , $S_{n(\text{eff})}^{\text{GB}}$ as calculated from the numerical solutions of (2.1) is insensitive to low excitations V_{B} . Our analytic model (2.33) is inapplicable for these conditions because of the underlying assumption of "sufficient excitation." This insensitivity reflects the insensitivity of ϕ_{B} on V_{B} for low $N_{\text{ST}(\text{eff})}^{\text{D}}$ illustrated in Figs. 2.5 and 2.6. Fig. 2.4 reveals that $\phi_{\text{B}} \approx \phi_{\text{B0}}$ for these cases and explains

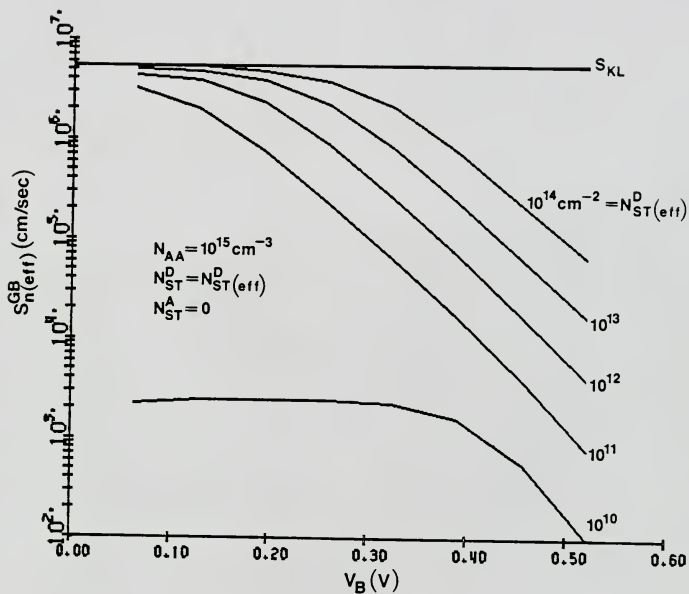


Fig. 2.7 Calculated effective recombination velocity for minority electrons at the edge of the grain-boundary space-charge region versus grain-boundary excitation and surface-state density. The kinetic-limit velocity, which is the physical upper limit for the recombination velocity, is indicated here and in Figs. 2.8 - 2.10.

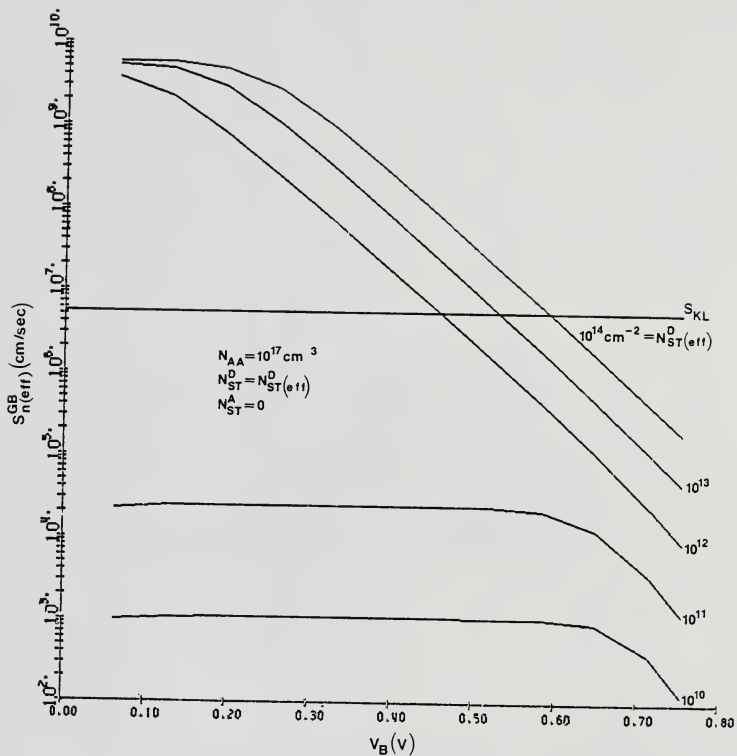


Fig. 2.8 Calculated effective recombination velocity for minority electrons at the edge of the grain-boundary space-charge region versus grain-boundary excitation and surface-state density.

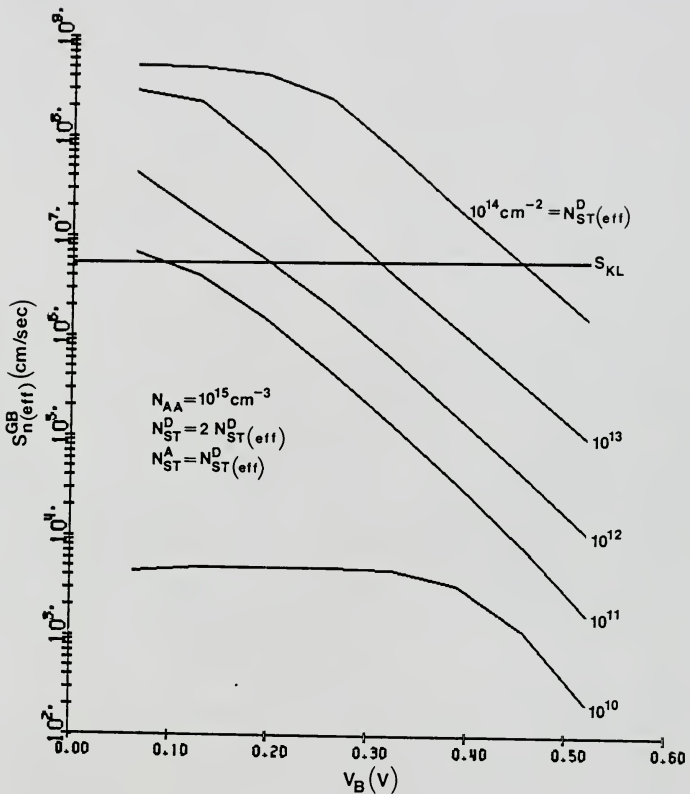


Fig. 2.9 Calculated effective recombination velocity for minority electrons at the edge of the grain-boundary space-charge region versus grain-boundary excitation and surface-state density.

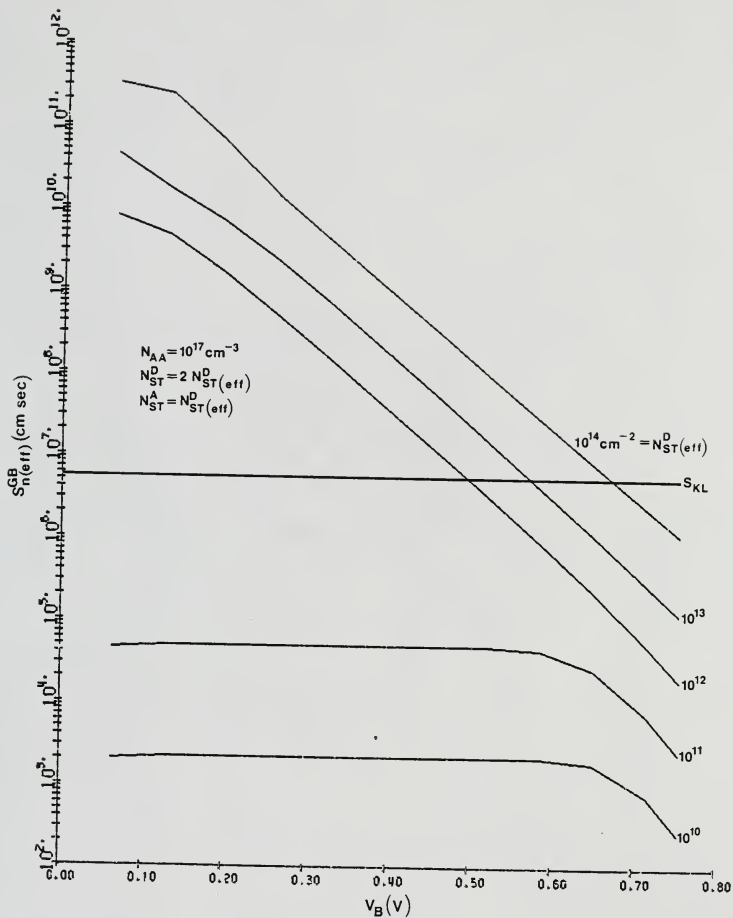


Fig. 2,10 Calculated effective recombination velocity for minority electrons at the edge of the grain boundary space-charge region versus grain-boundary excitation and surface-state density.

why $S_{n(\text{eff})}^{\text{GB}}$ is independent of the grain-boundary excitation. The excitation is insufficient to create a high enough electron density to alter the barrier height from its low equilibrium value [$N(0) \ll P(0)$]. Thus, when the electron emission rate is negligible, $S_{n(\text{eff})}^{\text{GB}} \sim C_n N_{\text{ST}}^{\text{D}}$ for these cases.

2.2.2 Grain

We now derive an approximate solution for the two-dimensional electron continuity equation in the quasi-neutral p-base of the grain illustrated in Fig. 2.2(b). This solution, which is governed by $S_{n(\text{eff})}^{\text{GB}}$ given in (2.33) and (2.35), yields the electron current $I_G^{\text{B}} = I_{\text{GB}}^{\text{B}} + I_{\text{QN}}^{\text{B}}$ injected into the base of the forward-biased n^+p junction.

Because of the nonlinear boundary condition at the grain boundaries, a rigorous derivation of this solution would require a computer. To simplify the problem such that an analytic solution, useful for engineering design and for demonstration of the pertinent physics, can be obtained, we partition the p-region as shown in Fig. 2.11. The implicit assumption made in doing this is that in certain subregions of the base, the electron flow is predominantly one-dimensional; that is, the divergence of the current density has one predominant term. Thus the resulting one-dimensional forms of the continuity equation can be solved, and the solutions then coupled to give $N(r,z)$, which defines I_G^{B} . This simplification is similar to Shockley's "gradual-case" approximation in his analysis of the unipolar transistor [32] and was qualitatively mentioned in [23]. Its utility was established in a numerical study [39] of the two-dimensional minority-carrier flow in a forward-biased planar diffused pn junction.

As indicated in Fig. 2.11, we assume that in the central portion of the grain ($r < r_1$), the electron flow is not influenced by the grain-boundary recombination, and is hence in the downward z -direction. Contrarily, we assume that in the vicinity of the grain boundary ($r_1 < r < r_G$), the electron flow is strongly influenced by the grain-boundary recombination, and is thus primarily in the lateral r -direction. These assumptions are commensurate with letting

$$r_1 = r_G - L_n \quad , \quad (2.36)$$

where L_n is the electron diffusion length. Note that (2.36) restricts our quasi-two-dimensional analysis to cases for which $r_G > L_n$. Although this inequality implies that I_G^B is not dominated by I_{GB}^B , the solutions for these cases nevertheless serve to illustrate well the effects of the nonlinearity introduced by $S_{n(eff)}^{GB}$. If $r_G < L_n$, which implies a predominance of I_{GB}^B , the electron flow is truly three-dimensional everywhere, and this case requires a computer solution. However, from a practical viewpoint, this case may be undesirable because the electron current is dominated by grain-boundary recombination ($I_{GB}^B > I_{QN}^B$); it could be avoided perhaps by increasing N_{AA} to reduce L_n , while still decreasing I_G^B .

In the central region of the grain, the electron density $N(z)$ for low-injection conditions is defined by

$$\frac{d^2 N(z)}{dz^2} - \frac{N(z)}{L_n^2} = 0 \quad (2.37)$$

with the boundary conditions

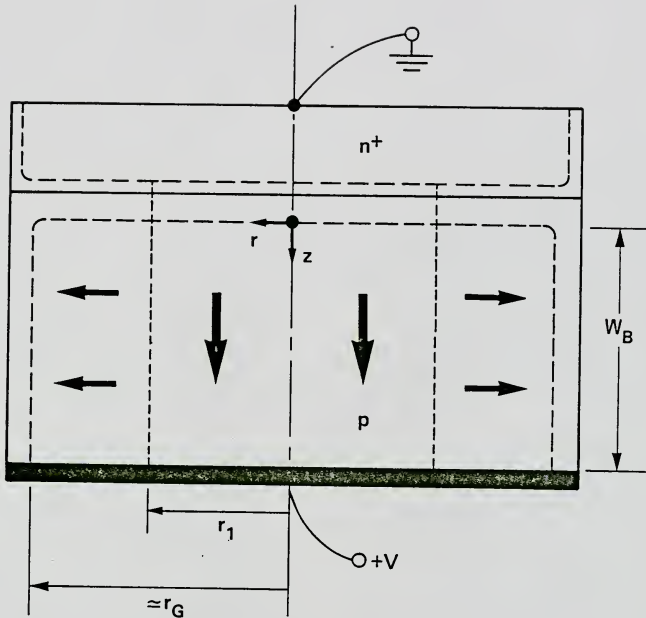


Fig. 2.11 Partitioned p -region of the representative grain showing predominantly one-dimensional electron flow in the subregions ($r_G > L_n$).

$$N(0) = \frac{n_i^2}{N_{AA}} \exp\left(\frac{qV}{kT}\right) \quad (2.38)$$

and

$$N(W_B) = 0 \quad , \quad (2.39)$$

the latter being due to the ohmic contact on the back of the junction.

The solution of (2.37)-(2.39) which is obvious, then provides one boundary condition, i.e., $N(r_1, z)$, for the coupled problem in the vicinity of the grain boundary:

$$\frac{1}{r} \frac{\partial}{\partial r} \left[r \frac{\partial N(r, z)}{\partial r} \right] - \frac{N(r, z)}{L_n^2} = 0 \quad . \quad (2.40)$$

The general solution of (2.40) is an infinite series. To obtain an approximate solution that is consistent with our partitioned-base model, we initially neglect the second term, but later account for the recombination current it defines by integrating $qN(r, z)/\tau_n$ (τ_n is the electron lifetime) over the quasi-neutral base of the grain. This results in a $\ln(r)$ dependence for N .

The second boundary condition for (2.40) is that defining the grain-boundary recombination discussed in the previous subsection:

$$-\frac{1}{q} J_N^r(r_G, z) \equiv -D_n \left. \frac{\partial N(r, z)}{\partial r} \right|_{r=r_G} = S_{n(\text{eff})}^{\text{GB}} N(r_G, z) \quad (2.41)$$

where D_n is the electron diffusion coefficient and where $S_{n(\text{eff})}^{\text{GB}}$, which depends on z , is given either by (2.33), in which $N(w_{\text{SCR}}^{\text{GB}}) = N(r_G, z)$, or by (2.35). The determination of which expression to use involves an iterative process. We initially use (2.33), solve (2.37)-(2.41), compare (2.33) and (2.35) everywhere on the grain boundaries, and then use (2.35) where necessary. This complicated process is typically simplified because unrealistic values of $S_{n(\text{eff})}^{\text{GB}} > S_{\text{KL}}$ imply, through the solution of the electron continuity equation in the grain, that $V_B = 0$ at the point being considered; this is also implied by the realistic value of $S_{n(\text{eff})}^{\text{GB}} = S_{\text{KL}}$ provided $S_{\text{KL}} > D_n/L_n$, which is common.

The electron density $N(r, z)$ derived from (2.37)-(2.41) can now be used to calculate the injected electron current I_G^{B} . The component due to recombination at the grain-boundary surfaces is

$$I_{\text{GB}}^{\text{B}} = -2\pi q D_n r_G \int_0^{w_B} \left. \frac{\partial N(r, z)}{\partial r} \right|_{r=r_G} dz, \quad (2.42)$$

and that due to recombination in the quasi-neutral p-base is

$$I_{\text{QN}}^{\text{B}} = \frac{2\pi q}{\tau_n} \int_0^{w_B} \int_0^{r_G} N(r, z) r dr dz, \quad (2.43)$$

in which the integration must be done in accordance with the partitioning of the p-region.

The general form of the resulting expression for the electron current, $(I_{GB}^B + I_{QN}^B)$, is

$$I_G^B(V) = I_{O1} \exp\left(\frac{qV}{kT}\right) + I_{O_n} \exp\left(\frac{qV}{n(V)kT}\right) \quad (2.44)$$

In (2.44) the $\exp(qV/kT)$ component is the electron current that would be injected in the absence of grain boundaries. For example, if $L_n < W_B$, then $I_{O1} = A_G q n_i^2 D_n / N_{AA} L_n$ where $A_G = \pi r_G^2$ is the area of the grain. In the $\exp(qV/nkT)$ component, which in general comprises both grain-boundary and intragrain recombination, I_{O_n} depends on S_0 , given in (2.34) in addition to the p-region parameters that define I_{O1} . The reciprocal slope factor $n(V)$, which also depends on S_0 and the p-region parameters, increases from one to two as V increases, albeit in the range corresponding to low-injection conditions in the p-region.

The general shape of the $I_G^B(V)$ characteristic in (2.44) for typical values of the grain and grain-boundary parameters is illustrated in Fig. 2.12. The shape resembles that of the dark current-voltage characteristic of a BSF solar cell [40], e.g., a p^+nn^+ cell, in which the inflection in the curve results because of the relative significance of different components of current having different reciprocal slope factors.

In Fig. 2.12, for low V , $I_G^B \propto \exp(qV/kT)$ because $n(V) \approx 1$. This occurs because the electron injection level is very low, and hence $S_{n(\text{eff})}^{GB}$, which is proportional to $[N(W_{SCR}^{GB})]^{-1/2}$ ($\equiv [N(r_G, z)]^{-1/2}$) as shown by (2.33), is high and fixed at S_{KL} everywhere (see Figs. 2.7-2.10). The nonlinearity is thereby removed and both I_{GB}^B and I_{QN}^B vary as $\exp(qV/kT)$. As V increases, $N(W_{SCR}^{GB})$ tends to increase also, and

thus $S_{n(\text{eff})}^{\text{GB}}$ begins to fall below S_{KL} at portions of the grain boundaries. The nonlinearity is hence apparent, and $n(V)$ exceeds unity; the slope of $I_G^{\text{B}}(V)$ decreases as shown in Fig. 2.12. At higher V , the $\exp(qV/nkT)$ component becomes insignificant, and $I_G^{\text{B}}(V) \rightarrow I_{01} \exp(qV/kT)$, resulting in the inflection in the curve, above which the grain boundaries are inconsequential because $S_{n(\text{eff})}^{\text{GB}}$ is low where the electron density is appreciable.

The general shape of the $I_G^{\text{B}}(V)$ curve predicted by our analysis and shown in Fig. 2.12 is consistent with measured current-voltage characteristics of gated n^+p diodes fabricated on Wacker polysilicon [16]. The characteristics of diodes containing substantial grain-boundary-surface area show an inflection similar to that in Fig. 2.12 whereas those of diodes having little or no grain-boundary-surface area, e.g., diodes fabricated within a grain, shown no inflection.

If $S_0 \rightarrow 0$, then $I_{0n} \rightarrow 0$, and the $I_G^{\text{B}}(V)$ characteristic approaches that of a single-crystal silicon junction. If $S_{n(\text{eff})}^{\text{GB}} \rightarrow S_{\text{KL}}$ everywhere, then $n \rightarrow 1$, and, as in the $S_0 = 0$ case, $I_G^{\text{B}}(V) \propto \exp(qV/kT)$, but with a pre-exponential coefficient greater than I_{01} because of the grain-boundary recombination. This discrepancy is commonly described in terms of an "effective" minority electron lifetime in the grain, which is smaller than τ_n [1, 8, 13]. It is important to note however that such a description pertains only to I_G^{B} , and not necessarily to other responses of the junction, e.g., the short-circuit photocurrent, and is meaningful only when $n = 1$.

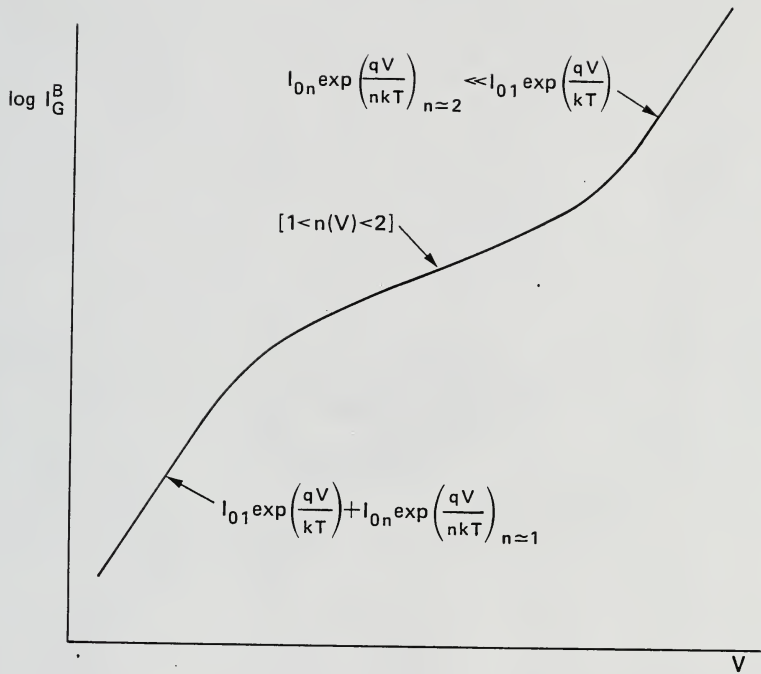


Fig. 2.12 Theoretical representation of the electron current injected into the base of the forward-biased polysilicon n^+p junction.

2.3 Discussion

In this chapter we have developed, using computer-aided numerical solutions, an approximate model for the electron current I_G^B injected into the base of a representative grain of the forward-biased polysilicon n^+p junction illustrated in Fig. 2.1. Key assumptions have been made to simplify the general three-dimensional, nonlinear boundary-value problem, i.e., the electron continuity equation, and to make this development possible. We now discuss these assumptions and, where necessary, the model limitations they imply.

We based the grain-boundary recombination analysis on the assumption of quasi-equilibrium, i.e., nearly flat quasi-Fermi levels, in the grain-boundary space-charge region. This assumption facilitates the separation of the grain-boundary recombination analysis from the intragrain electron transport analysis, the results of which define the grain-boundary excitation. The assumption further enables a complete analysis of the grain-boundary recombination without having to ascertain the mechanism, e.g., thermionic emission [10], by which majority holes are transported from the quasi-neutral grain to the grain-boundary surface.

The limitations associated with the quasi-equilibrium assumption are effectively removed by recognizing that when conditions obtain that negate quasi-equilibrium, the minority electrons flow to the grain-boundary surface with velocities about equal to the kinetic-limit velocity S_{KL} [31]. Thus we simply truncated in (2.35) our quasi-equilibrium-based prediction (2.33) for the effective electron recombination velocity $S_{n(\text{eff})}^{GB}$ at S_{KL} when (2.33) yields $S_{n(\text{eff})}^{GB} = S_{KL}$.

Even with the quasi-equilibrium assumption, the grain-boundary analysis, i.e., the solution of Poisson's equation (2.1), is formidable. Thus we resorted to a computer-aided numerical solution of (2.1) to facilitate the derivation of the analytic model for $S_{n(\text{eff})}^{\text{GB}}$. Empirical relationships implied by the numerical solutions were supported by qualitative discussion of the underlying physics.

We also assumed monoenergetic densities of surface states at the grain boundary. First, in accord with the position of the "neutral Fermi level" of polysilicon grain boundaries being near the middle of the energy gap, we postulated the existence of effective donor-type (adjacent to p-type grains) states near midgap to calculate the grain-boundary potential barrier height ϕ_B . Then, based on our assumed existence of both donor-type and acceptor-type traps at midgap, ϕ_B was used to calculate the grain-boundary recombination and ultimately $S_{n(\text{eff})}^{\text{GB}}$.

The utility of an analysis based on a monoenergetic density of grain-boundary surface states, which is not realistic, has been discussed before [8, 10, 20, 23]. Such a model provides physical insight and possibly simulates well actual surface-state distributions in the energy gap that significantly influence carrier recombination at the grain boundary. A recent analysis [11], which assumes the surface-states to be distributed in the energy gap, has yielded results that are consistent with ours. To generalize our results somewhat, we studied the effects of moving the trap level E_T away from midgap. Provided E_T remains relatively deep in the energy gap, i.e., $\approx 5kT$ above or below midgap, the functional dependencies in our model prevail. That is, $S_{n(\text{eff})}^{\text{GB}}$ as described in (2.33) for sufficient excitation of the

grain boundary depends on the electron density in the adjacent grain and hence manifests a nonlinear boundary condition for the electron continuity equation in the quasi-neutral p-region. When E_T is shallow, near either the conduction or the valence band, the carrier emission (exponential) terms in (2.3) tend to dominate and render f , and hence ϕ_B nearly insensitive to the grain-boundary excitation. Thus in this case, the nonlinearity does not occur, and $S_{n(\text{eff})}^{\text{GB}}$ is nearly constant equal either to S_{KL} (e.g., for E_T near the conduction band) or to lower values (e.g., for E_T near the valence band).

However the observation [20, 34, 38] that the neutral Fermi level of polysilicon grain boundaries is near midgap implies that E_T is not shallow. Thus the electron transport within the quasi-neutral p-region is generally complicated by the nonlinear boundary condition defined by $S_{n(\text{eff})}^{\text{GB}}$ in (2.33). To enable the derivation of an analytic solution for the electron continuity equation, we partitioned the p-region into subregions in which we assumed the electron flow is predominantly one-dimensional. In the central portion of the grain, we assumed that the electron flow was not significantly influenced by the grain-boundary recombination. The one-dimensional solution in this subregion then provided a boundary condition for the coupled transport problem in the subregion adjacent to the grain boundary where the strong influence of the grain-boundary recombination, simulated by $S_{n(\text{eff})}^{\text{GB}}$ [i.e., (2.33) and (2.35)], was assumed to cause the electrons to flow one-dimensionally toward the grain boundary.

The general results of the intragrain analysis, valid for $r_G > L_n$, was the expression (2.44) for $I_G^B(V)$, which includes an $\exp(qV/nkT)$ component ($1 < n < 2$) that occurs because of the nonlinearity introduced

by $S_{n(\text{eff})}^{\text{GB}}$. The occurrence of this component complicates the interpretation of measured current-voltage characteristics of polysilicon pn junctions. Because the current component deriving from recombination in the junction space-charge region exhibits the same dependence on the forward bias [41], it is generally impossible to distinguish between the two components unless special structures are used.

It is likely however that the junction space-charge region recombination current could be predominantly due to recombination through grain-boundary surface states within the junction space-charge region [33]. The voltage dependence of this current $I_{\text{GB}}^{\text{SCR}}$ can be derived by applying to this part of the grain boundary those portions of our analysis related to (2.10) and (2.30). Generalizing the quasi-equilibrium assumption to mean nearly flat quasi-Fermi-level planes in the space-charge region surrounding the intersection of the grain boundary with the metallurgical junction [8, 33], we have for this case $V_{\text{B}} = V$, and hence from (2.30)

$$I_{\text{GB}}^{\text{SCR}} \propto U_{\text{GB}}^{\text{SCR}} \propto \exp\left(\frac{qV}{2kT}\right) \quad (2.45)$$

where the reciprocal slope factor is exactly two. Thus, (2.45) possibly may facilitate the decomposition of the measured current-voltage characteristic of a polysilicon pn junction and thereby, with the minority-carrier transport model (2.44) developed herein, provide physical insight into the performance of polysilicon bipolar devices and their optimal designs.

From the grain-boundary analysis described in this chapter, it is clear that the boundary condition at the grain boundary adjacent to a quasi-neutral grain is, in general, nonlinear. We will experimentally demonstrate in the next chapter the nonlinearity in $S_{n(\text{eff})}^{\text{GB}}$ using EBIC measurements [21, 22] interpreted quantitatively via a computer-aided numerical solution of the underlying transport problem. Numerical simulation of the EBIC is used because of the complexity of the transport problem, i.e., the three-dimensional continuity equation subject to the nonlinear boundary conditions. With the aid of the grain-boundary model developed in this chapter, we will obtain typical values for $N_{\text{ST}(\text{eff})}^{\text{D}}$ and E_{T} at a grain boundary in Wacker (cast) polysilicon.

CHAPTER 3
DETERMINATION OF GRAIN-BOUNDARY RECOMBINATION VELOCITY
FROM ELECTRON-BEAM-INDUCED-CURRENT MEASUREMENTS

3.1 Introduction

The minority-carrier transport model developed in Chapter 2 reveals that the grain-boundary recombination velocity $S_{n(\text{eff})}^{\text{GB}}$ is, in general, dependent on the excitation level (carrier density) at the grain boundary. This nonlinearity can cause unique current-voltage characteristics for polysilicon diodes. To provide some experimental support for the model, we investigate in this chapter the recombination properties of grain boundaries using the scanning electron microscope (SEM) in the electron-beam-induced-current (EBIC) mode [42]. The EBIC technique has been widely used to measure bulk diffusion length [21, 22, 43-45] and surface properties [21, 22, 24, 46-49] in semiconductor devices.

There are numerous advantages in using EBIC over other forms of excitation to characterize semiconductor devices. The EBIC probe volume has been well investigated and is well defined. For example, the penetration depth of an electron beam is dependent on the atomic number of the semiconductor and is independent of the energy gap [21]. This is in contrast to optical excitation [25], in which the absorption coefficient depends strongly on the energy gap and possibly on the impurity concentration. The EBIC technique is well suited to probe finite semiconductor regions since the excitation volume is small. For

example, in polysilicon the EBIC technique facilitates isolation of a grain boundary from the adjacent quasi-neutral grain without tedious sample preparation, such as fabrication of small-area diodes [16]. Furthermore EBIC is a potentially powerful tool for measuring transport properties near semiconductor surfaces [46, 49], especially in integrated circuits.

In this chapter we will determine $S_{n(\text{eff})}^{\text{GB}}$ at a grain boundary from an analysis of the EBIC response in a grain adjacent to it. The grain boundary is assumed to be perpendicular to the collecting (n^+p) junction, and the electron beam traverses it as illustrated in Fig. 3.1. The quantitative interpretation of the EBIC response requires the solution of the underlying minority-carrier (electron) transport problem in the p-type base, which, in general, is three-dimensional and has nonlinear boundary conditions. The three-dimensionality arises because the carriers are generated over only a finite region in the semiconductor, while the nonlinearity in the boundary condition is due to the dependence of $S_{n(\text{eff})}^{\text{GB}}$ on the excitation as shown in Chapter 2. The existence of a finite hole-electron-pair excitation volume, which, in general, is described by a Gaussian function [47, 50, 51], further complicates the analysis.

The conventional methods to solve the transport problem treat the grain boundary as a surface, which can be justified using the "folding technique" [26]. The EBIC response in the vicinity of a surface perpendicular to the collecting junction was first derived by Van Roosbroeck [52] for the case of a point generation source. Later Berz and Kuiken [25] developed an analytic model by assuming a spherical generation source (volume) and using the method of images. These

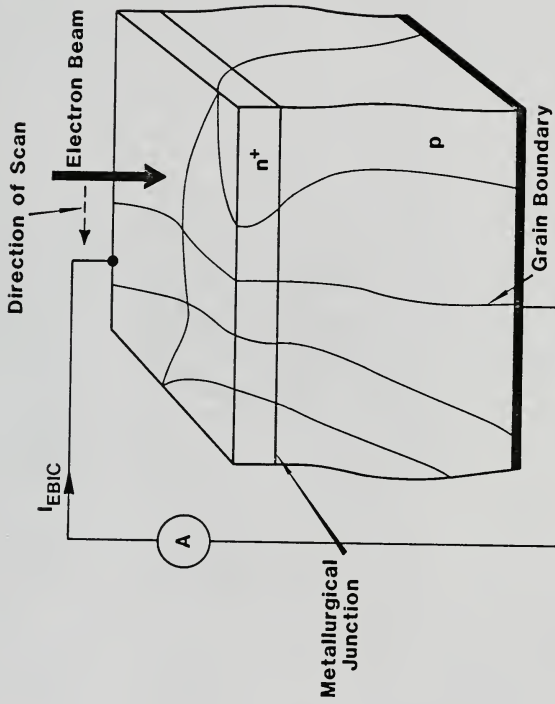


Fig. 3.1 Short-circuited polysilicon n^+p junction with columnar grains and the schematic used to measure the EBIC.

analyses have been used in the determination of minority-carrier lifetime and grain-boundary recombination velocity from EBIC measurements [21, 22, 24, 47]. However the point [52] or the spherical [25] generation-source models do not give a realistic description of the actual electron-beam generation [50]. Furthermore none of the analyses [21, 22, 24-26, 47, 52] account for the nonlinear $S_{n(\text{eff})}^{\text{GB}}$ at the grain boundary, the effects of which depend critically on the generation source.

The approach we take is to solve numerically the minority-carrier transport problem underlying the EBIC response subject to the nonlinear boundary condition at the grain boundary. The three-dimensional, steady-state electron continuity equation is reduced to two dimensions by recognizing that the grains are sufficiently wide (in the y-direction) that the y-dependence of the electron concentration is insignificant (see Fig. 3.2). The solution of the two-dimensional continuity equation yields the electron density, $N(x,z)$. The EBIC collected at the junction, I_{EBIC} , is subsequently calculated. Both the spherical and the Gaussian generation-source models have been considered in the numerical analysis.

Our results, obtained by numerically solving the two-dimensional continuity equation, are in agreement with published analytic solutions [25, 26]. Experimental data obtained on Wacker (cast) polysilicon cells demonstrate the dependence of $S_{n(\text{eff})}^{\text{GB}}$ on the excitation level, which is consistent with the results in Chapter 2. With the aid of the numerical analysis, we predict values for the effective grain-boundary trap density $N_{\text{ST}(\text{eff})}^{\text{D}}$ at passivated (see Chapter 4) and unpassivated grain boundaries in Wacker polysilicon. We also find that using the

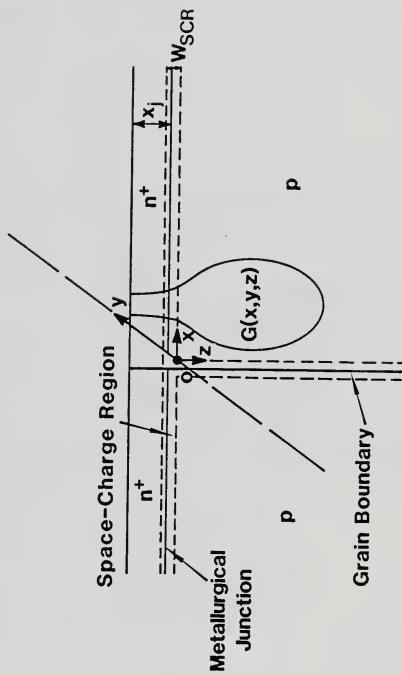


Fig. 3.2 Configuration of an assumed representative grain of the n^+p junction with an illustration of the electron-beam-induced hole-electron-pair generation rate distribution.

assumption of a simplified spherical generation source to predict the EBIC response is valid provided the beam is farther than $2z_0$ from the grain boundary, where z_0 is the penetrating range of the primary electrons [21].

3.2 Formulation of the Problem

The configuration of an assumed representative grain of the polysilicon n^+p junction is shown in Fig. 3.2. The grain is assumed to extend infinitely in the positive x - and z -directions and in the positive and negative y -directions. The metallurgical junction is located at a distance x_j from the SCR edge top surface, and w_{SCR} is the width of the (nearly one-sided) junction space-charge region. The electron beam is incident from the top surface and creates electron-hole pairs over a finite region in the semiconductor. The collection of the electrons, which are assumed to flow only by diffusion, by the junction gives rise to I_{EBIC} . Our objective is to characterize I_{EBIC} , which decreases as the beam moves closer to the grain boundary because of recombination losses there. From the EBIC response we can determine $S_{n(eff)}^{GB}$ at the grain boundaries as well as the electron diffusion length L_n in the grains, which we assume to be everywhere constant.

In order to interpret the EBIC measurements quantitatively, we solve, numerically, the electron transport problem in the p -type base subject to the appropriate boundary conditions. The steady-state continuity equation for electrons when an incident beam of electrons creates $g(x,y,z)$ electron-hole pairs ($\text{cm}^{-3}\text{-sec}^{-1}$) is

$$\nabla \cdot \mathbf{J}_n - qU + qg = 0 \quad (3.1)$$

In (3.1) \bar{J}_n is the electron current density, q is the electron charge, and U is the net thermal recombination rate ($\text{cm}^{-3}\text{-sec}^{-1}$). For a homogeneously doped base under low-level-injection conditions, (3.1) can be written as

$$\frac{\partial^2 N}{\partial x^2} + \frac{\partial^2 N}{\partial y^2} + \frac{\partial^2 N}{\partial z^2} - \frac{N}{L_n^2} + \frac{g(x,y,z)}{D_n} = 0 \quad (3.2)$$

where $N(x,y,z)$ is the excess electron density at any point in the base, D_n is the electron diffusion coefficient, and $L_n = (D_n \tau_n)^{1/2}$ for an electron lifetime τ_n .

Complex analytical solutions of (3.2) have been published for the cases of point- [26], spherical- [25], and Gaussian- [53] generation sources. These solutions are not completely general since they do not account for the nonlinearity in the boundary condition at the grain boundary. The nonlinearity occurs due to the dependence of $S_{n(\text{eff})}^{\text{GB}}$ on the excitation, i.e., N at the grain boundary, given by (2.33). The incorporation of the nonlinear boundary condition complicates the solution of (3.2), and hence we must resort to a computer-aided numerical solution. The direct numerical solution of (3.2) in three-dimensions, however, would involve excessive computer times.

Fortunately, we can reduce (3.2) to a two-dimensional equation that faithfully represents the actual electron transport if the grains are sufficiently wide, i.e., the surfaces in the y -direction are far away ($\sim \infty$). Ascertaining that the EBIC response is invariant along the y -direction (due to the symmetry), Donolato [53] proved mathematically the validity of the simplification of the transport problem from three- to two dimensions. He concluded [53] that the detailed distribution of

the generation function $g(x,y,z)$ along the y -direction does not influence the resulting value of the EBIC, and hence it is sufficient to solve, as we will, the two-dimensional (in x and z) continuity equation to calculate I_{EBIC} . We will show qualitatively that I_{EBIC} in the actual (three-dimensional) case differs from that calculated from our numerical (two-dimensional) analysis by a constant factor for all excitation conditions. This difference does not hinder our quantitative interpretation of the EBIC measurements, e.g., evaluation of $S_{n(\text{eff})}^{\text{GB}}$, since we do not use absolute values of current in our interpretation.

The simplification to two dimensions (x and z) is valid if the flux of electrons in the y -direction is inconsequential. This indeed is generally true with regard to relative value of I_{EBIC} . When the electron beam is far away from the grain boundary, the electrons that diffuse (initially) in the y -direction have virtually the same probability of being collected by the junction, rather than recombining at the grain boundary, as those electrons diffusing in the x -direction toward the grain boundary. For this condition, the y -dependence in (3.2) can be neglected. As the beam is moved close to the grain boundary, the number of electrons that diffuse in the y -direction is small compared to the number that diffuse in the x - (and z -) directions. This is true because the grain-boundary surface (and the junction) is an effective sink for the minority electrons, and hence they tend to diffuse directly towards the grain boundary (or the junction). For this condition also, the y -dependence in (3.2) is not important.

Therefore integrating (3.2) over the y -direction, we get

$$\int_{-\infty}^{\infty} \frac{\partial^2 N}{\partial x^2} dy + \int_{-\infty}^{\infty} \frac{\partial^2 N}{\partial z^2} dy - \frac{1}{L_n^2} \int_{-\infty}^{\infty} N dy + \frac{1}{D_n} \int_{-\infty}^{\infty} g(x,y,z) = 0 \quad (3.3)$$

where, in accord with the above conclusions, we have neglected the y -dependence of the electron concentration, which implies a two-dimensional solution for I_{EBIC} that differs from the actual EBIC by a constant factor. We then simplify (3.3) to

$$K_y \frac{\partial^2 N(x,z)}{\partial x^2} + K_y \frac{\partial^2 N(x,z)}{\partial z^2} - K_y \frac{N(x,z)}{L_n^2} + \frac{G'(x,z)}{D_n} = 0 \quad (3.4)$$

where K_y is an effective y -direction width that serves as a normalizing constant. In (3.4), $N(x,z)$ is the electron concentration obtained from the two-dimensional numerical analysis, and

$$G'(x,z) = \int_{y=-\infty}^{\infty} g(x,y,z) dy \quad (3.5)$$

is the two-dimensional generation-rate function. Dividing (3.4) throughout by K_y , we obtain

$$\frac{\partial^2 N(x,z)}{\partial x^2} + \frac{\partial^2 N(x,z)}{\partial z^2} - \frac{N(x,z)}{L_n^2} + \frac{G(x,z)}{D_n} = 0 \quad , \quad (3.6)$$

which is the differential equation that we solve to obtain the EBIC response. Detailed expressions for $G(x,z)$ for spherical and Gaussian distributions will be given in the next section.

We have thus demonstrated the validity of the simplification of the electron transport problem (3.2) from three- to two-dimensions. Further support for our two-dimensional model is obtained when we compare the

normalized EBIC responses calculated from the three- [25] and the two-dimensional analysis. Excellent agreement between the two (normalized) responses is achieved.

The boundary conditions for this problem are $N(z=0) = 0$ at the edge of the (shorted) junction space-charge region; $N(z \rightarrow \infty) = 0$ since $L_n < W_B$ where W_B is the thickness of the base; $N(x \rightarrow \infty) = 0$ since the grain is semi-infinite ($\gg L_n$) in the x-direction; and at the edge of the grain-boundary space-charge region ($x=0$),

$$D_n \frac{\partial N}{\partial x} = S_{n(\text{eff})}^{\text{GB}} N \quad , \quad (3.7)$$

where $S_{n(\text{eff})}^{\text{GB}}$ is given by (2.33). In (3.7) we have implicitly accounted for the flux of electrons that do not recombine at the grain boundary but flow through it to the adjacent grain. Qualitatively this can be visualized by "folding over" the region to the left of the grain boundary onto that to the right [26], and noting that the electron distributions in the adjacent grains add to yield a solution of (3.6) provided 1) the transport problem is linear, 2) L_n is the same in both grains, and 3) quasi-equilibrium prevails across the grain-boundary space-charge region. When these conditions obtain, the grain-boundary recombination is properly characterized by (3.6) and (3.7) provided $N(x,z)$ is recognized to be the folded sum of the left- and right-side solutions. This is shown to be mathematically valid in Appendix B. From the numerical solution $N(x,z)$ of (3.6) we calculate the EBIC collected at the junction:

$$I_{\text{EBIC}} = qK_y D_n \int_0^{\infty} \left. \frac{\partial N}{\partial z} \right|_{z=0} dx \quad . \quad (3.8)$$

3.3 The Volume Distribution of the Generation Rate

Before we solve (3.6), it is important to model the volume distribution of the electron-beam-induced hole-electron-pair generation rate $G(x,z)$. The simplest representation is a point-source excitation [21, 26, 52], i.e., the electron-hole pairs are generated at a point in the base. The distance of the point-source from the junction is determined by the energy of the incident electron beam. It is obvious that the point-source generation model does not represent the actual generation.

Improved models for the excitation volume have been proposed. A spherical generation source [24, 25] has been suggested as a reasonable representation of the actual generation distribution. More sophisticated models such as the radial Gaussian [50] and the spherical Gaussian [51] have been proposed and have been shown to be more generally reliable than the spherical generation-source model. In our analyses we consider two cases: 1) a spherical generation source [24, 25]; and 2) a more complicated radial Gaussian generation source [50]. The reason for analyzing the spherical generation source is that it is easier to implement it numerically than the Gaussian source, and, as we see later, the results obtained by assuming a spherical generation source are in agreement with those obtained by assuming a Gaussian source, provided the beam is far away from the grain boundary. Any uncertainties resulting from assuming a spherical source model, particularly related to the dependence of $S_{n(eff)}^{GB}$ on the excitation, will be removed by the Gaussian source model.

3.3.1 Spherical Generation Source

The electron beam incident from the top surface, is assumed to generate electron-hole pairs in a spherical volume [25]. In our numerical analysis, in which we have reduced the transport problem to a two-dimensional differential equation (in the xz -plane), the source is a circle as shown in Fig. 3.3. The radius of the circle, r_G , is much smaller than the electron diffusion length in the base, and the generation rate at any point inside the circle is assumed to be independent of position [25]:

$$G = G_0 / \pi r_G^2 K_y \quad (3.9)$$

where G_0 is the total number of electron-hole pairs per unit time generated by the electron beam, and K_y is the normalizing constant in (3.4).

The center of the circle is located at a distance $z_0/3$ from the top surface, where [21]

$$z_0 = C E_0^{1.75} \quad (3.10)$$

is the primary electron range, i.e., the penetration of the primary electrons in the z -direction. In (3.10) E_0 is the energy of the beam in kilo-electron-volts (keV), and C is a constant which is dependent on properties of the semiconductor [21]:

$$C = \frac{4}{\rho} \times 10^{-6} \quad (3.11)$$

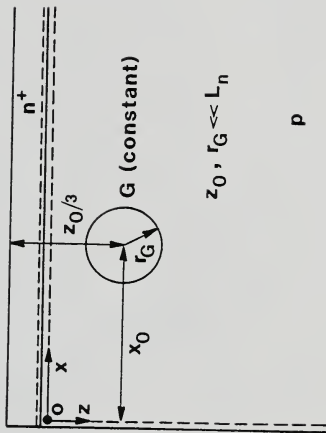


Fig. 3.3 Schematic of the polysilicon grain with a circular hole-electron-pair generation source.

where ρ is the (mass) density of the semiconductor. For silicon $C = 0.0171 \times 10^{-4}$, which yields $z_0 = 8.6 \mu\text{m}$ for $E_0 = 35 \text{ keV}$. The physical reason for using a circular generation source centered at a distance $z_0/3$ from the top surface will be explained in the next subsection.

3.3.2 Gaussian Generation Source

When high-energy electrons penetrate the semiconductor, the electron-hole pairs are generated over a characteristic pear-shaped volume rather than over a spherical volume [50]. The reason for this is that the energy dissipation of the incident electrons has been experimentally shown to be given by the Gruen's function [54] in the depth coordinate, i.e., in the z -direction. The Gruen's function is a third-degree polynomial in z and has a maximum at a depth determined by the energy of the incident beam. These results have also been verified by Monte Carlo simulations [55]. Hence, in our analysis, we will assume that the distribution in the z -direction is adequately described by the Gruen's function.

In the radial (x -) direction, we will assume that the carrier generation follows a Gaussian distribution [50]. The Gaussian distribution has been used to reliably model carrier generation due to X-rays produced by an electron beam [56] and successfully in electron lithography studies [50]. The amplitude A and the width σ of the Gaussian function will depend on z and z_0 . The generation rate at any point can then be expressed as [50]

$$G(x, z) = \frac{A(z, z_0)}{K_y 2 [2\pi\sigma^2(z, z_0)]^{1/2}} \exp\left[-\frac{(x-x_0)^2}{2\sigma^2(z, z_0)}\right] \quad (3.12)$$

where K_y is the normalizing constant in (3.4). The expression for G in (3.12) has been proposed by Donolato [50]. Expressions for A and σ will be given shortly. Note in (3.12) that G is independent of the y -direction since the transport problem has been reduced to two dimensions. The actual generation in the y -direction is accounted for implicitly by matching the experimentally measured and the theoretically calculated values of the maximum EBIC (at a point well inside the grain) to obtain the theoretical EBIC response, $I_{EBIC}(x)$.

A property of (3.12) is

$$\int_{x=-\infty}^{\infty} G(x,z) dx = A(z,z_0)/K_y \quad . \quad (3.13)$$

From (3.10) and (3.13) we can infer that $A(z,z_0)$ represents the relation between the penetration depth of the electron beam and its energy [54]. An expression for $A(z,z_0)$ has been experimentally obtained [50, 54],

$$A(z,z_0) = \frac{G_0}{z_0 K_y} [\Lambda(z/z_0)] \quad , \quad (3.14)$$

where $\Lambda(z/z_0)$ is the Gruen's function [50, 54]:

$$\begin{aligned} \Lambda(z/z_0) &= 0.6 + 6.21(z'/z_0) - 12.4(z'/z_0)^2 \\ &\quad + 5.69 (z'/z_0)^3 \quad \text{for } 0 < z' < 1.1 z_0 \\ &= 0 \quad \text{for } z' > 1.1 z_0 \quad ; \end{aligned} \quad (3.15)$$

in (3.15), $z' \triangleq z + (x_j + W_{SCR})$. Since this form for Λ yields a unity integral between 0 and $1.1 z_0$, integration of (3.15) in the range $0 < z' < \infty$ correctly yields G_0/K_y . In Fig. 3.4 we have plotted $A(z, z_0)$ for $E_0 = 35$ keV. We see that the maximum value of $A(z, z_0)$ occurs at $z_0/3$ from the top surface ($z' \approx z_0/3$), where $z_0 = 8.6 \mu\text{m}$. This observation qualitatively justifies the earlier assumption that the center of the approximate circular generation volume is at $z' \approx z_0/3$.

The width of the Gaussian for a finite value of the beam diameter is given by [50]

$$\sigma^2(z, z_0) = 0.36 d^2 + 0.11 (z')^3/z_0 \quad (3.16)$$

where d is the beam diameter. For EBIC measurements, typically $d = 500\text{-}1000 \text{ \AA}$. The complete expression for G adopted in our numerical analysis is ($0 < z < 1.1 z_0$)

$$G(x, z) = \frac{G_0/K_y}{2z_0} \frac{\Lambda(z/z_0)}{[2\pi\sigma^2(z, z_0)]^{1/2}} \exp\left[-\frac{(x - x_0)^2}{2\sigma^2(z, z_0)}\right] \quad (3.17)$$

where $\Lambda(z, z_0)$ and $\sigma^2(z, z_0)$ are described by (3.15) and (3.16). In Fig. 3.5 we have plotted G as a function x for various values of z . These plots have been drawn for $x_0 = 30 \mu\text{m}$ and $E_0 = 35$ keV.

3.4 Results

The computer-aided numerical solution of (3.6), subject to the given boundary conditions, was obtained by using a finite-difference approximation technique [57, 58]. The grain is divided into rectangular grids and the differential equation (3.6) is approximated by its finite-

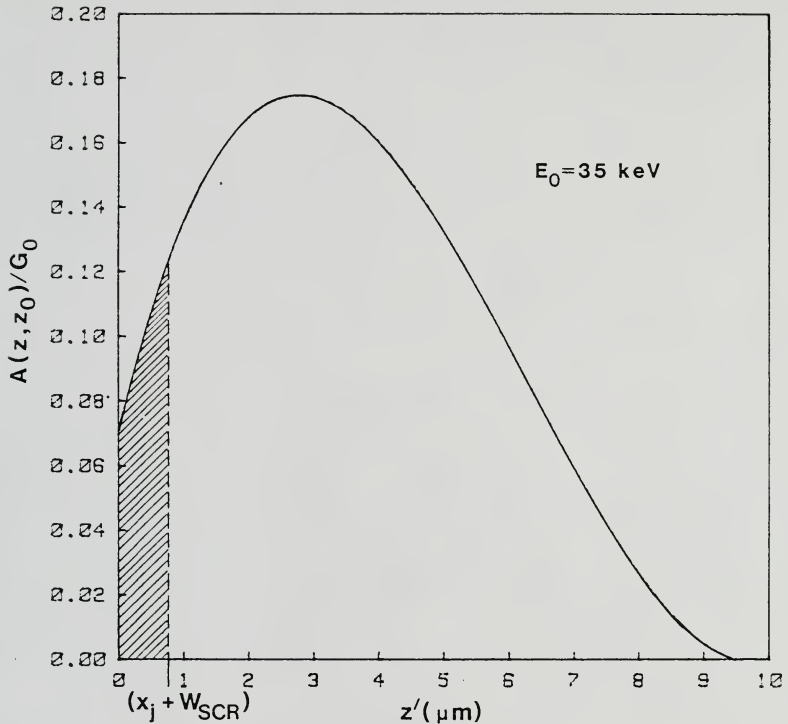


Fig. 3.4 The pre-exponential coefficient $A(z, z_0)$ of the Gaussian generation distribution versus the depth coordinate. The shaded area indicates the total generation in the emitter and the junction space-charge region. For our cells, $(x_j + W_{\text{SCR}}) \approx 0.8 \mu\text{m}$, within which only about 6% of the total generation occurs.

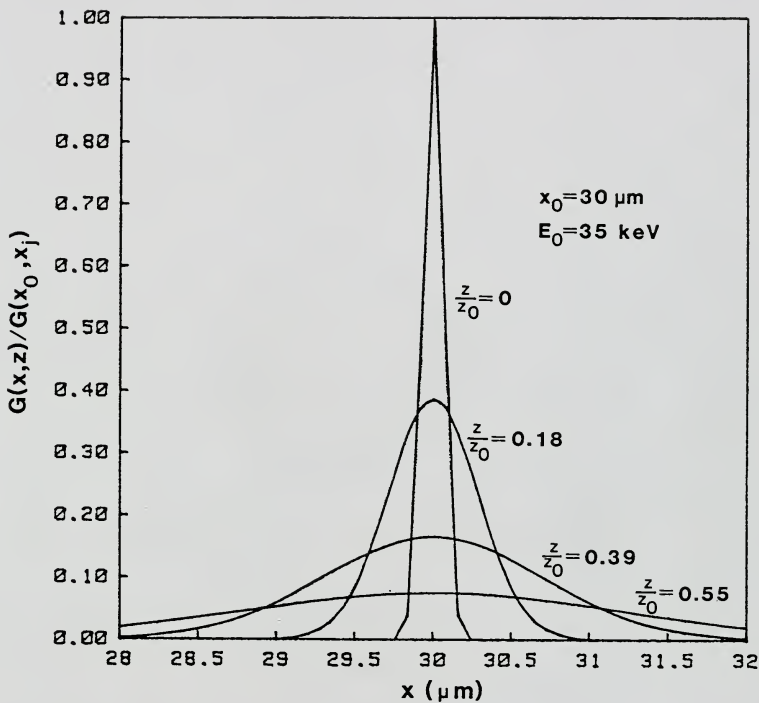


Fig. 3.5 The generation rate (assumed to be a radial Gaussian) as a function of the distance x from the grain boundary at different depths z .

difference form at each grid point. The resultant set of algebraic equations is combined with that at the boundaries and solved simultaneously using the Gauss-Seidel elimination method with successive overrelaxation [57, 58]. The EBIC current (3.8) is calculated by numerically differentiating $N(x,0)$ and integrating it over the area of the junction. Salient features of the numerical algorithm are described in Appendix C, wherein we have also listed the Fortran computer program.

Typically EBIC measurements are performed on shallow-junction devices. In such devices we can assume that the generation in the quasi-neutral emitter and the junction space-charge region is much smaller than the total generation. Hence the EBIC due to generation of carriers in the quasi-neutral emitter and the junction space-charge region, which is a constant, can be neglected. For example, in the Wacker polysilicon cells used in our experiments $x_j \approx 0.4 \mu\text{m}$ and $W_{\text{SCR}} \approx 0.4 \mu\text{m}$. The value of x_j was inferred from sheet resistivity measurements, while the value of W_{SCR} was determined from the zero-bias capacitance measurements performed on the completed cell. From Fig. 3.4 we note that the generation in the emitter and the junction space-charge region is about 6% of the total generation (in the entire cell), which is negligible.

The calculated I_{EBIC} as a function of the beam position is plotted in Figs. 3.6 and 3.7 for two different values of the background EBIC excitation level, i.e., maximum I_{EBIC} produced when the beam is far removed from the grain boundary:

$$I_{\text{EBIC}}^{\text{MAX}} = qK_y \int_0^{\infty} \int_0^{\infty} \left[G(x,z) - \frac{N(x,z)}{\tau_n} \right] dx dz \quad (3.18)$$

where G is given by (3.17). These plots have been drawn subject to the condition that $S_{n(\text{eff})}^{\text{GB}}$ is dependent on the excitation as described by (2.33). Note that the theoretical EBIC responses in Figs. 3.6 and 3.7 as well as the experimental data pertain to the same grain.

Superimposed on the theoretical plots in Figs. 3.6 and 3.7 are the measured EBIC responses of a typical grain in a standard (unpassivated) polysilicon n^+p cell, the fabrication of which will be described in the next chapter. The two parameters L_n and $N_{\text{ST}(\text{eff})}^{\text{D}}$ are determined simultaneously by fitting the experimental data at one current level; the fits at other current levels provide a check on the model, i.e., the nonlinear $S_{n(\text{eff})}^{\text{GB}}$ and the constant L_n . By comparing the theoretical and experimental responses, we infer that $L_n = 120 \mu\text{m}$ and that $N_{\text{ST}(\text{eff})}^{\text{D}} = 1 \times 10^{12} \text{ cm}^{-2}$ for the grain measured.

The error bars shown in Figs. 3.6 and 3.7 as well as in the other figures to follow reflect the uncertainty in the measurement of the distance, x_0 , of the generation volume from the center of the grain boundary. This uncertainty is due to the difficulty in being able to locate the center of the grain boundary in our measurements.

In Figs. 3.6 and 3.7, we have also plotted theoretical EBIC responses based on a constant $S_{n(\text{eff})}^{\text{GB}}$. The assumption of a constant $S_{n(\text{eff})}^{\text{GB}}$ seems to be a reasonable one when the beam is sufficiently far away from the grain boundary. However, as is clear from Figs. 3.6 and 3.7, the EBIC responses for the constant $S_{n(\text{eff})}^{\text{GB}}$ case deviate from the experimental data as the beam approaches the grain boundary. The physical reason for this deviation is evident from Fig. 3.8, where we have plotted $S_{n(\text{eff})}^{\text{GB}}$ versus x_0 for the two different excitation levels in Figs. 3.6 and 3.7. As the beam nears the grain

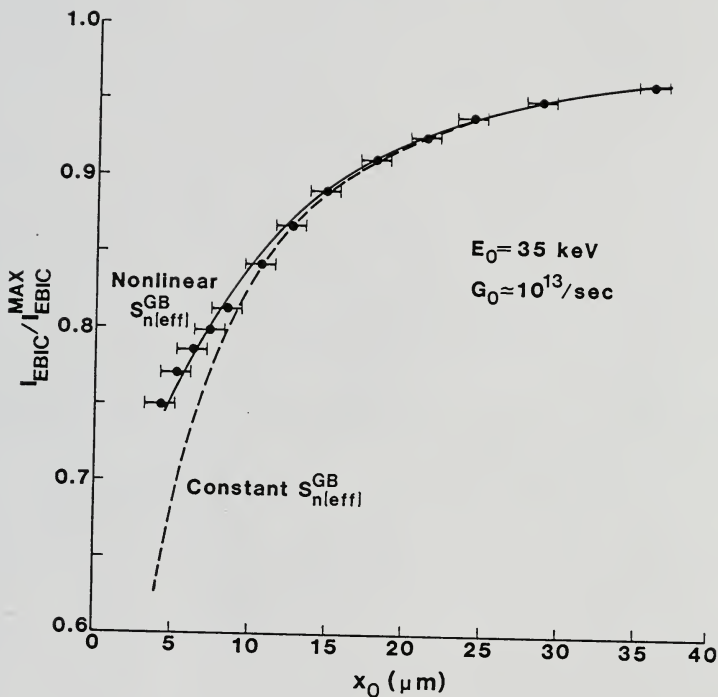


Fig. 3.6 Calculated and measured (\bullet) EBIC (normalized) from a grain in the vicinity of an unpassivated grain boundary ($G_0 \approx 10^{13}/\text{sec}$). The EBIC has been calculated for constant (---) and nonlinear (—) $S_{n(eff)}^{GB}$.

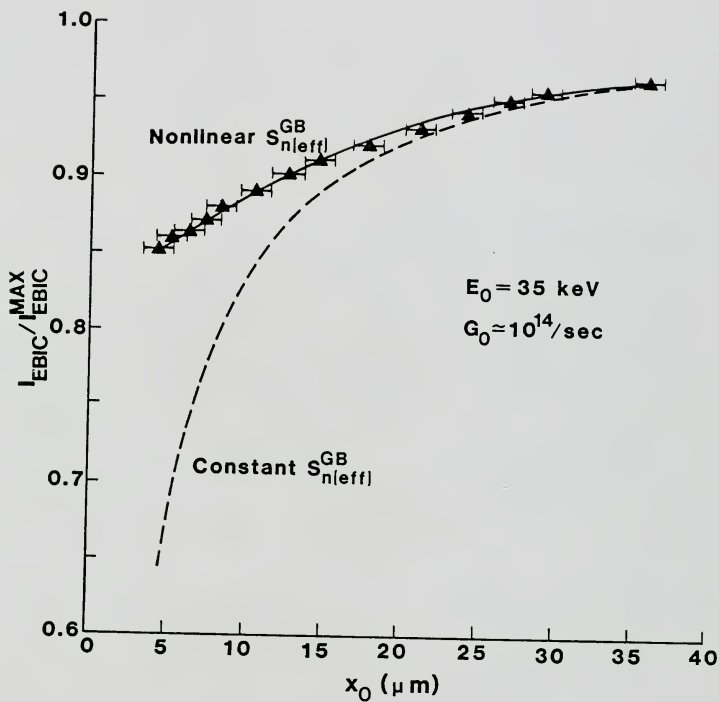


Fig. 3.7 Calculated and measured (\blacktriangle) EBIC (normalized) from a grain in the vicinity of an unpassivated grain boundary ($G_0 \approx 10^{14}/\text{sec}$). Note the significance of the nonlinearity when the electron beam is near the grain boundary.

boundary we find that $S_{n(\text{eff})}^{\text{GB}}$ decreases due to the increase in excitation, i.e., $N(0,z)$, at the grain boundary. Consequently the actual EBIC collected by the junction at any beam position is higher than that predicted by the unrealistic constant- $S_{n(\text{eff})}^{\text{GB}}$ curves. This demonstrates the significant nonlinearity in $S_{n(\text{eff})}^{\text{GB}}$ in accord with our theoretical results in Chapter 2.

We also note from Figs. 3.6 and 3.7, which pertain to the same grain, that the value of $S_{n(\text{eff})}^{\text{GB}}$ inferred by comparing the theoretical (constant $S_{n(\text{eff})}^{\text{GB}}$) and experimental responses, is not unique; different values are implied at the same grain boundary at different current levels when $S_{n(\text{eff})}^{\text{GB}}$ is assumed to be a constant. This further demonstrates the nonlinearity and shows that a constant- $S_{n(\text{eff})}^{\text{GB}}$ model is physically unreasonable. We note that when the nonlinearity in $S_{n(\text{eff})}^{\text{GB}}$ is accounted for, comparison of theoretical and experimental results yields a unique value for $N_{\text{ST}(\text{eff})}^{\text{D}}$; the nonlinear model is thus physically reasonable.

The nonlinearity in $S_{n(\text{eff})}^{\text{GB}}$ is further confirmed when we compare the experimental data measured at the two different excitation levels (Figs. 3.6 and 3.7). The increased excitation (G_0) was obtained by increasing the beam current and keeping the beam energy constant. (The increase in the beam diameter with excitation level [42] is inconsequential since the second term on the right side of (3.16) is always dominant.) If $S_{n(\text{eff})}^{\text{GB}}$ were a constant then the percentage EBIC collected by the junction at any given x_0 should be independent of the excitation level [25, 47]. However the experimental data in Figs. 3.6 and 3.7 show a strong dependence on the excitation level. For the same value of x_0 we observe that the percentage EBIC lost at the grain

boundary at the lower excitation level (Fig. 3.6) is higher than that at the higher excitation level (Fig. 3.7). The reason for this is obvious from Fig. 3.8 wherein we have plotted $S_{n(\text{eff})}^{\text{GB}}$ as a function of x_0 at the two excitation levels for the grain boundary in the standard cell. From Fig. 3.8 we note that $S_{n(\text{eff})}^{\text{GB}}$ at the grain boundary in the standard cell is lowered by about an order of magnitude at the higher excitation level. Hence we conclude that the nonlinearity in $S_{n(\text{eff})}^{\text{GB}}$ influences the EBIC response when the beam is close to the grain boundary and should be accounted for to ensure accurate quantitative interpretation of EBIC measurements.

In Figs. 3.9 and 3.10 we compare the theoretical plots with the experimental data obtained in a grain of an aluminum-passivated (active) n^+p cell. The passivation technique will be described in the next chapter. By comparing the experimental data with the theoretical plots, which were obtained by assuming G to be a Gaussian given by (3.17), we infer that $N_{\text{ST}(\text{eff})}^{\text{D}} \approx 10^{11} \text{ cm}^{-2}$ at a passivated grain boundary. Once again we observe that $S_{n(\text{eff})}^{\text{GB}}$ is nonlinear. However the nonlinearity is less pronounced than at the unpassivated grain boundaries in a standard cell, particularly at the low excitation level. An explanation for this can be provided using the grain boundary analysis in Chapter 2. For low $N_{\text{ST}(\text{eff})}^{\text{D}}$, $\phi_B = \phi_{B0}$, which implies that $S_{n(\text{eff})}^{\text{GB}} (= C_1 N_{\text{ST}(\text{eff})}^{\text{D}})$ is virtually constant.

The theoretical EBIC response obtained in a grain in the vicinity of an unpassivated grain boundary is compared to the experimental data in Fig. 3.11. We infer that at this grain boundary, $N_{\text{ST}(\text{eff})}^{\text{D}} \approx 10^{14} \text{ cm}^{-2}$, which suggests that this particular grain boundary is a high-angle boundary. This value of $N_{\text{ST}(\text{eff})}^{\text{D}}$ is unusually

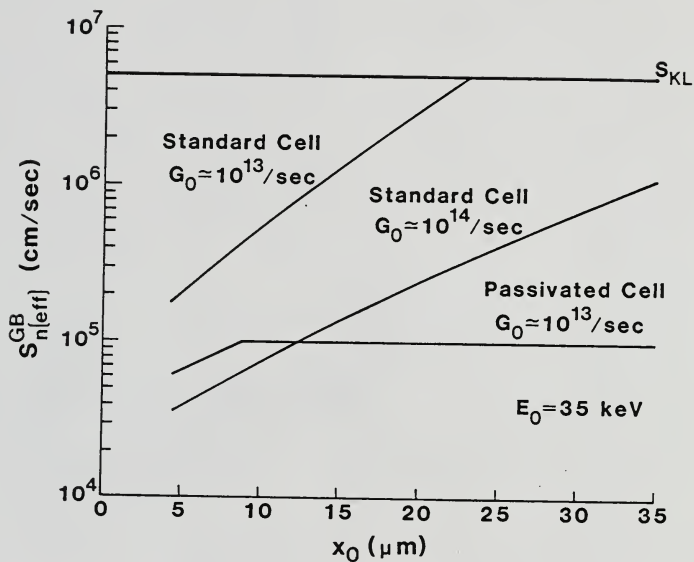


Fig. 3.8 The grain-boundary effective recombination velocity as a function of x_0 at unpassivated and passivated grain boundaries. These plots show how $S_{n(\text{eff})}^{\text{GB}}$ changes as the electron beam moves toward (excites) the grain boundary.

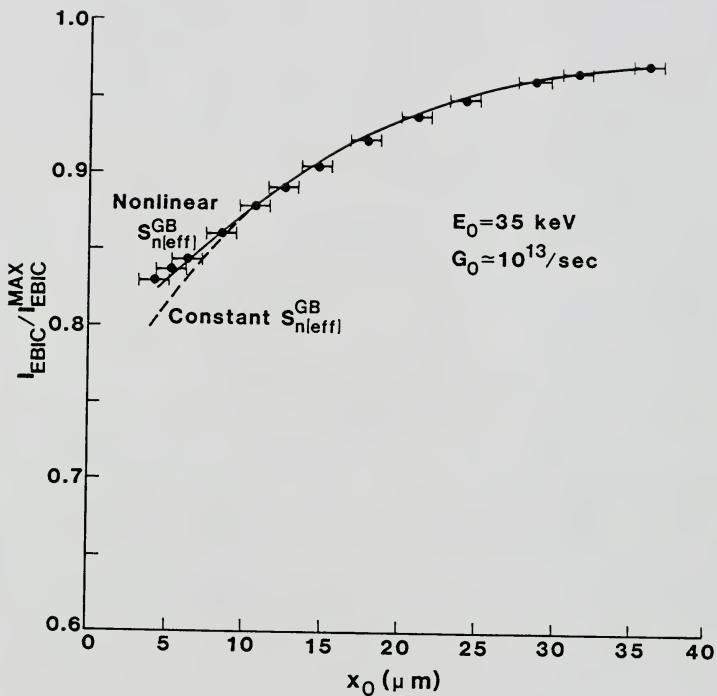


Fig. 3.9 Calculated and measured (\bullet) EBIC (normalized) from a grain in the vicinity of a passivated grain boundary ($G_0 \approx 10^{13}/\text{sec}$).

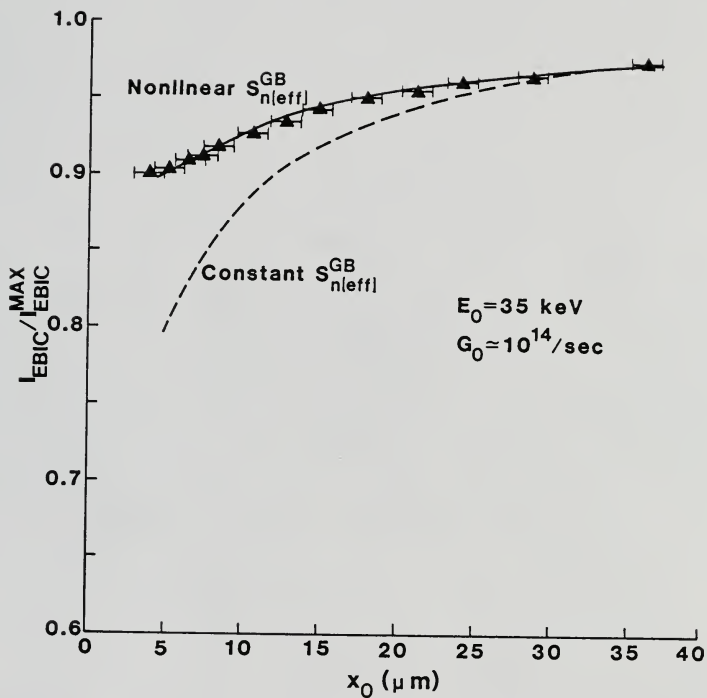


Fig. 3.10 Calculated and measured (\blacktriangle) EBIC (normalized) from a grain in the vicinity of a passivated grain boundary ($G_0 \approx 10^{14}/\text{sec}$).

high, possibly because of our assumption that $N_{ST(eff)}^D$ is monoenergetic situated at midgap. The large value of $N_{ST(eff)}^D$ causes ϕ_B to be high. Consequently the value of $S_{n(eff)}^{GB}$ does not vary significantly with the excitation level and is at the kinetic limit as described in Chapter 2.

In Fig. 3.12 we have plotted the theoretical EBIC response obtained by assuming a circular generation source. Comparing it to the Gaussian-generation-source case, we observe that the circular-generation assumption is good provided we interpret data far away ($\sim 2z_0$) from the grain boundary. As the beam approaches the grain boundary the predicted EBIC responses in the two cases differ from each other. If we interpret the experimental data in Fig. 3.6 using the circular generation source assumption we find that $N_{ST(eff)}^D = 2 \times 10^{12} \text{ cm}^{-2}$, which is a factor of two higher than that obtained by assuming a Gaussian generation source.

3.5 Discussion

In this chapter we determined $S_{n(eff)}^{GB}$ at typical passivated and unpassivated grain boundaries in Wacker (cast) polysilicon from EBIC measurements. We demonstrated the dependence of $S_{n(eff)}^{GB}$ on the excitation level as predicted by the transport model developed in Chapter 2.

In order to facilitate quantitative interpretation of EBIC measurements we solved, using computer-aided numerical analysis, the underlying transport problem. The general transport problem in three dimensions was reduced to one in two-dimensions by neglecting the variations in the (y-) direction normal to the plane defined by the moving electron beam. This assumption is justified since the surfaces

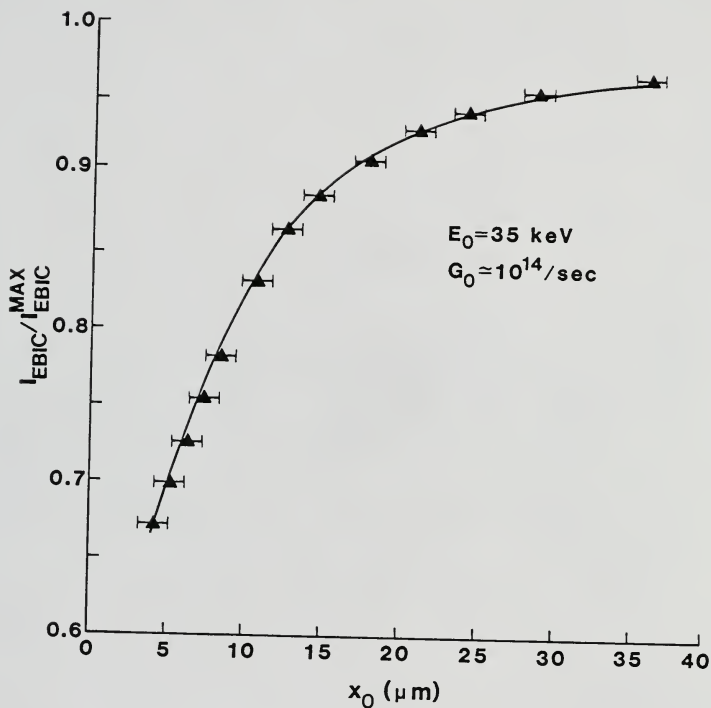


Fig. 3.11 Calculated and measured (\blacktriangle) EBIC (normalized) from a grain in the vicinity of an unpassivated (high-angle) grain boundary ($G_0 \approx 10^{14}$ /sec); $S_n^{GB}(\text{eff})$ is virtually constant ($\approx S_{KL}$) due to high $N_{ST}^D(\text{eff})$ ($\approx 10^{14}$ cm $^{-2}$).

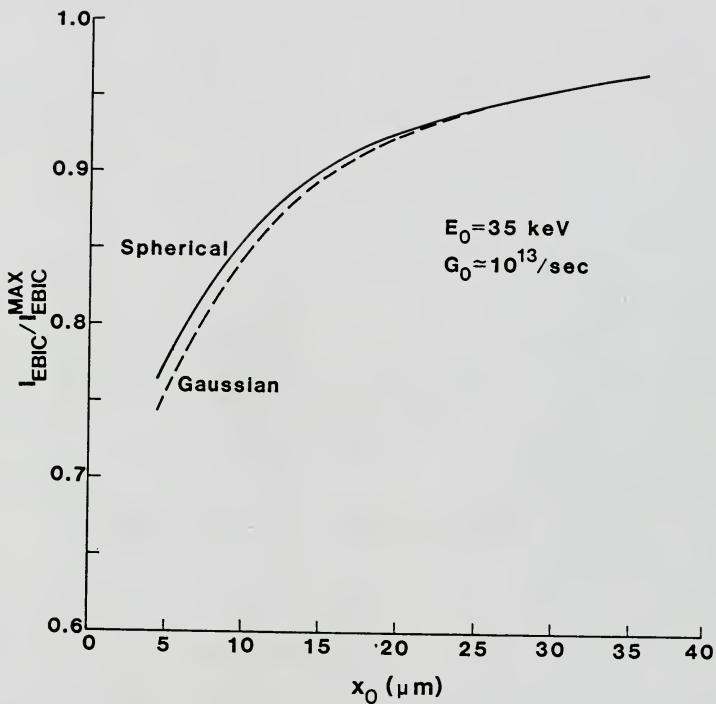


Fig. 3.12 Comparison of the calculated EBIC (normalized) as a function of x_0 for two different models for the hole-electron-pair generation volume.

in the y -direction are far removed from the excitation volume. We found that the discrepancy between the actual solution and ours is a constant factor in I_{EBIC} provided the y -dependence in (3.2) can be neglected, which was justified qualitatively. Our quantitative interpretation of $S_{n(eff)}^{GB}$ is not hindered due to this constant difference since we compare only relative values of EBIC current. The results of the two-dimensional analysis agree well with published analytic solutions [25, 26, 52]. The simplification of the transport problem from three- to two-dimensions has also been shown to be mathematically valid [53].

In our analyses, we have incorporated two different models for the hole-electron-pair excitation volume: 1) the spherical generation-source model [24, 25]; and 2) the Gaussian generation-source model [50]. The utility of the spherical-source model results from its ease of implementation in the numerical analysis. The EBIC response obtained by using this model far away from the grain boundary agrees well with that obtained by using the sophisticated and hence more complicated Gaussian-source model. Thus the spherical-source model is useful for interpreting EBIC data far away from the grain boundary when $S_{n(eff)}^{GB}$ is a constant (e.g., when $S_{n(eff)}^{GB} = S_{KL}$ or at passivated grain boundaries).

In the spherical-source model the incident electron beam generates hole-electron pairs in the base in a sphere (circle in the two-dimensional analysis) whose radius is much smaller than the electron diffusion length and within which the generation rate is a constant [25]. To remove any uncertainties associated with the spherical-source assumption [47, 50, 51], we also modeled the excitation volume using a radial Gaussian distribution [50], i.e., at any depth z , G is given by a Gaussian function. In the z -direction the distribution is given by the

Gruen's function [50, 54]. This description of the generation source is more generalized and better represents the actual generation than the simplified spherical-source model.

The analytic solution of the two-dimensional continuity equation (3.6) in the general case of nonlinear $S_{n(\text{eff})}^{\text{GB}}$ and a Gaussian generation source is formidable. Hence we resorted to a computer-aided numerical solution. The solution was obtained by approximating (3.6) using finite differences [57, 58]. The resultant set of algebraic equations was solved by the Gauss-Seidel elimination method [57, 58]. The EBIC current collected at the junction was calculated as a function of x_0 , $S_{n(\text{eff})}^{\text{GB}}$, and $N_{\text{ST}(\text{eff})}^{\text{D}}$. In the analyses we have treated the grain boundary as a surface, which can be justified by using the folding technique [26].

The EBIC response of (aluminum-) passivated and unpassivated Wacker (cast) polysilicon cells were measured experimentally. The cell fabrication and the passivation technique will be described in the next chapter. When the beam is situated close to the grain boundary we observed that I_{EBIC} measured experimentally was higher than predicted by the theoretical plots for constant $S_{n(\text{eff})}^{\text{GB}}$. This clearly demonstrates, subject to our assumption of constant L_n which was indeed supported by our results, that the dependence of $S_{n(\text{eff})}^{\text{GB}}$ on the excitation level as predicted in Chapter 2. We also observed that the current loss at the grain boundary for a given x_0 decreased with increasing excitation level. This provides further evidence for the nonlinearity. Physically, $N(0,z)$ increases as the beam approaches the grain boundary or as the incident excitation level is increased. Consequently, $S_{n(\text{eff})}^{\text{GB}}$, which is proportional to $[N(0,Z)]^{1/2}$, decreases and hence

I_{EBIC} is higher than predicted by constant $S_{n(\text{eff})}^{\text{GB}}$ curves (see Figs. 3.6, 3.7, 3.9, 3.10).

By comparing the experimental data with the theoretical plots we inferred that $N_{\text{ST}(\text{eff})}^{\text{D}} \approx 10^{12} \text{ cm}^{-2}$ at a typical unpassivated grain boundary and $N_{\text{ST}(\text{eff})}^{\text{D}} \approx 10^{11} \text{ cm}^{-2}$ at a passivated grain boundary. The comparison of the theoretical and experimental EBIC responses also yielded values for the diffusion lengths in the grains simultaneously. For the grain of the unpassivated cell, $L_n \approx 120 \text{ }\mu\text{m}$, while for the grain of the passivated cell, $L_n \approx 110 \text{ }\mu\text{m}$. The determinations of $N_{\text{ST}(\text{eff})}^{\text{D}}$ were based on the assumption that the trap level, E_T , is at midgap ($E_T = E_i$). If E_T were below E_i [34], the value of $N_{\text{ST}(\text{eff})}^{\text{D}}$ would be higher than that predicted by our numerical analysis. The dependence of $S_{n(\text{eff})}^{\text{GB}}$ on the excitation level, however, remains unaltered and is given by (2.33), provided E_T is located relatively deep in the energy gap, i.e., $\approx 5 \text{ kT}$ below E_i (see Chapter 2).

Our analyses predict that the spherical generation-source assumption adequately describes the EBIC response provided $x_0 \gtrsim 2z_0$. For $x_0 < 2z_0$, the response for a spherical source differs from that for a Gaussian source and could cause at least a factor of two difference in the determination of $N_{\text{ST}(\text{eff})}^{\text{D}}$. The reason for the discrepancy is that the spherical source cannot accurately describe the nonlinearity in $S_{n(\text{eff})}^{\text{GB}}$, which becomes important as the beam approaches the grain boundary. For $x_0 \gtrsim 2z_0$, the influence of the grain boundaries on the EBIC response is minimal and hence the response is independent of the choice of the generation source. The use of the spherical-source model, which is easy to implement and is widely used in most analyses [24, 25, 47], is recommended to interpret EBIC data far away from the grain

boundary. The model yields reliable results when $S_{n(\text{eff})}^{\text{GB}}$ is a constant, e.g., at a passivated grain boundary or when $S_{n(\text{eff})}^{\text{GB}} = S_{\text{KL}}$.

In Chapter 2 we studied grain-boundary recombination and its influence on the base recombination current of a polysilicon diode. In this chapter we described an experimental technique to determine $S_{n(\text{eff})}^{\text{GB}}$, which is a measure of the grain-boundary recombination. It is obvious that grain-boundary recombination deteriorates the performance of bipolar polysilicon devices. For example in a polysilicon solar cell, the grain-boundary recombination both in the junction space-charge region as well as adjacent to the quasi-neutral base can limit the cell efficiency [8]. In order to improve polysilicon device performance it is necessary to suppress grain-boundary recombination. Such suppression will also likely reduce carrier scattering by grain boundaries which lowers ϕ_B at the grain boundaries. This results in an improvement of the carrier mobility in polysilicon [5], for example that used in integrated circuits [3].

In the next chapter we suggest an experimental method to reduce grain-boundary recombination by passivating grain boundaries using preferential diffusion of aluminum. The passivation is assessed by comparing the EBIC response in the vicinity of an unpassivated and a passivated grain boundary. The value of $S_{n(\text{eff})}^{\text{GB}}$ is determined from the EBIC measurements with the aid of the numerical solution of the transport problem described in this chapter. Possible additional benefits of aluminum, such as gettering, are also examined.

CHAPTER 4
POTENTIAL IMPROVEMENT OF POLYSILICON SOLAR CELLS
BY GRAIN-BOUNDARY AND INTRAGRAIN DIFFUSION OF ALUMINUM

4.1 Introduction

The conversion efficiency of polycrystalline silicon (polysilicon) solar cells, as pointed out in Chapter 2, is limited by high defect densities within the grains as well as at the grain boundaries. On the one hand, the efficiency of bulk polysilicon cells having relatively large grains is generally limited by high densities of intragrain defects that cause short minority-carrier lifetimes; the grain-boundary recombination is hence rendered virtually unimportant. The efficiency of thin-film polysilicon cells having relatively small grains may, on the other hand, be generally limited by high densities of grain-boundary traps that produce high recombination velocities. It is therefore of interest to consider processes that could possibly passivate the grain boundaries, i.e., reduce the grain-boundary trap densities, and also getter the grains, i.e., remove defects (impurities) from the active portions of the grains. Such a process is perhaps the diffusion of a specific impurity whose grain-boundary diffusion coefficient is higher than its bulk coefficient, which implies preferential grain-boundary diffusion [59], and whose presence at the silicon surface increases the solubility of common defects, which implies bulk-to-surface transfer of defects.

Phosphorous, which is an effective gettering agent in silicon [60], also has the potential to be an effective grain-boundary passivating agent [16]. However preferential grain-boundary diffusion of phosphorous much deeper than $\sim 10 \mu\text{m}$ is not practical because it must be done at a temperature ($> 1000^\circ\text{C}$) considerably higher than the normal solar cell junction-formation temperature ($< 900^\circ\text{C}$). It has been shown that lithium tends to suppress grain-boundary recombination, but its stability and effectiveness are dubious [17]. Monatomic hydrogen has been shown to be extremely effective in passivating grain boundaries [18], but the necessity of inordinate sample preparation and the unorthodox nature of the hydrogenation process make it impractical in solar cell fabrication. Passivation of grain boundaries has also been achieved using deuterium [19] but, as is hydrogenation, the incorporation of deuterium into the polysilicon is incompatible with conventional solar cell processing. Hence it would be useful to design a process that 1) is compatible with conventional solar cell fabrication; 2) passivates most of the grain boundaries in a relatively short time; and 3) produces concomitant gettering of intragrain defects.

There are indications that aluminum, an acceptor-type dopant in silicon, could be an ideal agent for improving polysilicon solar cell efficiency. Evidence of anomalous diffusion of and gettering by aluminum in silicon dates back to the initial development of the aluminum-alloyed n^+pp^+ back-surface-field (BSF) silicon solar cell [61]. More recently unusually high grain-boundary diffusion coefficients for aluminum in polysilicon have been measured [62], and unexpected improvements in the spectral response of "bicrystalline" silicon cells having aluminum "BSFs" have been observed [63].

The passivation of a grain boundary by preferential aluminum diffusion might occur via 1) reduction of the grain-boundary (deep-level) trap density resulting from removal of dangling bonds; 2) formation of a high-low junction at the grain boundary, which reduces the effective recombination velocity $S_{n(\text{eff})}^{\text{GB}}$ (see Chapter 2); and/or 3) formation of a pn junction at the grain boundary, which effectively increases the collecting junction area. It is possible then that aluminum diffusion, which is compatible with solar cell fabrication, could improve polysilicon solar cells by passivating grain boundaries as well as by gettering intragrain impurities and by creating an effective BSF.

In this chapter we present results of experiments designed to study the effects of aluminum diffusion on the efficiency of both bulk and thin-film polysilicon solar cells. In the case of bulk polysilicon, which possibly may soon be a cheap substitute for silicon in solar cell technology, we focus our attention on the conventional Al-BSF process [61, 64], which should ultimately yield the highest attainable efficiencies as it has in silicon cells [65]. Possible additional benefits due to the back aluminum diffusion (alloying), e.g., gettering and grain-boundary passivation, are investigated. With regard to thin-film polysilicon, we examine gettering and grain-boundary passivation resulting from aluminum diffusion at low temperatures (below the eutectic-formation temperature, 577°C) from the front surface. Such low-temperature diffusion has been shown to yield preferential aluminum spikes down dislocations [66].

To assess the grain-boundary passivation, we use the electron-beam-induced-current (EBIC) technique. A qualitative analysis is done

initially to detect grain-boundary passivation. Quantitative estimates of grain-boundary parameters, e.g., $S_{n(eff)}^{GB}$, based on EBIC data are derived using the computer-aided numerical simulation, details of which were disclosed in Chapter 3, of the minority-carrier transport underlying the EBIC response of a pn junction in the vicinity of a grain boundary. Current-voltage characteristics and reverse-bias capacitance measurements, which yield the base doping density of the cell, are used to determine the minority-carrier diffusion length in the base, which reflects the benefit produced by the Al-BSF process.

Our experimental results show that the conventional Al-BSF process results in longer diffusion lengths because of (bulk-to-surface) gettering of intragrain impurities, irrespective of indications that the grain boundaries emit impurities during the high-temperature process. Our results also suggest that the minority-carrier lifetime is longer when measured using light-bias than when measured in the dark. This suggestion is consistent with the theory [67] that defect clusters in polysilicon are effectively negated by high carrier-injection levels. No grain-boundary passivation near the front junction is apparent after the BSF process. However we find significant passivation near the front junction resulting from low-temperature aluminum diffusion from the front surface, but no observable gettering. Consequently, it is possible that aluminum diffusion, when optimally done, could substantially increase the efficiencies of both bulk and thin-film polysilicon solar cells.

4.2 Cell Fabrication

The cells used in this study were fabricated on p-type Wacker (cast) polysilicon substrates. After standard cleaning and chemical polishing of the front surface, the substrate thickness, W_B , is about 350 μm . The doping density, N_{AA} , varies from $5 \times 10^{15} \text{cm}^{-3}$ to $1 \times 10^{16} \text{cm}^{-3}$, as determined by reverse-bias capacitance measurements on the completed cells.

Three different kinds of cells were fabricated for comparison in both the bulk and thin-film polysilicon studies. Active cells were subjected to aluminum diffusion while control cells were not. However, the control cells were subjected to the same thermal stress as were their aluminum-diffused counterparts. Several standard cells, which were neither aluminum-diffused nor subjected to any abnormal thermal stress, were also fabricated.

4.2.1 Bulk Process

For the studies applicable to the development of bulk polysilicon solar cells, we used the conventional Al-BSF process for silicon [64] to fabricate the active cells. About 1.5 μm of aluminum was evaporated onto the back surface of the cell after the front phosphorous (n^+) diffusion. The aluminum was then diffused into the active cell during the alloying process at 800°C for 1 hour in forming gas. The control cell underwent an identical heat treatment but without aluminum. Both large-area (0.4 - 0.45 cm^2) and small-area (30-mil-diameter) cells were fabricated.

Fabricating small-area cells enables control of the grain-boundary density in each cell. The surface and edge leakage currents, which are

predominant in large-area cells, can be effectively controlled by means of an MOS guard-ring overlapping the edge of the emitter in the small-area cells [16]. In addition, by comparing the diffusion lengths, determined from the current-voltage characteristics, of the large-area (measured under light) and the small-area (measured in dark) cells, we can deduce the effect of the light-bias on minority-carrier lifetime.

The n^+p junction in the large-area cells was formed by diffusing in phosphorous at 875°C for 30 minutes using $POCl_3$ as the source. The resulting junction depth is about 0.4 μm . Subsequent to the aluminum diffusion, which followed the phosphorous (n^+) diffusion, about 0.6 μm of aluminum was evaporated onto the back surface to serve as a contact. The control and the standard cells were then sintered at 450°C for 15 minutes in forming gas. Following a mesa etch that isolated the cells, the front contact was formed by evaporating a 300-Å-thick aluminum "dot". Details of these processing steps as well as those of the small-area and the thin-film cells are given in Appendix D.

The junction in the small-area cells was formed by a phosphorous predeposition at 950°C for 40 minutes using $POCl_3$ as the source followed by a drive-in diffusion at 1000°C for 27 minutes. This resulted in a junction depth of approximately 0.7 μm . Aluminum was then diffused into the active cells from the back surface. The front- and back-contact aluminum evaporations, 5000-Å and 6000-Å-thick respectively, were performed subsequently. As in the case of the large-area cells, the control and the standard cells were sintered at 450°C for 15 minutes after the back-contact evaporation.

In order to suppress surface and edge leakage currents in the small-area cells, a silicon-dioxide layer (~ 1700-Å-thick) was thermally

grown on the top surface during the drive-in step, and a metal gate was deposited overlapping the edge of the diffused region [16]. A negative gate bias (-20V to ensure surface accumulation in the base) was used while the current-voltage characteristic of the cell was being measured.

4.2.2 Thin-Film Process

For the studies applicable to the development of thin-film polysilicon solar cells, the n^+p junction was formed by diffusing phosphorus at 875°C for 30 minutes using $POCl_3$ as the source. The resulting junction depth is approximately 0.4 μm . A mesa etch was used to isolate the cells. The active and control cells were fabricated on sequential wafers from the Wacker ingot.

We use bulk (large-grain) polysilicon to imply the effects of aluminum diffusion in thin-film (small-grain) cells. This material facilitates electrical isolation of a grain boundary (using EBIC) and enables direct quantitative assessment of the passivation yielded by the aluminum diffusion. We anticipate that the low-temperature diffusion will similarly passivate grain boundaries in thin-film polysilicon. However because the grain boundaries may differ significantly from those in Wacker polysilicon, the extent of the passivation might be different.

We diffused aluminum into the active cells from the front surface at temperatures below the Si-Al eutectic temperature (577°C) to avoid irreparable damage to the junction region. IC-grade aluminum, 1.5- μm -thick, was evaporated onto the front surface before the phosphorous (n^+) diffusion. The aluminum diffusion was then done at 450°C for 3-6 hours in forming gas. Following the removal of excess aluminum, a thin layer of silicon was etched off to avoid shunting of the n^+p junction that is

subsequently formed. The control cells, sequential to the active cells, were also etched in addition to undergoing an identical heat treatment. After the subsequent phosphorous (n^+) diffusion, about 6000 Å of aluminum was evaporated onto the lapped back of the cell to serve as the back contact. The front contact was formed by evaporating a 300-Å-thick aluminum "dot" after the isolating mesa etch.

The standard cells did not undergo any thermal treatment except for the phosphorous (n^+) diffusion and a sinter for 15 minutes at 450°C following the back-contact evaporation.

4.3. Results

4.3.1 Bulk Process

Significant effects of the Al-BSF process are revealed in Tables 4.1 and 4.2, where we give representative values of the electron diffusion lengths L_n (averaged over each cell) in, respectively, the small-area and the large-area active, control, and standard cells. The values of L_n were derived from the quasi-neutral-base recombination current, which was experimentally determined by measuring the dark current-voltage characteristics [68]. We have assumed that the emitter recombination current in both the large- and small-area cells is negligible. The large values of the base recombination current determined from the current-voltage characteristics justify this assumption [68].

The forward current-voltage characteristics of the small-area cells were obtained by measuring the dark current, I_D , through the cell for different values of the forward bias, V_D , across the cell. This measurement as well as the extrapolation of the I_D - V_D characteristics to

Table 4.1 Measured electron diffusion lengths in bulk-cell-related small-area active, control, and standard n^+p cells.

Device	N_{AA} (cm^{-3})	L_n (μm)
STANDARD	6×10^{15}	74
	6×10^{15}	33
	7×10^{15}	27
	7×10^{15}	55
	7×10^{15}	49
	7×10^{15}	47
	7×10^{15}	57
	7×10^{15}	74
ACTIVE	7×10^{15}	63
	8×10^{15}	168
	7×10^{15}	276
	9×10^{15}	173
	9×10^{15}	92
	7×10^{15}	146
	1×10^{16}	92
CONTROL	6×10^{15}	244
	9×10^{15}	20
	1×10^{16}	20
	1×10^{16}	41
	8×10^{15}	14
	7×10^{15}	34
	9×10^{15}	24

Table 4.2 Measured electron diffusion lengths in large-area active, control, and standard n^+p cells. Each row refers to cells fabricated on sequential wafers.

DEVICE	N_{AA} (cm^{-3})	L_n (μm)
STANDARD	5×10^{15}	91
	5×10^{15}	96
ACTIVE	5×10^{15}	160
	5×10^{15}	130
	4×10^{15}	122
CONTROL	5×10^{15}	34
	6×10^{15}	57

obtain the base recombination current [68] was achieved using an HP 9845A desktop computer. The cells were maintained at a constant temperature, $T = 25^\circ\text{C}$, during the measurement by placing them in a Stanam oven. In Fig. 4.1 a typical I_D-V_D characteristic obtained on a small-area active cell is shown.

The base recombination current of the large-area cells was experimentally determined by measuring the short-circuit current, I_{SC} , versus the open-circuit voltage, V_{OC} , characteristic resulting from different illumination levels [68]. The reason for using the $I_{SC}-V_{OC}$ characteristic to determine the base recombination current is that the series resistance associated with the large-area cells does not influence the V_{OC} measurement and can be rendered insignificant in the I_{SC} measurement by applying an appropriate reverse bias across the cells. In this measurement the cells were maintained at $T=25^\circ\text{C}$ by placing them on a Temptronic thermal chuck.

To determine N_{AA} , the capacitance C of the completed cell was measured for different values of the reverse bias V_R . Assuming a one-sided (asymmetrical) junction, we derived the base doping density N_{AA} from the slope of the $1/C^2$ versus V_R plots [69]. These measurements indicated slight variations of N_{AA} among the cells, given in Tables 4.1 and 4.2, that were accounted for in the determinations of L_n .

We see in Table 4.1 that the small-area active cells, which are actually n^+pp^+ structures, have longer diffusion lengths than do both the control and standard cells. On the average, L_n in the active cells is about a factor of three longer than in the standard cells. The average L_n in the control cells is about a factor of six shorter than in the active cells. These results suggest that the Al-BSF process getters

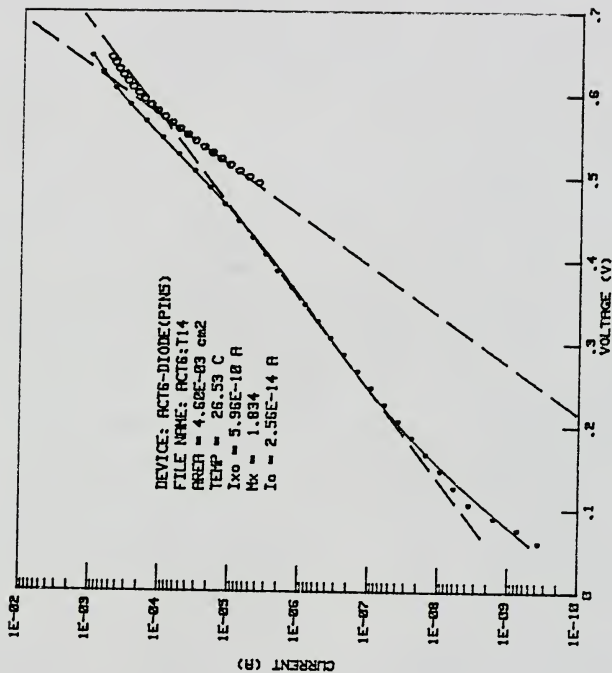


Fig. 4.1 A typical I_D - V_D characteristic obtained from a small-area active cell.

intragrain impurities, reducing the defect density by more than an order-of-magnitude. We discuss this and other possible explanations for the results later.

Measurements of large-area cells, the results of which are given in Table 4.2, also indicate that the conventional Al-BSF process is beneficial. However, the increase in L_n in the large-area cells is seemingly smaller than that in the small-area cells indicated in Table 4.1. Typically L_n is about 50% longer in the active cells than in the standard cells. The discrepancy is possibly due to the fact that large-area cells were measured under light-bias, i.e., the base recombination current was extracted from $I_{SC}-V_{OC}$ measurements, whereas the small-area cells were measured in the dark, i.e., the dark I-V characteristic was used. We discuss this discrepancy later in conjunction with the theory [67] that light-bias effectively negates defect clusters in polysilicon and increases the actual minority-carrier diffusion length.

We also observe in Table 4.1 that the average L_n in the control cells is about 50% shorter than in the standard cells. Since the front and back surfaces of the control cell were masked by an oxide (1700Å) during the 800°C heat treatment, the shorter L_n in the control cells could be due to the emission of impurities from the grain boundaries into the intragranular regions. Such emission, which has been suggested [70], would also occur in the active cells, but apparently the emitted impurities as well as the intragrain defects are gettered to the Si-Al interface.

With regard to grain-boundary passivation resulting from the Al-BSF process, qualitative results from EBIC measurements performed on large-

area cells show no significant reduction of $S_{n(\text{eff})}^{\text{GB}}$. This conclusion is based on a comparison of the percentages of background EBIC current lost at the grain boundary, averaged over ten randomly selected grain boundaries in the active and in the control cells. This result is not unexpected since we are using thick wafers ($W_B = 350 \mu\text{m}$), and it is unlikely that the aluminum could diffuse sufficiently up grain boundaries to significantly passivate them in the vicinity of the front n^+p junction. Furthermore the formation of the Al-Si alloy tends to restrict the amount of aluminum entering the silicon [63]. Hence we conclude that, for bulk polysilicon, aluminum produces no significant grain-boundary passivation when diffused from the back at a high temperature. However it does seem to getter intragrain impurities, thereby increasing L_n . Hence an optimal Al-BSF process might substantially increase bulk polysilicon solar cell efficiencies, perhaps by producing an effective BSF [40].

4.3.2 Thin-Film Process

Since the aluminum diffusion from the front is done at a low temperature prior to the phosphorus (n^+) diffusion, we observe no gettering attributable to it. This could possibly be because most of the impurities are immobile at temperatures around 450°C . However, significant grain-boundary passivation is achieved via this process as inferred from EBIC measurements. These measurements were made on a scanning electron microscope using a beam energy of 35 KeV, which yields a maximum electron penetration depth of about $8 \mu\text{m}$ [21]. Hence the measurements reflect recombination properties of the grain boundaries within about $20 \mu\text{m}$ from the front surface.

In the EBIC images of the top surface, we have observed random clustering of colored dislocations in some grains. We attribute this to preferential aluminum diffusion down dislocations that might possibly be aluminum-induced. The junction, however, is not shorted because it is formed after the low-temperature aluminum diffusion.

To illustrate the grain-boundary passivation effected by aluminum diffusion, we compare, in Fig. 4.2, the percentages of background EBIC lost at the grain boundaries in active and control cells (fabricated on sequential wafers) and in the standard cell. The percentage of EBIC lost at a grain boundary is experimentally determined as follows.

The maximum EBIC, I_{EBIC}^{MAX} , at two points far away from the grain boundary and on either side of it is measured directly. Note that the points should be chosen far enough away from the grain boundary so that the grain-boundary recombination does not limit I_{EBIC}^{MAX} . The EBIC, I_{EBIC} , when the beam is positioned at the center of the grain boundary is also measured. The percentage current lost at the grain boundary is the ratio of the current lost at the grain boundary (given by the difference between the average of the maximum EBICs and the EBIC measured at the grain boundary) and the average of the maximum EBICs.

In Fig. 4.2 we see a clear indication that the aluminum diffusion reduces the current loss at the grain boundaries, which implies that it decreases $S_{n(eff)}^{GB}$ near the n^+p junction. Furthermore it seems in some cases to reduce the scatter in the recombination properties of the grain boundaries. Additional support for these qualitative conclusions is provided in Table 4.3 where we present similar results of EBIC measurements performed on active, control, and standard cells fabricated on nonsequential wafers. We emphasize that these qualitative EBIC

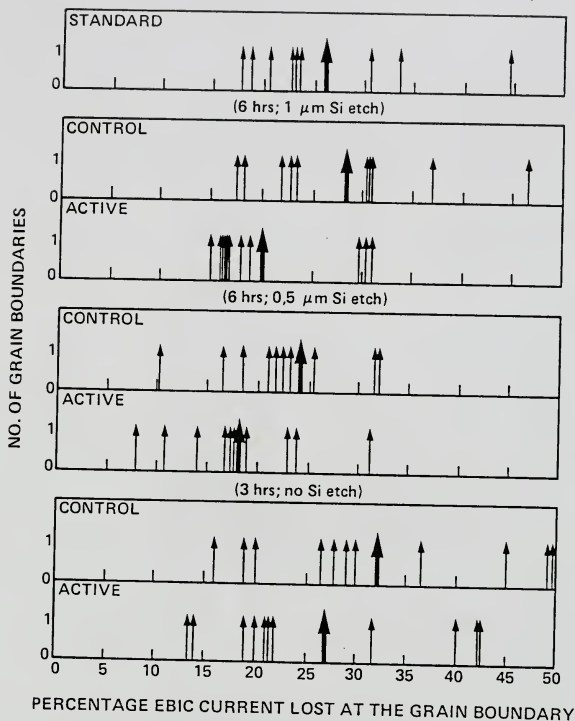


Fig. 4.2 Statistical distribution of the percentage background EBIC lost at the grain boundaries in the active, control, and standard cells (beam energy=35 keV). Each box refers to cells from sequential wafers. Thick arrows indicate the average percentage EBIC lost at the grain boundaries in each cell. The aluminum diffusion (annealing) time and subsequent silicon-etch are given for active (and control) cells.

results merely indicate a trend statistically. The actual decrease in $S_{n(\text{eff})}^{\text{GB}}$ produced and its significance with regard to an actual thin-film cell performance are now considered.

In order to interpret the EBIC measurements quantitatively and evaluate $S_{n(\text{eff})}^{\text{GB}}$ at passivated and unpassivated grain boundaries, we use the solution to the minority-carrier (electron) transport problem in the p-type base outlined in Chapter 3. We will use the results of the numerical solution for the simple case of a circular generation source, the utility of which was discussed, to demonstrate the efficacy of aluminum passivation.

The EBIC response as a function of the distance of the electron beam from the grain boundary is measured experimentally using the setup shown in Fig. 4.3a. The electron beam traverses the grain boundary at a known speed. The Keithley 427 amplifier converts the current to a voltage which is recorded on the x-y plotter. A typical plot obtained using this setup is shown in Fig. 4.3b. Note that it is important to calibrate the sweep-rate of the x-y plotter and the scanning-rate of the electron beam precisely in order to relate the x-axis of the plot in Fig. 4.3b to actual distances in the sample.

The theoretically calculated values of EBIC current as a function of the beam position are plotted in Fig. 4.4 for different values of $S_{n(\text{eff})}^{\text{GB}}$ and for the case of a circular (spherical in three dimensions) generation source. The value of L_n assumed corresponds to that of an active cell. We have assumed that $S_{n(\text{eff})}^{\text{GB}}$ is constant, i.e., independent of the excitation at the grain boundary, which is not valid in general as shown in Chapter 2. Superimposed on the theoretical plots in Fig. 4.4 are the measured EBIC responses obtained on two typical

Table 4.3 Measured EBIC losses at grain boundaries in thin-film-cell-related active, control, and standard n^+p cells fabricated on non-sequential wafers. The aluminum diffusion (annealing) time and subsequent silicon etch are given for the active (and control) cells.

Cell	EBIC Current Loss at Grain Boundary (%)
ACTIVE (6 hr; 2 μm)	23
ACTIVE (6 hr; 1 μm)	20
ACTIVE (3hr; 0.5 μm)	21
CONTROL (6 hr; 2 μm)	28
CONTROL (6 hr; 1 μm)	28
CONTROL (3 hr; 0.5 μm)	25
STANDARD	29
STANDARD	26

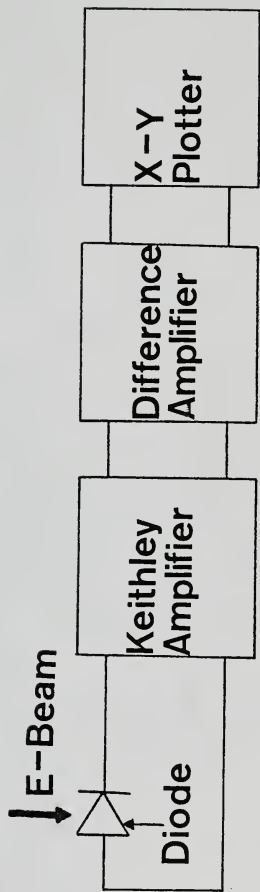


Fig. 4.3a Experimental setup used to obtain the EBIC response.

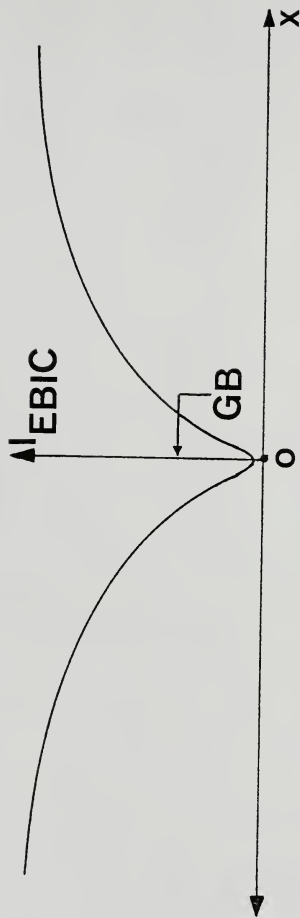


Fig. 4.3b A typical EBIC response obtained using the setup in Fig. 4.3a.

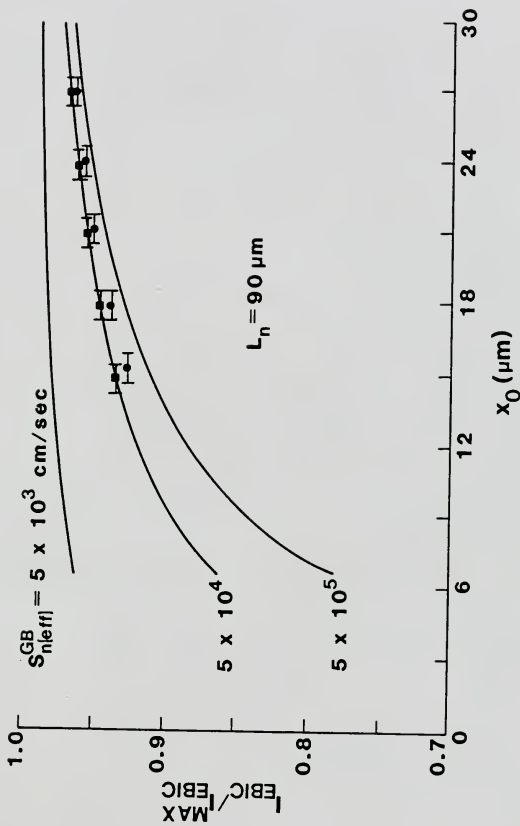


Fig. 4.4 Calculated and measured EBIC (normalized) from an active cell (beam energy=35 keV) as a function of beam position. The experimental points (● and ■) correspond to two different grain boundaries.

grain boundaries in an active cell. By comparing the theoretical and experimental responses, we infer that $S_{n(\text{eff})}^{\text{GB}} = 5 \times 10^4$ cm/sec at the passivated grain boundaries near the n^+p junction. This value is more than an order-of-magnitude lower than the value obtained for the same two grain boundaries (in a sequential control cell) without passivation, which follows from Fig. 4.5. In Fig. 4.5 calculated and measured EBIC responses from the control cell are plotted. These plots imply $S_{n(\text{eff})}^{\text{GB}} > 10^6$ cm/sec, near the kinetic limit velocity S_{KL} [31], at typical unpassivated grain boundaries. Similar analyses reveal that $S_{n(\text{eff})}^{\text{GB}}$ at a typical grain boundary in a standard cell is comparable to that in a control cell.

We now support the assumptions of constant $S_{n(\text{eff})}^{\text{GB}}$ and a spherical generation source, in conjunction with the results in Chapter 3. In Chapter 3 it was shown that the nonlinearity in $S_{n(\text{eff})}^{\text{GB}}$ is not significant until the beam is sufficiently close to the grain boundary. This is particularly true in the vicinity of passivated grain boundaries, where $S_{n(\text{eff})}^{\text{GB}}$ is low. The reason for this is that the minority electron density at the grain boundary is not high enough to significantly change the barrier. Consequently $S_{n(\text{eff})}^{\text{GB}}$ is nearly constant in the EBIC measurements made and analyzed in this chapter. Furthermore we concluded in Chapter 3 that the spherical generation source is a good representation of the actual electron-beam-induced generation provided we interpret data (as we did here) taken about $2z_0$ away from the grain boundary (see Fig. 3.13), where z_0 is the maximum penetration depth of the primary electrons ($z_0 = 8 \mu\text{m}$ at $E_0 = 35$ keV).

In order to estimate the reduction in the grain-boundary trap density $N_{\text{ST}(\text{eff})}^{\text{D}}$ corresponding to the decrease in $S_{n(\text{eff})}^{\text{GB}}$

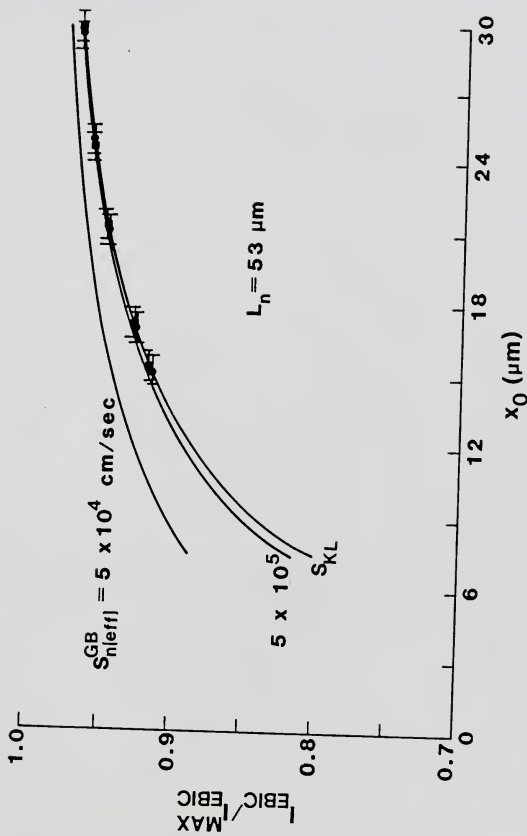


Fig. 4.5 Calculated and measured EBIC (normalized) from a control cell (beam energy=35 keV) as a function of the beam position. The experimental points (● and ■) correspond to two grain boundaries that are sequential to those referred to in Fig. 4.4. The bottom calculated curve corresponds to the kinetic-limit recombination velocity $S_{KL} \approx 5 \times 10^6 \text{ cm/sec}$ [31]

resulting from the aluminum diffusion, we use the analytic model developed in Chapter 2. It was shown that for a monoenergetic density of trap states located at the center of the energy gap, $S_{n(\text{eff})}^{\text{GB}}$ is insensitive to the grain-boundary excitation for sufficiently low $N_{\text{ST}(\text{eff})}^{\text{D}}$ and sufficiently low excitation. For these conditions, $S_{n(\text{eff})}^{\text{GB}} \propto N_{\text{ST}(\text{eff})}^{\text{D}}$. We thus infer that $N_{\text{ST}(\text{eff})}^{\text{D}} \approx 2-5 \times 10^{11} \text{ cm}^{-2}$ at typical unpassivated grain boundaries, and it is more than an order-of-magnitude lower at typical passivated grain boundaries. The low value of $N_{\text{ST}(\text{eff})}^{\text{D}}$ ($\sim 10^{10} \text{ cm}^{-2}$) at the passivated grain boundary reveals that the aluminum diffusion reduces the grain-boundary trap density toward a physical lower limit, and that further reductions in $S_{n(\text{eff})}^{\text{GB}}$, which is defined by the grain-boundary potential barrier, can be achieved only by increasing N_{AA} (see Chapter 2).

4.4 Discussion

In this chapter we have demonstrated experimentally that aluminum diffusion can be beneficial to both bulk and thin-film polysilicon solar cells.

With regard to bulk polysilicon cells, we found that the conventional Al-BSF (800°C) process [64] produced concomitant gettering of prevalent intragrain impurities, in accord with previously reported results [63]. The gettering, which increased the average minority electron lifetime ($\tau_n = L_n^2/D_n$) in p-type Wacker (cast) polysilicon significantly, was detected by dark current-voltage and reverse-bias capacitance measurements of n^+p solar cells. We also found evidence that the grain boundaries emit impurities into the intragranular regions during the high-temperature heat treatment, but that the emitted

impurities as well as the intragrain defects are effectively getterred to the Si-Al interface. EBIC measurements revealed that the Al-BSF did not passivate grain boundaries near the front junction because of the thickness of the bulk polysilicon.

It has been theorized that L_n increases with the illumination level because defect clusters are negated by high carrier-injection levels. Comparison of L_n in standard and control cells measured under light-bias (large-area cells in Table 4.2) and in the dark (small-area cells in Table 4.1) support this theory. For example, the average L_n in the standard cell is about a factor of two higher when measured using light-bias than when measured in the dark. Since the defect densities in the active cells are reduced due to the gettering, no such increase in L_n with illumination is observed (compare results in Table 4.1 with those in Table 4.2).

With regard to thin-film polysilicon cells, we found that a low-temperature (450°C) aluminum diffusion from the front surface of the cell produced significant passivation of grain boundaries. The passivation was experimentally assessed using EBIC measurements which showed a reduction in the current lost at an aluminum-diffused grain boundary in comparison with one without aluminum. Typically, the grain-boundary recombination velocity, which is unaltered by EBIC excitations far away from the grain boundary, is reduced from greater than 10^6 cm/sec to less than 10^5 cm/sec by the aluminum diffusion. These values of $S_{n(eff)}^{GB}$ near the n^+p junction were determined by interpreting measured EBIC responses using a computer-aided numerical simulation of the underlying electron transport in the quasi-neutral base of the n^+p cell developed in Chapter 3. Using the analytic grain-boundary

recombination model developed in Chapter 2, we found that the grain-boundary trap density was also lowered by more than an order-of-magnitude by the aluminum diffusion. The value of $N_{ST(eff)}^D$ at a typical Al-passivated grain boundary is $\sim 10^{10} \text{ cm}^{-2}$, which is probably low enough to enable the virtual suppression of grain-boundary recombination losses in thin-film cells by proper choice of N_{AA} (see Chapter 2). For example, from Fig. 2.9 we infer that if N_{AA} were 10^{17} cm^{-3} , $S_{n(eff)}^{GB}$ would be near 10^3 cm/sec , which would render the grain boundary virtually inactive electrically. We note that the grain-boundary passivation produced by the aluminum diffusion is distinct from any passivation due to the phosphorous diffusion, which would occur in the standard and control cells as well as the active ones, but which is probably negligible [16].

To exemplify the real benefit of the aluminum diffusion to the efficiency of a thin-film polysilicon solar cell, we estimate the increase in V_{OC} that would result from the inferred reduction in $N_{ST(eff)}^D$ noted above. It has been shown [33] that the predominate recombination current component in a thin-film cell may well be that from the portion of the grain boundary within the junction space-charge region, I_{GB}^{SCR} , which is proportional to $N_{ST(eff)}^D$ [8]. Thus in this case, the large reduction in $N_{ST(eff)}^D$ would increase V_{OC} by about $(kT/q)\ln(50) \approx 100 \text{ mV}$, provided I_{GB}^{SCR} were still predominant in the grain-boundary-passivated cell.

In contrast to other grain-boundary passivation techniques [17-19], we expect the Al-diffused grain boundaries to be quite stable. The low-temperature aluminum diffusion was done prior to the high-temperature phosphorous (n^+) diffusion, which therefore stabilizes the redistributed

aluminum. The grain boundaries are effectively passivated even after the phosphorous diffusion, which implies that no significant out-diffusion of aluminum from the grain boundaries occurs, possibly because of a high segregation coefficient for aluminum at the grain boundaries.

We emphasize that the aluminum processes described in Section 4.2 are not necessarily optimal. Additional experiments are needed to determine optimal temperatures and times that maximize the gettering efficacy of aluminum in bulk cells and the grain-boundary passivation in thin-film cells. Furthermore in the thin-film process, the amount of aluminum evaporated onto the front surface prior to the diffusion and the subsequent silicon-etch must be properly specified. The main objective of this research, however, is not to define optimized processes, but to indicate the potential improvements afforded by aluminum diffusion in both bulk and thin-film polysilicon solar cells.

Although we have suggested that gettering is the most likely mechanism that produces the observed increases in the diffusion length, i.e., the decreases in the base recombination current J_{B0} , we cannot rule out the possible presence of the BSF effect [40]. Preferential dissolution of silicon can occur when aluminum is evaporated onto silicon and heated at temperatures greater than 700°C [28]. This dissolution, which occurs most rapidly at dislocations due to weak bonding, can penetrate deeply into the silicon [28]. As a result, a nonuniform and nonplanar BSF is produced, which could cause an apparent increase in the minority-carrier diffusion length as implied by J_{B0} . Hence, although we surmise the Al-BSF getters intragrain impurities, we stress that our results could be due to the formation of a nonuniform BSF.

In the next chapter we examine the mechanisms of gettering and nonuniform BSF due to preferential dissolution of silicon in greater detail in an effort to isolate the actual mechanism that is responsible for the observed improvements in the bulk polysilicon cell performance.

CHAPTER 5 ALUMINUM GETTERING IN (CAST) POLYSILICON

5.1 Introduction

In Chapter 4 we presented experimental evidence for benefits to the performance of polysilicon solar cells afforded by aluminum diffusion. We found that the conventional Al-BSF process [61] resulted in a reduction in the base saturation current density, J_{B0} , which we attributed to gettering of impurities from the base region by the aluminum alloying. Another possible explanation for the reduction in J_{B0} could be the formation of an effective, but nonuniform, nonplanar back-surface field (BSF) [40] due to the preferential dissolution of silicon during the high-temperature process [28]. Although the results in Tables 4.1 and 4.2 imply that the BSF is inconsequential in bulk cells since $L_n < W_B$, we consider it because the preferential dissolution of silicon can cause deep penetrations of aluminum into the base of the cell, resulting in an effective BSF in some portions of the cell, and because the L_n that we measured is an average value over several grains in which the local value may vary significantly.

If the aluminum penetrations are substantially deep ($\sim W_B$), and/or if L_n is sufficiently long ($\sim W_B$), then the BSF effect can be prevalent over a significant area of the cell, and the reduction in J_{B0} observed in Chapter 4 could be due to this nonuniform BSF rather than to gettering. The main objective of this chapter is to experimentally identify the actual mechanism that is responsible for the reduction in J_{B0} .

Most of the previous research regarding the aluminum-silicon system has been focused on low-temperature processing, e.g., sintering, because of its extensive use in the fabrication of silicon integrated circuits. Gettering of impurities by aluminum has been observed at temperatures below the eutectic temperature (577°C) [71, 72]. Thompson and Tu [72] found that annealing a silicon wafer, which has a layer of aluminum on its surface, at 540°C for 100 hours results in the removal of copper and gold from the silicon. As intimated in Chapter 4, aluminum also preferentially diffuses down dislocations (aluminum "spiking") when heated at below-eutectic temperatures, resulting in deep ($> 10 \mu\text{m}$) penetrations into the substrate [66, 73, 74]. If the aluminum "spikes" down dislocations in shallow-junction devices, it can increase leakage currents and could even result in shorted junctions [73].

The gettering as well as the penetrations into the substrate by aluminum occur at above-eutectic temperatures also [28, 63]. However the kinetics of these mechanisms are different at low and high temperatures; solid-phase diffusion occurs at low temperatures, and liquid-phase diffusion occurs at high temperatures. Another distinguishing feature is that the liquid-phase diffusion proceeds at a much faster rate than the solid-phase diffusion [62].

In this chapter we will study the impurity gettering as well as the dissolution of silicon into the aluminum during the high-temperature processing of silicon with a layer of aluminum on its surface. The removal of impurities from the base region of a p-n junction diode, i.e., gettering, results in an increase in the minority-carrier lifetime, and a consequent reduction in J_{B0} . The dissolution of silicon into the aluminum, which occurs preferentially [28], may cause deep

penetrations of aluminum into the silicon resulting in an effective back-surface field. If the BSF effect is significant, then it reduces J_{B0} as does gettering. The formation of an effective BSF hence may be wrongly interpreted as an increase in the minority-carrier diffusion length. A good understanding of the Al-Si system when subjected to above-eutectic temperatures is therefore essential to distinguish between these two mechanisms.

We provide, in this chapter, a qualitative description of the mechanisms of gettering and the formation of a nonuniform BSF due to the dissolution of silicon. In order to identify the mechanism (gettering or nonuniform BSF) that is responsible for the reduction in J_{B0} , we determine the minority electron diffusion length L_n in aluminum-diffused (n^+pp^+) polysilicon cells before and after lapping off the back p^+ junction. The values of L_n are determined from forward current-voltage and reverse-bias capacitance measurements on large-area Wacker (cast) polysilicon cells. We also investigate the benefits of the Al-BSF process in cells made from semiconductor-grade silicon substrates as well as from solar-grade [29] silicon substrates. The motivation for doing this is to determine if the benefits of the Al-BSF process are unique to the (cast) polysilicon.

Our results indicate that the reduction in J_{B0} which results from the conventional Al-BSF process [61] is predominantly due to impurity gettering. The BSF effect due to the penetration of aluminum into the silicon does not significantly influence J_{B0} . No significant increase in L_n was observed in the active (n^+pp^+) cells fabricated on semiconductor-grade and solar-grade silicon, which suggests that the impurity gettering is unique to the (cast) polysilicon. The results

imply that the polysilicon contains unique impurities that limit L_n ; they are not prevalent in semiconductor-grade nor solar-grade silicon. Data obtained from Wacker Siltronic Corporation [75] indicate that the concentration of oxygen in the cast polysilicon is about four orders of magnitude higher than that in semiconductor-grade and solar-grade silicon. The presence of oxygen can cause short minority-carrier lifetimes [76] due to the creation of donor-type impurities during heat treatment. Hence we surmise that aluminum getters oxygen and/or oxygen-related defects during the high-temperature process.

5.2 Description of the Mechanisms

5.2.1 Gettering

Gettering can be defined as the process of removing impurities and defect nuclei from crystals and wafers. The application of suitable thermal, mechanical, or chemical forces to the wafer can cause the transport of metallic impurities and defect nuclei (such as oxygen) from the wafer to an external source such as the wafer surface [60].

The effectiveness of gettering depends upon two criteria: 1) the temperature must be high enough that impurities can diffuse readily through the silicon and 2) the impurities must be captured (soluble) at a noncritical region of the wafer and must not be released back into the wafer on subsequent heat treatments.

Gettering can be achieved by the introduction of stresses on the surface of the wafer followed by heat treatments at elevated temperatures [60]. Metallic impurities such as iron, copper, and gold can be gettered by the predeposition of phosphorous, boron, arsenic, or gallium [60]. As a result of the lattice stress caused by the dopant

diffusion, dislocations are created at the surface of the wafer [60]. Impurities diffuse towards these dislocations, which are created away from the active regions of the device, and are captured by the dislocation sites.

Another model for gettering has been proposed by Goetzberger and Shockley [77]. According to this model, metal atoms diffuse to the surface where they react with the gettering agent by formation of chemical compounds. The gettering of copper by phosphorous has been explained by this model. Copper atoms diffuse from within the wafer to the surface during phosphorous or boron predeposition to form borates or phosphates [77, 78]. It has been shown [79] that metallic impurities can also be gettered by employing inorganic oxides as gettering agents at temperatures between 800°C-1000°C.

It has also been found [80] that copper and gold tend to accumulate in the heavily doped regions of the wafer. This has been attributed to the high solubility and low diffusivity of copper and gold in heavily doped layers. The reason for the increased solubility can be explained by an analogy to chemical reactions. The defect (solute) density in the doped semiconductor (solvent) increases when the doping density (solvent) is increased in accordance with the laws of mass action [80, 81]. For example, when copper and gold exhibit acceptor behavior in silicon, an n^+ (phosphorous) diffusion has been found to getter them out of the low-doped regions of the wafer to the heavily doped region [80].

5.2.2 Formation of a nonuniform back-surface field

In our experiments described in Chapter 4, pure aluminum was deposited onto silicon and annealed at 800°C in a forming-gas atmosphere. During this process no melting occurs until the temperature of the Al-Si system rises well above the eutectic temperature (577°C), or very close to the aluminum melting temperature (660°C) [28]. The reason for this is that there is no material of eutectic composition present initially. Once the aluminum is melted, an Al-Si liquid-phase of temperature-dependent composition is formed comprising all the deposited aluminum and the required silicon, which comes from the substrate. As the sample is slowly pulled out from the furnace, the composition of silicon in the liquid-phase must decrease as implied by the phase diagram shown in Fig. 5.1. The excess silicon segregates at the silicon-liquid interface and forms a regrowth layer doped with aluminum (p^+ layer) [28]. The regrowth layer, the thickness of which is directly proportional to the weight of the deposited aluminum [64], forms the necessary p^+p (high-low) junction to create a back-surface field. The segregation of the silicon stops when the liquid is cooled down to the eutectic point, and the liquid solidifies [28]. The final structure is illustrated in Fig. 5.2.

During the Al-Si alloying process, the main factor that controls the points at which the dissolution of silicon begins is the energy required to remove the silicon atoms from the lattice. Because of the low strain energy associated with a dislocation, removal of the silicon atoms from the lattice requires the least amount of energy at positions where dislocations emerge at the surface. In other words the most loosely bonded atoms (at dislocations) are removed first [28]. Since

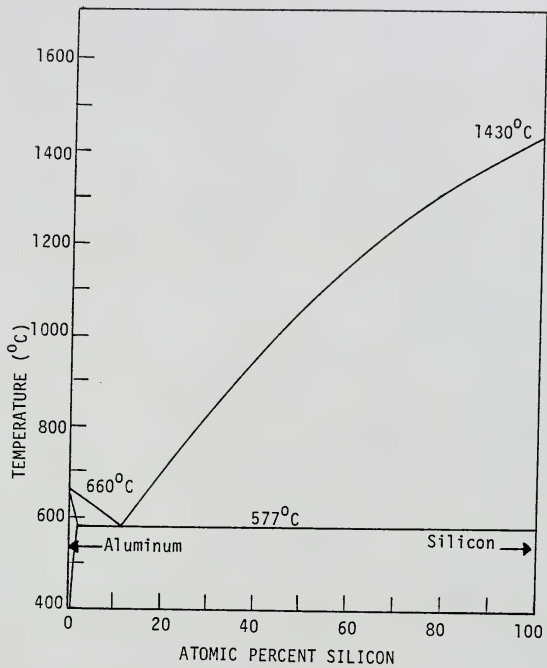


Fig. 5.1 Phase diagram of the aluminum-silicon system.

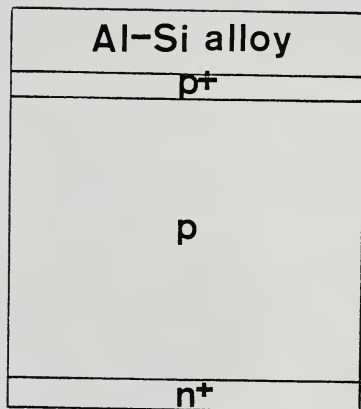


Fig. 5.2 Structure of an aluminum-alloyed (n^+pp^+) cell.

the grain boundaries are dislocations, the removal of the atoms at the grain boundaries takes place readily, resulting in aluminum "spikes" along the grain boundaries as reflected in Chapter 4. The silicon atoms are taken into the molten aluminum until the proportion of the silicon reaches about 25% (at 800°C) as inferred from Fig. 5.1. Until this melt composition is achieved, the system is in nonequilibrium, and hence the silicon atoms are removed from the lattice at a rapid pace. Once the melt composition corresponding to the temperature is reached, further dissolution takes place in near equilibrium conditions, and silicon is dissolved more or less uniformly from the surface [28]. The points of initial attack (i.e., the points at which the grain boundaries emerge at the surface) due to the preferential dissolution of silicon are where the deep penetrations of aluminum into the silicon occur.

On cooling the wafer, the excess silicon in the Al-Si alloy, which penetrates to different depths at different points in the silicon substrate, recrystallizes. This recrystallized silicon, doped with aluminum, creates a nonplanar back-surface-field layer. The reason for the nonuniformity is the varying depths of penetration (penetration depths up to 75 μm have been measured [28]) of aluminum into the silicon. The BSF effect, if dominant, can reduce J_{B0} [40], thus resulting in an apparent increase in the minority-carrier diffusion length.

5.3 Results

We focus our attention on two main topics in this section:

- 1) Identification of the actual mechanism, gettering or nonuniform BSF, that is responsible for the reduction in J_{B0} of (Wacker) polysilicon

cells fabricated using the conventional Al-BSF process. This identification is achieved by comparing L_n in active (n^+pp^+) cells with and without the back p^+p high-low junction. 2) Investigation of the beneficial effects of the Al-BSF process in semiconductor-grade and solar-grade [29] silicon cells. The purpose of this study is to ascertain whether or not the benefits that result from the Al-BSF process are unique to the (Wacker) polysilicon by comparing L_n in the active (n^+pp^+) cells and in the standard cells fabricated on semiconductor-grade and solar-grade silicon substrates.

5.3.1 Polysilicon cells

In order to determine if the reductions in J_{B0} due to the conventional Al-BSF process [61] were due to gettering or due to a back-surface field, we compare, in Table 5.1, the values of L_n in large-area Wacker (cast) polysilicon cells. The cells were fabricated using the bulk process outlined in Chapter 4, wherein we also described the technique to determine L_n from the short-circuit current (I_{SC}) versus open-circuit voltage (V_{OC}) characteristic. The values of L_n in the active (n^+pp^+) cells are about 50% higher than those in the standard cells, which is consistent with our earlier results. However our purpose here is not to compare the active and standard cells, but to compare L_n in aluminum-diffused cells with and without the back-surface field. If the decrease in J_{B0} is caused by a back-surface field, and consequently, the inferred increase in L_n is only an apparent one, then removing the p^+p (high-low) junction from the aluminum-diffused cells would increase J_{B0} .

Table 5.1 Measured electron diffusion lengths in active (with and without the p^+ layer) and standard n^+p polysilicon cells.

Device	N_{AA} (cm^{-3})	L_n (μm)
ACTIVE (n^+pp^+)	6×10^{15}	190
	5×10^{15}	150
	5×10^{15}	165
ACTIVE (Back-lapped)	6×10^{15}	160
	5×10^{15}	165
STANDARD	6×10^{15}	105
	5×10^{15}	100

The removal of the p^+p junction was achieved by lapping off 25-50 μm of material from the back surface of the active (n^+pp^+) cells, which were fabricated using the conventional Al-BSF process. Aluminum back and front contacts were then evaporated as described in Chapter 4. The cells were not sintered after the back-contact evaporation.

The values of J_{B0} in the back-lapped samples were measured to be about the same as in the active (n^+pp^+) cells. This suggests that the back-surface field had no influence in the reductions on J_{B0} observed in the aluminum-diffused polysilicon cells. We can thus conclude that the conventional Al-BSF process getters intragrain impurities in Wacker polysilicon.

To further consolidate the fact that the BSF effect due to the dissolution of silicon is not important, we measured the penetration depths of aluminum into the polysilicon in the active (n^+pp^+) structures. In order to measure these depths, we etched the Al-Si alloy layer from the back of the active cells by immersing them in HCl for 2-3 days. We observed that the back surface of the n^+pp^+ cell, after removal of the Al-Si alloy layer, was pitted due to preferential dissolution of silicon. Using an optical microscope, we estimated the depths of the pits to be 10-20 μm on the average, which is much less than the substrate thickness ($W_B \approx 350 \mu\text{m}$). To produce an effective BSF, the dissolution must penetrate to near the front junction [40], which requires the pits to be at least 200- μm deep. Since this is definitely not what is observed experimentally, we conclude that the nonuniform, nonplanar BSF due to the preferential dissolution of silicon is ineffective.

5.3.2 Semiconductor-grade and solar-grade silicon cells

Having established that the conventional Al-BSF process getters intragrain impurities in Wacker (cast) polysilicon, we next examine its gettering efficacy in semiconductor-grade as well as solar-grade [29] silicon cells. The solar-grade silicon is devoid of grain boundaries but has twin planes in it. The motivation for fabricating semiconductor-grade and solar-grade silicon cells is to determine if the gettering is unique to the Wacker (cast) polysilicon.

We fabricated large-area active and standard cells on semiconductor-grade and solar-grade silicon substrates using the bulk process described in Chapter 4. The semiconductor-grade silicon (Czochralski) wafers were obtained from Wacker, and their base doping densities were determined to be about $3 \times 10^{15} \text{ cm}^{-3}$ from reverse-bias capacitance measurements. The base doping densities of the solar-grade silicon wafers were determined to be about $8 \times 10^{15} \text{ cm}^{-3}$.

The base diffusion lengths, determined from I_{SC} - V_{OC} characteristics (see Chapter 4), for the active and standard cells fabricated on semiconductor-grade silicon substrates are given in Table 5.2. We find no significant change in L_n due to the Al-BSF process. In Table 5.3 we give values of L_n obtained on solar-grade silicon cells. We find from Table 5.3 that, as in the case of silicon cells, the active (n^+pp^+) cells have about the same L_n as do the standard cells. Since L_n in the active cells fabricated in semiconductor-grade or solar-grade silicon is not longer, we conclude that the conventional Al-BSF process does not getter impurities in these materials, as it does in the polysilicon. We cannot say whether or not the grain boundaries having diffused aluminum facilitate the gettering process, or that the impurities in Wacker

Table 5.2 Measured electron diffusion lengths in active (with and without the p^+ layers) and standard n^+p silicon cells.

DEVICE	N_{AA} (cm^{-3})	L_n (μm)
ACTIVE (n^+p^+)	3×10^{15}	200
	3×10^{15}	265
	3×10^{15}	280
ACTIVE (Back-lapped)	3×10^{15}	200
	3×10^{15}	280
STANDARD	3×10^{15}	250
	3×10^{15}	280
	3×10^{15}	300

Table 5.3 Measured electron diffusion lengths in active, control, and standard n^+p solar-grade silicon cells.

DEVICE	N_{AA} (cm^{-3})	L_n (μm)
ACTIVE (n^+pp^+)	8×10^{15}	175
	8×10^{15}	145
CONTROL	8×10^{15}	180
	9×10^{15}	200
STANDARD	8×10^{15}	210
	7×10^{15}	150

(cast) polysilicon are unique, but one or both of these is possible. Most probably, because L_n is considerably shorter in the polysilicon, there are prevalent impurities in it, which can be gettered by the Al-BSF process and which are not prevalent in the other materials.

To identify the impurities present in Wacker (cast) polysilicon and to determine if they are unique, we refer to data provided by Wacker Siltronic Corporation [75]. We compare the types and densities of impurities prevalent in Wacker semiconductor-grade silicon [75] and (cast) polysilicon used in our experiments. The impurities prevalent in Wacker polysilicon are oxygen, carbon, titanium, cobalt, antimony, and iron [75]. The concentration of oxygen in Wacker polysilicon is $\sim 5 \times 10^{17} \text{ cm}^{-3}$, which is at least four orders of magnitude greater than that in Wacker semiconductor-grade silicon [75]. Because of this large difference between the oxygen content in the polysilicon and that in the semiconductor-grade silicon, it is likely that the gettering observed in the polysilicon is due to the removal of the oxygen atoms from the bulk.

When oxygen-rich samples are annealed at temperatures greater than 400°C , the oxygen atoms are thermally activated into donor-type impurities [82, 83]. These donors cause a reduction in the minority-carrier lifetime [76]. One possible reason for this reduction could be that the oxygen donors form effective recombination centers, i.e., produce deep-level traps in the energy gap. A second reason could be that mobile impurities, which are gettered by oxygen, are released to form effective recombination centers when oxygen is activated into the donor state [76].

We thus surmise that aluminum getters oxygen and/or the mobile impurities possibly released by the oxygen during the donor-activation process. Because the oxygen content in the polysilicon is much higher than that in semiconductor-grade silicon, this conjecture is consistent with our results.

We note that although we have suggested that aluminum getters oxygen in polysilicon, it is not unlikely that other impurities present in Wacker polysilicon such as iron, titanium, cobalt, and antimony, which form effective recombination centers in silicon [84], are gettered by aluminum. Furthermore Wacker polysilicon contains a higher density ($\sim 10^{18} \text{ cm}^{-3}$) of carbon, which is at least two orders of magnitude higher than that in semiconductor-grade silicon. However the recombination effects due to carbon are not well understood [60] and hence are not discussed here.

Not much information is available about the type of impurities and their densities prevalent in solar-grade silicon. However, from Table 5.3, we observe that the measured diffusion length in standard cells fabricated on solar-grade silicon is higher than that in polysilicon (standard) cells (see Table 5.1), and, in fact, is comparable to that measured in semiconductor-grade silicon (standard) cells. This suggests that the impurity (presumably oxygen) content in solar-grade silicon is lower than that in polysilicon, which provides a possible explanation as to why aluminum gettering is not observed in solar-grade silicon.

In Table 5.3, note that the control cells made on solar-grade silicon show no significant reduction in L_n from that of the standard cells. Contrarily the control cells made on polysilicon substrates had

a lower L_n than that in the standard cells (see Tables 4.1 and 4.2), which we attributed to emission of impurities by the grain boundaries into the grains. Since the solar-grade silicon [29] has only twin planes and no grain boundaries in it, there is no emission of impurities into the bulk region, and consequently there is no reduction in L_n . This provides additional support for our conclusion that grain boundaries emit impurities, which has also been observed elsewhere [70].

5.4 Discussion

In this chapter we studied the Al-Si system when it is subjected to elevated temperatures. We established, by means of I_{SC} - V_{OC} measurements on solar cells, that the Al-BSF process getters intragrain impurities in Wacker (cast) polysilicon. Furthermore, we found that the gettering is apparent only in polysilicon and not in semiconductor-grade or in solar-grade [29] silicon cells. We then surmised that aluminum getters oxygen and/or oxygen-related impurities, which are present in higher densities in the polysilicon than in semiconductor and solar-grade silicon [75].

We provided a qualitative description of the mechanisms of gettering and the formation of a nonuniform BSF due to preferential dissolution of silicon that could possibly produce the observed reduction in J_{B0} in aluminum-diffused polysilicon cells. Several models [60, 77, 78, 80] have been proposed in the literature for gettering. The strain-field model [60, 78] postulates that during predeposition of dopants, dislocations are introduced at the surface as a result of lattice stress. At high temperatures, the impurities are mobile and hence they diffuse towards the dislocations and are captured by them. The compound-formation model [67] suggests that metallic impurities,

such as copper, form a compound with the gettering agent (a phosphate is formed in the case of phosphorous gettering). The impurities readily diffuse towards the surface since the concentration of impurities there is very low. The defect solubility model [80] postulates that particular impurities readily dissolve in heavily-doped layers due to their high solubility. For example, copper and gold, if present as acceptor-type impurities in silicon, tend to accumulate in the n^+ region adjacent to the surface of the wafer [80], and are thus gettered out of the low-doped regions of the wafer.

The nonuniform, nonplanar BSF is formed as a result of preferential dissolution of silicon during the aluminum-diffusion process. When aluminum is alloyed with silicon, the necessary silicon is obtained from the substrate preferentially from the most weakly bonded sites (dislocations) [28]. Consequently aluminum penetrates down the grain boundaries, since grain boundaries are dislocations, to varying depths in the silicon resulting in a nonuniform BSF layer. The effect of the nonuniform BSF layer, if predominant, is to cause a reduction in J_{BO} , which implies an apparent increase in L_n .

We measured $I_{SC}-V_{OC}$ and reverse-bias $C(V)$ characteristics of active (Al-BSF) n^+pp^+ polysilicon cells, from which we determined the electron diffusion length in the base. In order to prove that the observed increase in L_n was real and not merely apparent, which would be the case if the BSF was the dominant mechanism, we lapped the back p^+p junction in the active cells and determined L_n . We found that values of L_n in the back-lapped cells were about the same as those in the active (n^+pp^+) cells, which proves that the Al-BSF process getters intragrain impurities in Wacker (cast) polysilicon.

It should be pointed out that the reduction in J_{B0} in active (Al-BSF) cells is also commensurate with a possible reduction in the minority-electron mobility within a diffusion length of the junction [85]. The reduced mobility could be caused by the lattice strain produced during the aluminum-diffusion process. If the reduction in J_{B0} were due to a lowering of the electron mobility, then lapping off the back p^+p (high-low) junction should have increased J_{B0} . The reason for this is that lapping off the p^+p junction decreases the lattice strain, and consequently the mobility increases. However, we experimentally observed no change in J_{B0} when the p^+p junction was lapped off from the active (Al-BSF) cells. This suggests that it is unlikely that mobility reduction is an important mechanism that reduces J_{B0} in the active (Al-BSF) cells.

Measurements on semiconductor-grade and solar-grade [29] silicon cells revealed no significant increase in L_n due to the conventional Al-BSF process [61]. From this we concluded that the benefits due to the Al-BSF process were unique to the polysilicon. A possible reason for this is that Wacker (cast) polysilicon contains much higher densities of oxygen compared to semiconductor and solar-grade silicon [75]. The presence of high densities of oxygen can reduce minority-carrier lifetime in polysilicon as a result of the formation of thermal donors during heat treatment [82, 83]. The reduction in the minority-carrier lifetime could be due to the formation of deep-level traps, which act as effective recombination centers, created by the thermal donors, or due to the release of mobile impurities that become effective recombination centers when oxygen is activated into the donor state. The observed increase of L_n in the polysilicon could then possibly be

due to the removal of the oxygen atoms or the released impurities by the aluminum.

We also found that L_n in the control cells processed on solar-grade silicon, which has no grain boundaries in it, were about the same as in the standard cells (see Table 5.3). The control cells processed on Wacker polysilicon showed a decrease of the diffusion length (see Tables 4.1 and 4.2), from which we concluded that grain boundaries in polysilicon emit impurities at high temperatures, which is consistent with [70] and with our solar-grade-silicon experiments.

Finally we point out that the characterization of the Al-Si system presented in this chapter is not conclusive. Further experiments, possibly using an ion probe or Auger electron spectroscopy (AES) [86], are recommended to enable better characterization of the Al-Si system. Comparison of the type and relative concentrations of impurities prevalent in the bulk of the polysilicon and at the Al-Si interface would serve as an independent method to determine gettering.

CHAPTER 6
SUMMARY, DISCUSSION, AND RECOMMENDATIONS

In this dissertation we have developed an analytic model for minority-carrier transport in polysilicon, and provided experimental corroboration for the model using EBIC measurements. The EBIC measurements were quantified by means of a computer-aided numerical solution of the relevant transport problem. We have also demonstrated the potential of aluminum diffusion to improve the performance of polysilicon solar cells.

The main accomplishments of the research are summarized as follows:

- 1) An expression for the effective recombination velocity as a function of the grain-boundary excitation (excess carrier density) was derived, and the importance of including the nonlinearity in the general solution of the transport problem was discussed.
- 2) An approximate analytic model for the minority electron transport in the base of a n^+p polysilicon diode was developed, and it was shown that the transport is influenced by the grain boundaries only at low and intermediate forward voltages.
- 3) EBIC measurements were used to demonstrate the dependence of the grain-boundary recombination velocity on the excitation as well as to determine the surface-state density at the grain boundary and the diffusion length in the grain.

- 4) The conventional Al-BSF process [61] was shown to getter intragrain impurities (in Wacker polysilicon) as implied by current-voltage measurements on polysilicon cells, producing at least a factor-of-two increase in the bulk diffusion length, vis-a-vis, a factor-of-four increase in minority (electron) lifetime.
- 5) The gettering was found to be peculiar to Wacker (cast) polysilicon cells, which we attributed to the presence of unique impurities in polysilicon that are not present in semiconductor-grade nor in solar-grade [29] silicon cells. The polysilicon contained a much higher density of oxygen than semiconductor-grade silicon, and hence we speculated that aluminum getters oxygen.
- 6) A low-temperature aluminum diffusion process was shown to effectively passivate the grain boundaries, producing more than an order-of-magnitude reduction in the defect density at a typical (Wacker polysilicon) grain boundary.

The grain-boundary analysis in Chapter 2, which is based on an effective monoenergetic density of trap states situated at midgap, predicted that $S_{n(eff)}^{GB}$ is nonlinear. The functional dependencies of $S_{n(eff)}^{GB}$ predicted by the grain-boundary analysis are valid even when the trap level is not at the intrinsic level, but is within about $5kT$ above or below it. For example, the predominant trap level at a grain boundary adjacent to a p-type grain in Wacker polysilicon has been experimentally observed to be below the intrinsic level [34]. The effective recombination velocity in this case is still dependent on the excitation at the grain boundary. However, the onset of the

nonlinearity and the magnitude of the recombination velocity are both a function of the trap level.

In general the grain-boundary traps are not monoenergetic, but may be distributed in the energy gap [11], although the exact nature of the distribution is unknown. We recommend that Poisson's equation in the grain-boundary space-charge region be solved subject to a realistic distribution of trap states in the energy-gap at the grain boundary, and thus used to verify the accuracy of the results obtained using the monoenergetic-density-of-states assumption.

The solution of the minority-electron continuity equation in the base discussed in Chapter 2 is based on the gradual approximation [32], and is valid if and only if $r_G > L_n$, which restricts the analysis to relatively large grains. The base recombination current, derived from the solution of the continuity equation, comprises the one-dimensional diode current and a component of current dependent on the grain-boundary parameters. We found that the latter component was insignificant at high forward voltages. In order to obtain a general transport model we recommend that a computer-aided numerical analysis of the minority-carrier continuity equation subject to the nonlinear boundary condition at the grain boundary be done.

In Chapter 3, we determined $S_{n(\text{eff})}^{\text{GB}}$ at both unpassivated and passivated grain boundaries in Wacker (cast) polysilicon using EBIC measurements. We found that the percentage of current lost at the grain boundary is lowered as the excitation is increased, which proves that $S_{n(\text{eff})}^{\text{GB}}$ is nonlinear as described in Chapter 2. The quantitative interpretation of the EBIC measurements was facilitated by a computer-aided numerical solution of the pertinent two-dimensional continuity

equation subject to the nonlinear boundary condition at the grain boundary. By comparing the theoretical and experimental EBIC responses, we evaluated the trap density at typical passivated and unpassivated grain boundaries, assuming the trap states to be monoenergetic at midgap.

We recommend that, in order to determine the trap level in the energy gap from EBIC measurements, the expression for $S_{n(eff)}^{GB}$ used in the numerical analysis be modified to include the dependence on the trap level. Our two-dimensional numerical analysis is restricted to interpretation of EBIC measurements in relatively large-grain polysilicon. To enable the interpretation of EBIC measurements in small-grain polysilicon as well as to determine the bulk diffusion length directly from the absolute EBIC response, a refinement of our analysis to include the variations in the third-dimension is called for. It should be pointed out that the determination of the diffusion length from the absolute EBIC response requires precise measurement of the electron beam current.

In Chapter 4, we demonstrated the beneficial effects of aluminum diffusion in polysilicon. We found that high-temperature aluminum diffusion from the back surface gettered intragrain impurities in Wacker polysilicon. This finding followed from measurements of the forward current-voltage and the reverse-bias capacitance characteristics of n^+p polysilicon cells. A low-temperature aluminum diffusion from the front surface of the polysilicon resulted in effective grain-boundary passivation. The passivation was detected using EBIC measurements interpreted via the computer-aided numerical analysis developed in Chapter 3.

To optimize the aluminum-diffusion processes, we recommend fabrication of bulk and thin-film solar cells using aluminum diffusion at different temperatures and for various times. Pure aluminum is recommended for the thin-film process, since it results in deeper spikes [73] and hence effective grain-boundary passivation. The determination of the distribution of the aluminum down typical passivated grain boundaries, possibly using ion probe and/or Auger Electron Spectroscopy (AES) measurements, is called for to expedite the optimization of the passivation process.

The current-voltage characteristics measured on n^+pp^+ cells, reported in Chapter 4, implied that the conventional Al-BSF process [61] does indeed getter intragrain impurities. The benefits produced by the Al-BSF process is also commensurate with the formation of an effective BSF solar cell. The BSF, which is nonuniform and nonplanar, is formed as a result of preferential dissolution of silicon during the high-temperature process [28]. In Chapter 5 we examined the mechanisms of gettering and BSF formation using current-voltage characteristics on Wacker (cast) polysilicon cells before and after lapping off the p^+p junction. We established that the observed improvement in the (cast) polysilicon cell performance was due to gettering and that the BSF effect was inconsequential. We also demonstrated that the benefits produced by the Al-BSF process were unique to the polysilicon, i.e., no improvement in the performances of semiconductor-grade and solar-grade silicon cells was observed. This suggested that the polysilicon has unique impurities in it that are readily getterred by the aluminum.

Data obtained [75] on Wacker (cast) polysilicon indicate the prevalence of a high concentration of oxygen in polysilicon compared to

that in semiconductor-grade and solar-grade silicon. It has been shown [76] that minority-carrier lifetime is shortened due to the presence of excess oxygen. We thus surmise that aluminum getters oxygen from the polysilicon. However we do not rule out the possibility of gettering of other impurities by aluminum such as iron, cobalt, antimony, and titanium that are also present in (cast) polysilicon [75], and which form effective recombination centers. To clarify the uncertainty involved as to the type of impurities gettering by aluminum, we recommend that an AES analysis of the Al-Si system be done. Such an analysis would serve as an independent method to determine gettering.

We discuss in conclusion a few general applications of the research described in this dissertation. The solution of Poisson's equation in the grain-boundary space-charge region, i.e., the calculation of the barrier-height, is applicable also in studies of majority-carrier transport through grain boundaries, e.g., SOI MOSFETs [5] and polysilicon resistors [4]. Since a real semiconductor surface is analogous to a grain boundary, we can therefore anticipate that, in general, the recombination velocity at a semiconductor surface will be nonlinear. However, most analyses assume that the recombination velocity is constant at a surface, the validity of which is hence questionable. To remove this uncertainty, we recommend a comprehensive investigation of the recombination properties at passivated (by thermal oxides or even polysil emitters [87]), and unpassivated surfaces based on numerical interpretations of EBIC measurements.

APPENDIX A
 NUMERICAL SOLUTION OF POISSON'S EQUATION
 IN THE GRAIN-BOUNDARY SPACE-CHARGE REGION

Referring to Fig. 2.3, in which the grain boundary is located at $x=0$, we write Poisson's equation (one-dimensional) in the grain-boundary space-charge region ($0 < x < W_{SCR}^{GB}$) as

$$\frac{dE}{dx} = \frac{\rho}{\epsilon} \quad (A.1)$$

where ρ is the net charge density, ϵ is the dielectric constant of silicon, and E is the electric field in the grain-boundary space-charge region.

The net charge density in the grain-boundary space-charge region is given by

$$\rho = q[P - N - N_{AA}] \quad (A.2)$$

where N_{AA} is the grain (acceptor) doping density, q is the electron charge, and P and N are the hole and electron densities respectively in the grain-boundary space-charge region. P and N are related to the intrinsic Fermi level, E_i , through the respective quasi-Fermi levels, E_{FP} and E_{FN} :

$$P = n_i \exp\left(\frac{E_i(x) - E_{FP}}{kT}\right) \quad (A.3)$$

$$N = n_i \exp\left(\frac{E_{FN} - E_i(x)}{kT}\right) \quad (\text{A.4})$$

where n_i is the intrinsic carrier concentration. The electric field in the grain-boundary space-charge region is given by the derivative of the intrinsic Fermi level:

$$E \equiv \frac{1}{q} \frac{dE_i}{dx} \quad (\text{A.5})$$

Substituting (A.2) - (A.5) in (A.1), we get

$$\frac{d^2 E_i}{dx^2} = \frac{q}{\epsilon} Q(E_i) \quad (\text{A.6})$$

where

$$Q(E_i) = q \left[n_i \exp\left(\frac{E_i(x) - E_{FP}}{kT}\right) - n_i \exp\left(\frac{E_{FN} - E_i(x)}{kT}\right) - N_{AA} \right] \quad (\text{A.7})$$

The electric field at $x=0$ is determined by the grain-boundary surface-state charge through Gauss' law and provides one of the two boundary conditions necessary to solve (A.6):

$$\left. \frac{dE_i}{dx} \right|_{x=0} = \frac{q^2 N_{ST(eff)}^D (1-f)}{2\epsilon} \quad (\text{A.8})$$

where $N_{ST(eff)}^D$ is an effective monoenergetic density of grain-boundary states situated at the midgap (see Chapter 2) and f is the steady-state probability of electron occupancy for the surface states given in

(2.3). The second boundary condition is written in the uniformly doped quasi-neutral p-region by assuming low-injection conditions:

$$\left. \frac{dE_i}{dx} \right|_{x > W_{SCR}^{GB}} = 0 \quad . \quad (A.9)$$

The differential equation (A.6) is not homogeneous and has a nonlinear boundary condition, and hence must be solved numerically. The following numerical algorithm, called the n -method [88], has been used to solve the problem.

Let y be an approximate solution of the differential equation (A.6) that also satisfies the boundary conditions (A.8) and (A.9). Substituting $E_i(x) = y(x)$ in (A.6), we get

$$y'' - \frac{q}{\epsilon} Q(y) = 0 \quad . \quad (A.10)$$

A better approximation to the solution of the differential equation (A.10) is then given by $(y + \eta)$, where η is a small variation. Substituting this in (A.10), we get

$$(y + \eta)'' - \frac{q}{\epsilon} Q(y + \eta) = 0 \quad . \quad (A.11)$$

Expanding (A.11) by a Taylor series and neglecting higher-order terms, which is justified if η is small, we obtain

$$\eta'' - \eta \frac{q}{\epsilon} \frac{\partial Q}{\partial y} = - \left[y'' - \frac{q}{\epsilon} Q(y) \right] \quad . \quad (A.12)$$

The right side of (A.12) is known from the previous solution (A.10), and $\frac{\partial Q}{\partial y}$ can be obtained by differentiating (A.7). Thus (A.12) is a second-order differential equation in η whose boundary conditions are:

$$\eta' - \eta \frac{q}{\epsilon} \frac{\partial Q_1}{\partial y} = -[\eta' - \frac{q}{\epsilon} Q_1(y)] \quad \text{at } x = 0 \quad , \quad (\text{A.13})$$

where $Q_1 = \frac{q}{2\epsilon} N_{ST}^D (e f f) (1-f)$ is the net charge density at the grain boundary, and

$$\eta' = 0 \quad \text{for } x > W_{SCR}^{GB} \quad . \quad (\text{A.14})$$

The boundary condition (A.13) was obtained by substituting $E_i = (y + \eta)$ in (A.8), expanding by a Taylor series, and neglecting higher-order terms.

The differential equation (A.12) for η is a linear, second-order equation with linear boundary conditions, and is solved using a finite-difference approach using the Harwell subroutine DD02AD [37]. The grid size chosen was about 40 Å, which yielded good convergence and satisfactory results. Starting from an initial solution of E_i , the numerical analysis yields the correction term η , which is added to the initial solution to obtain the new value of E_i . The coefficients in (A.12) are evaluated using the new value of E_i , and (A.12) is solved again to obtain a new value of η , and so on. Convergence is reached when the correction term η is less than a certain minimum value which was chosen to be 5 meV in our analysis. This number was chosen to achieve a trade-off between the computer time required to solve the differential equation and the accuracy of the solution. The FORTRAN computer program is listed below.

```

C THIS PROGRAM SOLVES THE POISSON'S EQUATION SUBJECT
C TO NONLINEAR BOUNDARY EQUATIONS IN THE GRAIN BOUNDARY
C SPACE CHARGE REGION TO OBTAIN THE BARRIER HEIGHT
C THE DOPING DENSITY IN THE GRAIN IS READ IN; THE PROGRAM
C SOLVES FOR NST=1E10 TO 1E14; THE GRAIN BOUNDARY EXCITATION
C IS VARIED FROM EQUILIBRIUM UPTO THE LOW INJECTION LIMIT
C RAVI 29TH APRIL 1980
C MAIN PROGRAM EVALUATES THE INITIAL VALUES AND CALLS
C THE SUBROUTINE DD02AD
C IMPLICIT REAL*8(A-H,O-Z)
C COMMON W(2008)
C INTEGER*4 N,LIM,NLIN
C DIMENSION PHI(251),Y1(3),YN(3),F(251),G(251),H(251),Y(251),
C $T(1506),E(251),P(251),EQ(251)
C
C DEPINE CONSTANTS
C
C Q = 1.6D-19
C ANI = 1.33 D10
C VT = 26.0D-3
C PERM = 1.03 D-12
C CI = 1.0D-7
C CN = 1.0D-9
C EI=0.0
C EG = 1.11*Q
C ETS = 0.55*Q
C ANI2 = ANI ** 2
C CONST = ((-Q)/(PERM*VT))
C WRITE (6,110)
C #SCR1 = 1.0D-4
C
C TOTAL NO OF GRID POINTS
C
C NP = 251
C NP2 = NP + NP

```

NP3 = NP2 + NP
 NP4 = NP3 + NP
 NP5 = NP4 + NP
 NP6 = NP5 + NP

DEFINE BOUNDARIES

X1 = 0.0
 XN=MSCR1

READ IN THE DOPING CONCENTRATION

READ (5,115) ANAA

DEFINE ELECTRON AND HOLE MOBILITY EQUATIONS

UP = 47.7+(447.3/(1.+((ANAA/6.3D16)**0.76)))
 UN = 92.0+(1268./(1.+((ANAA/1.3D17)**0.91)))

DEFINE THE FERMI LEVEL

EFP = -(VT*Q)*DLOG(ANAA/ANI)
 AKP = ANI * (DEXP(-EFP/(VT*Q)))

INITIALIZE PHI VALUES TO ZERO

DO 3 I=1,NP
 PHI(I) = 0.0
 EQ(I) = 0.0
 CONTINUE
 ANSS = 1.D10

LOOP INCREMENTS THE NST VALUES

NSIZE = 2
 IF (ANSS.EQ. 1.D12) NSIZE=1

C
 C
 C

C
 C

C
 C

C
 C
 C

C
 C

3

C
 C
 C
 5


```

C POINTS
C
PHI1D = (T(NP+2)-0.5D0 *T(NP2+2) + T(NP3+3)/3 -
$0.25D0*T(NP4+3)) *Z
T(NP5+1) = (T(NP2+2)-T(NP3+3) + (11./12.) *
$T(NP4+3)) * (Z**2)
T(NP5+2) = (T(NP2+3) - T(NP3+4) + (11./12.) *
$T(NP4+4)) * (Z**2)
T(NP5-1) = (T(NP3-2) + T(NP4-2) + (11./12.) *
$T(NP5-3)) * (Z**2)
T(NP6) = (T(NP3-1) + T(NP4-1) + (11./12.) *
$T(NP5-2)) * (Z**2)
C
C TD01AD CALCULATES THE SECOND DERIVATIVES AT ALL POINTS
C
C CALL TD01AD(DX,T,NP,3,1,NP-2,4,0,T(NP5+1),EPS,T,LC,LA,2)
C
C CALCULATE THE RIGHT HAND SIDE OF THE DIFFERENTIAL EQUATION
C
DO 60 IP = 1,NP
F(IP) = 0.0
G(IP) = CONST * (AKP*DEXP(-PHI(IP)/VT) + AKN*DEXP(PHI(IP)/VT))
H(IP) = -(T(NP5+IP) + (Q/PERM) * (AKP*DEXP(-PHI(IP)/VT)
$-AKN*DEXP(PHI(IP)/VT) - ANAA))
CONTINUE
PX1 = AKP * (DEXP(-PHI(1)/VT))
ANX1 = AKN * (DEXP(PHI(1)/VT))
C
C DETERMINE THE PROBABILITY OF ELECTRON CAPTURE P'
C
ANUM = CI*ANX1+CH*ANI*(DEXP((EI-ETS)/(VT*Q)))
DEN = ANUM+CN*PX1+CI*ANI*(DEXP((ETS-EI)/(VT*Q)))
FPR = ANUM/DEN
C
C DEFINE BOUNDARY CONDITIONS
C

```

```

Y1(1) = 1.
IF (VB .NE. 0.0) GO TO 65
FPR = (1./(1.+DEXP(ETS-Q*PHI(1)-EFP)/(VT*Q))))
Y1(2) = CONST * FPR * (1.-FPR) * ANST
GO TO 66
Y1(2) = CONST*ANST*(FPR*(1.-FPR)+((PX1*ANX1-ANIZ)*CI*CN)/
$(DEN**2))
65 Y1(3) = -PHI1D - (Q/PERM) * (1.-FPR) * ANST
YN(1) = 1.
YN(2) = 0.
YN(3) = 0.
LIM = 1
EPS = 0.005

C
C DD01AD CALCULATES THE CHANGE IN BARRIER HEIGHT FROM THE
C INITIALIZED VALUES
C
CALL DD01AD(Y,X1,XN,NP,Y1,YN,P,G,H,E,LIM,EPS,K)
DO 70 JP = 1,NP
PHI(JP)=PHI(JP) + Y(JP)
CONTINUE

70
C
C CHECKING FOR CONVERGENCE
C
IF (K .EQ. -1) GO TO 30
PX1 = AKP * (DEXP(-PHI(1)/VT))
ANX1 = AKN * (DEXP(PHI(1)/VT))
IF (IV .GT. 1) GO TO 73
DO 72 LI=1,NP
EQ(LI) = PHI(LI)
CONTINUE
72 UGBD = 0.0
UGBDA = 0.0
DLEFN1 = 0.0
DLEFN2 = 0.0
IF (IK .EQ. 2 .OR. IK .EQ. 10) GO TO 74

```

```

C
C
C
74 GO TO 80
C
C DETERMINE THE ACTUAL WIDTH OF THE SPACE CHARGE REGION
C
C
C IF (IV .EQ. 1) GO TO 79
C DO 75 LM=1,NP
C LM1 = LM
C P(LM) = AKP*(DEXP(-PHI(LM)/VT))
C IF (P(LM) .GE. (0.1*ANAA)) GO TO 76
C CONTINUE
C WSCR2 = LM1 * DX
C
C
C FIND THE ELECTRON OCCUPANCY FUNCTIONS FOR DONOR (FD)
C & ACCEPTOR (FA) STATES
C
C ANUM1 = CI*ANX1+CN*ANI*DEXP((EI-ETS)/(VT*Q))
C DEN1 = ANUM1+CN*PX1+CI*ANI*DEXP((ETS-EI)/(VT*Q))
C FD = ANUM1/DEN1
C ANUM2 = CN*ANX1+CI*ANI*DEXP((EI-ETS)/(VT*Q))
C DEN2 = ANUM2+CI*PX1+CN*ANI*DEXP((ETS-EI)/(VT*Q))
C FA = ANUM2/DEN2
C
C CALCULATE THE EMISSION RATES
C
C END = CI*ANI*DEXP((ETS-EI)/(VT*Q))
C ENA = CN*ANI*DEXP((ETS-EI)/(VT*Q))
C
C CALCULATE THE NET RECOMBINATION RATE WITH AND WITHOUT THE
C PRESENCE OF ACCEPTOR STATES
C
C UGBD = CI*ANST*(1.-FD)*ANX1-END*ANST*FD
C UGBDA = UGBD+CN*ANST*(1.-FA)*ANX1-ENA*ANST*FA
C
C CALCULATE THE GRADIENT OF THE HOLE AND ELECTRON FERMI LEVELS
C ANWSR = (ANI2*(DEXP(VB/VT)))/ANAA

```

```

DLEFN1 = (Q*UGBD*WSCR2)/(UN*ANWSCR)
DLEFN2 = (Q*UGBDA*WSCR2)/(UN*ANWSCR)
PRINT OUT ALL VALUES
WRITE (6,140) VB,PHI(1),PX1,UGBD,UGBDA,DLEFN1,DLEFN2
CONTINUE
IF (ANST .GE. 1.0D14) GO TO 100
CONTINUE
INCREASE NST,NAA
ANSS = ANSS * 10.0
GO TO 5
IF (ANAA .GE. 1.D15) GO TO 150
ANAA = ANAA * 10.0
ANSS = 1.D10
GO TO 5
110 FORMAT (/26X,'NONEQUILIBRIUM POTENTIAL AT THE GB SPACE CHARGE REGI
$ON'/)
115 FORMAT (B12.3)
120 FORMAT ('1',11X,'NAA =',2X,D15.7,5X,'NST =',2X,D15.7)
130 FORMAT (/11X,'VB',15X,'PHIB',14X,'P(0)',12X,'UGBD',15X,'UGBDA',
$10X,'GRAD1',12X,'GRAD2'/)
140 FORMAT (/6X,7(D15.7,2X))
150 STOP
END
SUBROUTINE DD01AD(Y,XO,XN,NPT,YO,YN,F,G,H,E,LIM,YA,NUM)
C
C DD01AD SOLVES A 2 POINT BOUNDARY VALUE PROBLEM OF THE FORM:-
C Y'' + F(X)*Y' + G(X)*Y = H(X)
C BY A FINITE DIFFERENCE APPROXIMATION
C
C Y . . . THE FIRST NPT ELEMENTS OF THIS ARRAY ARE THE SOLUTION
C ON RETURN
C XO . . . THE LOWER LIMIT OF X
2
3
4
5
6
7
8
9

```

C C XN. . . THE UPPER LIMIT OF X
 C C NPT . . THE NUMBER OF POINTS WHERE THE VALUE OF Y IS REQUIRED
 C C (INCLUDING XO AND XN)
 C C YO. . . THE BOUNDARY CONDITION AT XO IS GIVEN BY:--
 C C $YO(1)*Y' + YO(2)*Y = YO(3)$
 C C YN. . . THE BOUNDARY CONDITION AT XN IS GIVEN BY:--
 C C $YO AND YN ARE BOTH ARRAYS OF DIMENSION AT LEAST 3.$
 C C $YN(1)*Y' + YN(2)*Y = YN(3)$
 C C IMPLICIT REAL*8 (A-H,O-Z)
 C C
 C C F) . . (ARE ALL ARRAYS OF DIMENSION AT LEAST NPT, THE FIRST
 C C G) . . (NPT ELEMENTS CONTAINING THE VALUES OF F(X), G(X), E
 C C H) . . (H(X) AT XO.....XN.
 C C E . . AN ARRAY OF AT LEAST NPT SET TO THE DIFFERENCE BETWEEN THE
 C C INITIAL APPROXIMATION AND THE CORRECTED SOLUTION. I.E. THE
 C C EFFECT OF THE THIRD AND FOURTH DIFFERENCES.
 C C LIM . . SET BY THE USER TO THE MAXIMUM NUMBER OF TIMES THE
 C C DIFFERENCE CORRECTIONS ARE TO BE APPLIED. IF CORRECTIONS
 C C ARE NOT TO BE APPLIED SET LIM=0
 C C YA. . . SET BY THE USER TO THE MAXIMUM ABSOLUTE DIFFERENCE
 C C BETWEEN THE LAST TWO APPROXIMATIONS TO Y. IF THIS IS
 C C LESS THAN YA THE ROUTINE RETURNS.
 C C NUM . . SET BY THE ROUTINE TO THE NUMBER OF TIMES THE
 C C CORRECTION TERMS ARE APPLIED. IF AFTER LIM CORRECTIONS
 C C HAVE BEEN APPLIED THEY ARE STILL GREATER THAN YA NUM IS
 C C SET TO -1
 C C W . . . THE FIRST 8*NPT WORDS OF COMMON ARE USED AS WORKING
 C C SPACE.
 C C COMMON W
 C C DIMENSION Y(1), YO(1), YN(1), F(1), G(1), H(1), E(1), W(1)
 C C EXISTS IF THERE ARE NO BOUNDARY CONDITIONS AT XO OR XN.
 C C IF LIM IS NEGATIVE THEN MOD(LIM) CORRECTIONS ARE APPLIED TO
 C C THE INITIAL APPROXIMATION IN W(3*NPT+1) TO W(4*NPT).
 C C THIS IS ONLY FOR USE AFTER A PREVIOUS CALL OF DD01AD IN THE

10
 11
 12
 13
 14
 15
 16
 17
 18
 19
 20
 21
 22
 23
 24
 25
 26
 27
 28
 29
 30
 31
 32
 33
 34
 35
 36
 37
 38
 39
 40
 41
 42
 43
 44
 45

```

C SAME PROGRAM, OTHERWISE SEVERAL ARRAY SUBSCRIPTS WILL BE
C UNDEFINED. THE RESULT WILL BE IN Y
IF(LIM) 10, 30, 30
10 LIM = -LIM
DO 20 IE = 1, NPT
Y(IE) = 0.0D0
20 CONTINUE
GO TO 110
30 IF(DABS(YO(1)) + DABS(YO(2))) 40, 40, 60
40 PRINT 50
50 FORMAT(37H NO BOUNDARY CONDITION AT XO IN DD01A)
CALL EXIT
60 IF(DABS(YN(1)) + DABS(YN(2))) 70, 70, 90
70 PRINT 80
80 FORMAT(37H NO BOUNDARY CONDITION AT XN IN DD01A)
CALL EXIT
C
C INITIALISE THE FOLLOWING FOR USE AS ARRAY SUBSCRIPTS.
90 NP = NPT
NP2 = NP + NP
NP3 = NP2 + NP
NP4 = NP3 + NP
NP5 = NP4 + NP
NP6 = NP5 + NP
NP7 = NP6 + NP
N = NP - 1
NL = NP - 2
DX = (XN - XO)/N
ZA = DX**2*0.5D0
C
C SETS UP W FOR THE EQUATIONS GIVING THE FIRST APPROXIMATION TO
C THE SOLUTION. W(2) TO W(3*NPT-1) CONTAINS THE LEFT HAND SIDE
C MATRIX, AND W(3*NPT+1) TO W(4*NPT) CONTAINS THE RIGHT HAND
C SIDE VECTOR, IN A FORM SUITABLE FOR USE IN MA07AD.
W(NP + 1) = -YO(1) + DX*YO(2) + ZA*(G(1)*YO(1) - F(1))*YO(2)
W(NP2+1) = YO(1)
81
46
47
48
49
50
51
52
53
54
55
56
57
58
59
60
61
62
63
64
65
66
67
68
69
70
71
72
73
74
75
76
77
78
79
80
81

```

```

      W(NP3+1) = DX*YO(3) + ZA*(H(1)*YO(1) - F(1)*YO(3))
      W(NP) = YN(1)
      W(NP2) = -YN(1) - DX*YN(2) + ZA*(G(NP)*YN(1) - F(NP)*YN(2))
      W(NP4) = -DX*YN(3) + ZA*(H(NP)*YN(1) - F(NP)*YN(3))
      Y(1) = 0.0D0
      E(1) = 0.0D0
      Y(NP) = 0.0D0
      E(NP) = 0.0D0
      DO 100 IB = 2, N
      Y(IB) = 0.0D0
      E(IB) = 0.0D0
      Z = 0.5*DX*F(IB)
      W(IB) = 1 - Z
      M1 = NP + IB
      M2 = NP2 + IB
      M3 = NP3 + IB
      W(M1) = DX**2*G(IB) - 2
      W(M2) = 1 + Z
      W(M3) = DX**2*H(IB)
100  CONTINUE
      NPVRT=NP3+1
C
C  MA07AD PRODUCES THE INITIAL SOLUTION IN W(3*NPVT+1) TO W(4*NPVT)
      CALL MA07AD(W, W(NPVRT), NP, NP, 3, 1, 1)
110  DO 220 J = 1, LIM
C
C  ALTERS Y TO THE LATEST SOLUTION, AND E TO THE AMOUNT OF THE
      DIFFERENCE CORRECTIONS SO FAR APPLIED.
      DO 130 IC = 1, NP
      NC = NP3 + IC
      Y(IC) = Y(IC) + W(NC)
      IF(J-1) 130, 130, 120
120  E(IC) = E(IC) + W(NC)
130  CONTINUE
C
C  IF LIM IS ZERO RETURNS BEFORE APPLYING ANY CORRECTIONS,

```

82
83
84
85
86
87
88
89
90
91
92
93
94
95
96
97
98
99
100
101
102
103
104
105
106
107
108
109
110
111
112
113
114
115
116
117

```

118 C   SETTING NUM TO ZERO.
119   IF (LIM) 140, 140, 150
120   NUM = 0
121   RETURN
122   NPVRT=NP3+1
123
124 C   TA03AD FINDS THE CENTRAL DIFFERENCES OF EVEN ORDER UP TO FOUR.
125   CALL TA03AD(W(NPVRT), NP, 1, 1, NP, 4, 0)
126
127 C   SETS THE COEFFICIENTS IN THE MATRIX EQUATION TO FIND THE
128   CORRECTION DUE TO THE HIGHER ORDER DIFFERENCES.
129   W(NP7+2) = W(NP7+3)
130   W(NP6+2) = W(NP6+3) - W(NP7+2)
131   NA = NP7 + N
132   W(NA) = W(NA-1)
133   NB = NP6 + N
134   W(NP7) = W(NA) + W(NB)
135   DO 190 J2 = 2, N
136   IF (F(J2)) 170, 160, 170
137   CA=0.0D0
138
139   GO TO 180
140   NC = NP6 + J2 + 1
141   CA = -(W(NC-1) + W(NC))/12
142   NE = NP7 + J2
143   CB = -W(NE)/12
144   NF = NP3 + J2
145   W(NF) = -(CB + CA*DX*F(J2))
146   CONTINUE
147   W(NP3+1) = Y0(1)*(4*W(NP6+2) + 3*W(NP7+2))/24
148   W(NP4) = YN(1)*(W(NA-1) - 4*W(NP7))/24..
149   NPVRT=NP3+1
150
151 C   MA07AD SOLVES THE EQUATION AND PUTS THE CORRECTION TERMS IN
152   W(J*NP3+1) TO W(4*NP3).
153   CALL MA07AD(W, W(NPVRT), NP, NP, 3, 1, 0)

```

```

C   CHECKS IF ANY DIFFERENCE CORRECTIONS ARE GREATER THAN YA. IF NOT
C   IT APPLIES THE CORRECTION, ALTERS E,SETS NUM AND RETURNS.
DO 200 ID = 1, NP
NG = NP3 + ID
IF (DABS(W(NG)) - YA) 200, 200, 220
200 CONTINUE
DO 210 JJ = 1, NP
NH = NP3 + JJ
E(JJ) = E(JJ) + W(NH)
Y(JJ) = Y(JJ) + W(NH)
210 CONTINUE
NH = J
RETURN
220 CONTINUE
C
C   NO SOLUTION OF THE PROBLEM WITHIN THE DESIRED ACCURACY HAS
C   BEEN FOUND AFTER LIM APPLICATIONS OF THE CORRECTION TERMS.
NUM = -1
RETURN
END
SUBROUTINE TAO3AD(Y, MU, NL, NS, NU, NO, LO)
IMPLICIT REAL*8(A-H, O-Z)
C   EVALUATES CENTRAL DIFFERENCES
DIMENSION Y(MU, 1)
LOJ=LO+1
NH=NS/2
NSH=NS-NH
L=NL+NS
M=NU
DO 11 J=1, NO
GO TO (1, 2, 3), LOJ
JA=J+1
JB=J
GO TO 6
2   JA=(J+3)/2
11
12
13
14
15
16
171
172
173
1   1
2   2
3   3
4   4
5   5
6   6
7   7
8   8
9   9
10  10
11  11
12  12
13  13
14  14
15  15
16  16

```



```

18 M=M-NS
11 CONTINUE
   RETURN
   END
   SUBROUTINE TD01AD(H,Y,MU,NL,NS,NU,NO,LO,A,T,E,LC,LA,NTH)
C
C   A ROUTINE TO CALCULATE FIRST AND SECOND DERIVATIVES USING
C   CENTRAL DIFFERENCES
   IMPLICIT REAL*8(A-H,O-Z)
   DIMENSION Y(MU,1),A(1),E(1)
   NH=NS/2
   LOJ=LO+1
   IF(NTH-2)10,20,30
C
C   SETS THE COEFFICIENT C TO C=1/(2*H) WHEN FIRST DERIVATIVES ARE
C   REQUIRED
   10 C=0.5D0/H
   GO TO 50
C
C   SETS THE COEFFICIENT C TO C=1/(H*H) WHEN SECOND DERIVATIVES ARE
C   REQUIRED
   20 C=1D0/(H*H)
   GO TO 50
   30 LC=7
C
C   SUBROUTINE HAS BEEN ASKED FOR DERIVATIVES GREATER THAN 2. PRINT
C   ERROR MESSAGE
   PRINT 40
   CALL EXIT
   40 FORMAT(67H SUBROUTINE TD01A IS DESIGNED ONLY FOR FIRST AND SECOND
   1DERIVATIVES)
C
C   SET COUNTERS TO INITIAL VALUES
   50 K=0
   K2=NTH
C

```

53
54
55
56
1
2
3
4
5
6
7
8
9
10
11
12
13
14
15
16
17
18
19
20
21
22
23
24
25
26
27
28
29
30
31
32

```

33 C SET COUNTER TO ZERO IN ORDER TO SUM
34 DO 60 I=NL,NU,NS
35 A(I)=ODD
36 60 CONTINUE
37 IF(NO-NTH) 70, 90, 90
38
39 NOT ENOUGH DIFFERENCES SUPPLIED. PRINT ERROR MESSAGE
40 LC=7
41 PRINT 80
42 CALL EXIT
43 80 FORMAT(1X, 106H SUBROUTINE TD01A REQUIRES DIFFERENCES OF ORDER AT LE
44 1AST AS LARGE AS THE ORDER OF DERIVATIVE TO BE CALCULATED)
45
46 C ADDS ONE TERM OF THE SERIES E(I) ON TO THE SUM A(I) PER
47 ITERATION
48 90 DO 290 LB=NTH, NO, 2
49 LA=LB
50 GO TO (100, 110), NTH
51 100 GO TO (120, 130, 210), LOJ
52 110 GO TO (120, 210, 130), LOJ
53 120 J=LA
54 GO TO 220
55 130 IF(NS-1) 190, 140, 190
56 140 LC=7
57 GO TO (150, 170), NTH
58 150 PRINT 160
59 CALL EXIT
60 160 FORMAT(1X, 106H FIRST DERIVATIVES CANNOT BE CALCULATED BY SUBROUTIN
61 1E TD01A BECAUSE ODD DIFFERENCES HAVE BEEN OVERWRITTEN)
62 170 PRINT 180
63 CALL EXIT
64 180 FORMAT(1X, 106H SECOND DERIVATIVES CANNOT BE CALCULATED BY SUBROUTIN
65 1E TD01A BECAUSE EVEN DIFFERENCES HAVE BEEN OVERWRITTEN)
66 190 GO TO (210, 200), NTH
67 200 J=LA/2+1
68 GO TO 220

```

```

210 J=(LA+1)/2
220 GO TO (230,250),NTH
230 DO 240 I=NL,NU,NS
    IB=I-NH
    IC=IB+NS
C
C    FIND NEXT TERM OF SERIES FOR FIRST DERIVATIVES
    E(I)=C*(Y(IB,J+1)+Y(IC,J+1))
240 CONTINUE
    GO TO 270
250 DO 260 I=NL,NU,NS
C
C    FIND NEXT TERM OF SERIES FOR SECOND DERIVATIVES
    E(I)=C*Y(I,J+1)
260 CONTINUE
C
C    ROUTINE TO DECIDE WHETHER SUM IS CONVERGING,HAS CONVERGED,ETC
270 CALL TD01BD(A,T,E,LC,LA,NL,NS,NU,NO,NTH)
    IF(LC)300,280,300
280 K=K+1
    K2=K2+2
C
C    SET COEFFICIENT C FOR NEXT ITERATION
    C=-K*K*C/(K2*(K2-1D0))
290 CONTINUE
    LC=3
300 RETURN
    END
SUBROUTINE TD01BD(A,T,E,LC,LA,IL,IS,IU,NO,L1)
C
C    THIS ROUTINE DECIDES WHETHER OR NOT ANOTHER ITERATION IS TO BE
    TAKEN. A VALUE OF LC IS SET ACCORDING TO THE FOLLOWING
    CONDITIONS
C    VALUE
C    OF LC

```

69
70
71
72
73
74
75
76
77
78
79
80
81
82
83
84
85
86
87
88
89
90
91
92
93
94
95
96
97
98
99
100
101
102
103
104

```

C 0   REQUIRED TOLERANCE NOT REACHED.FIND NEXT TERM.
C 1-5  SEE WRITE UP FOR EXPLANATION.
      IMPLICIT REAL*8(A-H,O-Z)
      DIMENSION A(1),E(1)
      BN=ODD
      IF(T)80,10,10
10    SN=ODD
      DO 30 I=IL,IU,IS
      WS=DABS(E(I))
      SN=SN+WS
      IF(BN-WS)20,30,30
20    BN=WS
30    CONTINUE
      SN=SN*IS/(IU-IL+IS)
      IF(LA-L1)40,80,40
40    IF(SO-BN)50,50,80
50    IF(LA-NO)70,60,70
60    LC=4
      RETURN
70    LC=5
      RETURN
80    DO 90 I=IL,IU,IS
      A(I)=A(I)+E(I)
90    CONTINUE
      SO=SN
      IF(BN-T)100,100,130
100   IP(LA-NO)120,110,120
110   LC=2
      RETURN
120   LC=1
      RETURN
130   LC=0
      RETURN
      END
      SUBROUTINE MA07AD (A,B,MO,NO,NG,NR,NL)
C##### 18/05/70 LAST LIBRARY UPDATE

```

105

106

107

108

109

110

111

112

113

114

115

116

117

118

119

120

121

122

123

124

125

126

127

128

129

130

131

132

133

134

135

136

137

138

1

2

C IMPLICIT REAL*8(A-H,O-Z)
 C SOLVES SETS OF LINEAR EQUATIONS OF THE FORM $A \cdot X = B$, WHERE A IS A
 C SQUARE MATRIX OF ORDER NO AND X, B ARE MATRICES EACH WITH NO ROWS
 C AND NR COLUMNS. THE SOLUTION X OVERWRITES THE RHS B. THE ONLY
 C NON ZERO ELEMENTS OF A APPEAR IN A BAND OF WIDTH NW CENTRED ON THE
 C DIAGONAL.
 C AND J TH COLUMN OF A AND B MUST BE WRITTEN INTO A(I,J-I+(NW+1)/2)
 C AND B(I,J) RESPECTIVELY AND THE FIRST DIMENSION OF THE ARRAYS A,B
 C MUST BE MO IN THE CALLING ROUTINE. NL MUST BE NON ZERO UNLESS
 C THE SAME LHS IS TO BE USED REPEATEDLY IN WHICH CASE SPEED CAN BE
 C GAINED AFTER THE INITIAL ENTRY TO THE SUBROUTINE BY LEAVING THE
 C ARRAY A IN THE FORM PRODUCED BY THE INITIAL ENTRY AND SETTING NL
 C TO ZERO FOR SUBSEQUENT ENTRIES.
 C DIMENSION A(MO,1),B(MO,1)
 C M=(NW+1)/2
 C MM1=M-1
 C I=NO
 C DO 14 L1=1,NO
 C IF(NL)1,4,1
 C A(I,M)=1.0/A(I,M)
 C J=MM1
 C DO 3 L2=1,MM1
 C IF(I+J-N)4,4,2
 C A(I,J)=A(I,J)*A(I,M)
 C J=J-1
 C CONTINUE
 C DO 5 L=1,NR
 C B(I,L)=B(I,L)*A(I,M)
 C CONTINUE
 C IF(I-1)15,15,6
 C DO 12 K=1,MM1
 C I1=I-K
 C IF(I1)13,13,7
 C I2=N+K
 C IF(NL)8,11,8
 C J=MM1

3
 4
 5
 6
 7
 8
 9
 10
 11
 12
 13
 14
 15
 16
 17
 18
 19
 20
 21
 22
 23
 24
 25
 26
 27
 28
 29
 30
 31
 32
 33
 34
 35
 36
 37
 38

1

2

3

4

5

6

7

8

```

39 DO 10 L2=1,MM1
40 IF(I+J-M)11,11,9
41 I3=J+K
42 A(I1,I3)=A(I1,I3)-A(I,J)*A(I1,I2)
43 J=J-1
44 CONTINUE
45 DO 12 L=1,NR
46 B(I1,L)=B(I1,L)-B(I,L)*A(I1,I2)
47 CONTINUE
48 I=I-1
49 CONTINUE
50 DO 19 I=2,NO
51 J=MM1
52 DO 18 L1=1,MM1
53 I1=I+J-M
54 IF(I1)19,19,16
55 DO 17 L=1,NR
56 B(I,L)=B(I,L)-B(I1,L)*A(I,J)
57 CONTINUE
  J = J-1
  CONTINUE
  CONTINUE
  RETURN
  END

```

9

10

11

12

13

14

15

16

17

18

19

APPENDIX B
MATHEMATICAL JUSTIFICATION FOR USING THE FOLDING TECHNIQUE

Consider the n^+p junction shown in Fig. 3.2 with an arbitrary volume distribution of the generation rate. The right- and left-side grains are assumed to be semi-infinite in the positive and negative x -directions respectively, and the grain boundary is situated at $x=0$. We will first formulate the general problem without using the folding technique, i.e., without considering the grain boundary as a surface, and then demonstrate the justification for using the folding technique.

In the right-side grain, the minority electron continuity equation, under low-injection conditions, can be written as

$$\frac{\partial^2 N_R}{\partial x^2} + \frac{\partial^2 N_R}{\partial y^2} + \frac{\partial^2 N_R}{\partial z^2} - \frac{N_R}{L_n^2} + \frac{g_R}{D_n} = 0 \quad (\text{B.1})$$

where L_n is the electron diffusion length, D_n is the electron diffusion coefficient, g_R is the generation rate (per unit volume per second), and N_R is the electron concentration at any point in the right-side grain. The boundary conditions for this problem are $N_R(z = 0) = 0$ at the edge of the (shorted) junction space-charge region; $N_R(z = \infty) = 0$ since $L_n < W_B$, where W_B is the width of the base; $N_R(x = \infty) = 0$ since the grain is semi-infinite ($\gg L_n$) in the x -direction; and at the edge of the grain-boundary space-charge region in the right-side grain ($x=0^+$),

$$D_n \frac{\partial N_R}{\partial x} = S_{n(\text{eff})}^{\text{GB}} N_R \quad , \quad (\text{B.2})$$

which defines $S_{n(\text{eff})}^{\text{GB}}$ (see Chapter 2). The boundary condition (B.2) accounts for only those carriers that flow towards the grain boundary from the right-side grain and recombine there. Any carriers that are transmitted through the grain boundary to the left-side grain as well as those carriers that are generated there can be accounted for by formulating the problem in the left-side grain.

In the left-side grain we can write the differential equation analogous to that in the right-side grain:

$$\frac{\partial^2 N_L}{\partial x^2} + \frac{\partial^2 N_L}{\partial y^2} + \frac{\partial^2 N_L}{\partial z^2} - \frac{N_L}{L_n^2} + \frac{g_L}{D_n} = 0 \quad (\text{B.3})$$

where N_L is the electron concentration and g_L is the generation rate (per unit volume per second) at any point in the left-side grain. We have assumed that the diffusion lengths in the two grains are equal. The boundary conditions for this problem are $N_L(z=0) = 0$; $N_L(z=\infty) = 0$; $N_L(x=\infty) = 0$; and at the edge of the grain-boundary space-charge region in the left-side grain ($x=0^-$),

$$- D_n \frac{\partial N_L}{\partial x} = S_{n(\text{eff})}^{\text{GB}} N_L \quad . \quad (\text{B.4})$$

The quasi-equilibrium approximation ensures that $N_L(0^-) = N_R(0^+)$ and hence that $S_{n(\text{eff})}^{\text{GB}}$ has the same value at $x=0^+$ and at $x=0^-$. Note

that $S_{n(\text{eff})}^{\text{GB}}$ in (B.2) and (B.4) is dependent on the excitation at the grain boundary (see Chapter 2). The total current, I_{EBIC} , collected at the junction ($z=0$) is

$$I_{\text{EBIC}} = q D_n \int_{-\infty}^{\infty} \int_{-\infty}^{\infty} \left[-\frac{\partial N_R}{\partial z} + \frac{\partial N_L}{\partial z} \right]_{z=0} dx dy \quad . \quad (\text{B.5})$$

Hence in order to obtain the collected current, it is necessary to solve (B.1) and (B.3) subject to the respective boundary conditions.

The folding technique [26] enables us to simplify this problem. Provided the differential equations (B.1) and (B.3) are linear, we can add them to get

$$\frac{\partial^2 N}{\partial x^2} + \frac{\partial^2 N}{\partial y^2} + \frac{\partial^2 N}{\partial z^2} - \frac{N}{L_n} + \frac{g}{D_n} = 0 \quad (\text{B.6})$$

where $N = N_R + N_L$ is the folded sum of the electron concentrations in the right- and in the left-side grains and $g = g_R + g_L$ is the total generation rate. It is important to recognize that the addition of the differential equations (B.1) and (B.3) to yield (B.6) is possible only if L_n is the same in the two grains. The boundary conditions are $N(z=0) = 0$; $N(z \rightarrow \infty) = 0$; $N(x \rightarrow \infty) = 0$; and at $x=0$,

$$D_n \frac{\partial N_R}{\partial x} + \left| -\frac{\partial N_L}{\partial x} \right| = S_{n(\text{eff})}^{\text{GB}} [N_R + N_L] \quad ,$$

or

$$D_n \frac{\partial N}{\partial x} = S_{n(\text{eff})}^{\text{GB}} N \quad . \quad (\text{B.7})$$

We stress that in order to obtain (B.7) we have assumed that quasi-equilibrium prevails across the grain-boundary space-charge region, which ensures $S_{n(\text{eff})}^{\text{GB}}$ has the same value on either side of the grain boundary.

We have thus provided a mathematical justification for using the folding technique. The solution of the differential equation (B.6) yields the folded sum of the electron concentrations in the left- and right-side grains, $(N_R + N_L)$, and is equivalent to solving the differential equations (B.1) and (B.3). The boundary condition (B.7) accounts for the carriers in both grains that recombine at the grain boundary. The total current, I_{EBIC} , given by (B.5) can be calculated from the solution of (B.6) as described in Chapter 3.

APPENDIX C
NUMERICAL ALGORITHM FOR SOLVING THE TWO-DIMENSIONAL CONTINUITY EQUATION
UNDERLYING THE EBIC RESPONSE

We describe here the basic numerical algorithm used to solve the two-dimensional electron continuity equation formulated in Chapter 3. It should be pointed out that our algorithm is not necessarily the most efficient one. The method was found to be successful, and hence it was utilized without additional considerations.

C.1 Numerical Solution of the Steady-State Continuity Equation

To obtain the EBIC response we must first solve the electron continuity equation (3.6) under low-injection conditions in the p-type base,

$$\frac{\partial^2 N}{\partial x^2} + \frac{\partial^2 N}{\partial z^2} - \frac{N}{L_n^2} + \frac{G}{D_n} = 0 \quad , \quad (C.1)$$

subject to the appropriate boundary conditions. The Gauss-Seidel elimination method [57, 58], with successive-overrelaxation, is used to obtain the solution of (C.1), $N(x,z)$.

A rectangular grid system was employed over the x-z plane. Two different sets of grid sizes were used. The finer grid system was employed in the region around the generation source. Each point is labeled (i,j), which indicates its coordinate position. If Δx and Δz are the coarse mesh sizes in the x- and z-directions respectively, then

$$x_i = (i-1)\Delta x, \quad i = 1, 2, 3, \dots, \quad (C.2)$$

$$z_j = (j-1)\Delta z, \quad j = 1, 2, 3, \dots$$

are the coordinate positions. The fine mesh sizes $\Delta x'$ and $\Delta z'$ are calculated as follows:

$$\Delta x' = \Delta x / (K-1) \quad , \quad (C.3)$$

$$\Delta z' = \Delta z / (L-1) \quad ,$$

where K and L are the number of fine mesh points in the x - and z -directions respectively. The values of K and L are chosen by trial-and-error so as to minimize the computer time and maximize the accuracy. The excess electron density at each point is indicated by

$$N(x_i, z_j) \equiv N_{i,j} \quad . \quad (C.4)$$

A finite difference form of (C.1) can be written at each interior point in the coarse mesh region using the following approximations [57]:

$$\frac{\partial^2 N_{i,j}}{\partial x'^2} \approx \frac{N_{i+1,j} - 2N_{i,j} + N_{i-1,j}}{\Delta x'^2} \quad (C.5)$$

and

$$\frac{\partial^2 N_{i,j}}{\partial z^2} = \frac{N_{i,j+1} - 2N_{i,j} + N_{i,j-1}}{\Delta z^2} \quad (C.6)$$

In the fine mesh region similar equations can be written by replacing Δx and Δz by $\Delta x'$ and $\Delta z'$ respectively. The differential equation (C.1) can now be written in finite-difference form using (C.5) and (C.6):

$$\frac{N_{i+1,j} - 2N_{i,j} + N_{i-1,j}}{\Delta x^2} + \frac{N_{i,j+1} - 2N_{i,j} + N_{i,j-1}}{\Delta z^2} - \frac{N_{i,j}}{L_n^2} + \frac{G_{i,j}}{D_n} = 0 \quad (C.7)$$

Rearranging, we obtain

$$N_{i,j} = \frac{N_{i+1,j} + N_{i-1,j} + (N_{i,j+1} + N_{i,j-1})A + G_{i,j}\Delta x^2/D_n}{(2 + 2A + \Delta x^2/L_n^2)} \quad (C.8)$$

where $A = \frac{\Delta x^2}{\Delta z^2}$. The finite-difference form in the fine-mesh region can also be rearranged to obtain an expression for $N_{i,j}$ similar to that in (C.8), with Δx and Δz replaced by $\Delta x'$ and $\Delta z'$.

The value of $G_{i,j} \equiv G(x_i, z_j)$ in (C.8) is evaluated at each grid point using the appropriate model, i.e., spherical or Gaussian, to describe the generation rate distribution. For a spherical-source model, the value of G at each interior point is given by a constant value (see Chapter 3), and for a Gaussian-source model G is evaluated using (3.17). The total generation rate G_0 (electron-hole pairs/sec) is chosen such that the theoretically calculated maximum EBIC in the grain is equal to the experimentally observed value.

Equation (C.8) is evaluated at each interior grid point, using the dependent and independent boundary conditions to define the values of N

at the boundaries. These values are then overrelaxed by using a weighting factor w [89]:

$$N_{i,j_{\text{new}}} = wN_{i,j} + (1-w)N_{i,j_{\text{old}}} \quad . \quad (\text{C.9})$$

Equation (C.9) is used in conjunction with (C.8) to successively assign new values to the excess electron density at each interior point. The procedure is iterated until some acceptable difference between the old and new values of electron density at each interior point is achieved. The number of iterations required to obtain a given accuracy depends on the value of the weighting factor used as well as the coarse and fine mesh sizes used.

The sizes of the coarse grid used in our analysis were about $2 \mu\text{m}$ in the x -direction and $3 \mu\text{m}$ in the z -direction. The values of K and L were 49 and 13 respectively. The value of the weighting factor used was $w = 1.9$ [89]. The required CPU times using an AMDAHL 470 computer were typically about 200 seconds to obtain a single EBIC line scan, i.e., to solve (C.1) and to calculate the EBIC at nine different positions of the beam.

The independent boundary conditions at $z = 0$, $z \rightarrow \infty$, and $x \rightarrow \infty$ were incorporated into the solution by simply assigning the excess electron density values to the respective boundary grid points. For example, at the edge of the junction space-charge region, $N_{i,1} = 0$ for $i = 1, 2, 3, \dots$

The dependent boundary condition at $x=0$ is modified every time N is evaluated. The dependent boundary condition in this problem involves the normal derivative at the edge of the grain-boundary space-charge region, and can be numerically evaluated using Newton's forward

interpolation formula [58]. Differentiating the three-point version of this formula, we obtain the following one-sided derivative approximation:

$$\frac{\partial N_{1,j}}{\partial x} = \frac{-N_{3,j} + 4N_{2,j} - 3N_{1,j}}{2\Delta x} \quad \text{for } j = 1, 2, 3, \dots \quad (\text{C.10})$$

The relation (C.10) can be used to evaluate, after each iteration, the electron density at the edge of the grain-boundary space-charge region:

$$D_n \frac{-N_{3,j} + 4N_{2,j} - 3N_{1,j}}{2\Delta x} = S_{n(\text{eff})}^{\text{GB}} N_{1,j} \quad (\text{C.11})$$

In (C.11) $S_{n(\text{eff})}^{\text{GB}}$ is, in general, dependent on N at the grain boundary (see Chapter 2), and is evaluated after each iteration. Rewriting (C.11), we obtain

$$N_{1,j} = \frac{4N_{2,j} - N_{3,j}}{[(2\Delta x S_{n(\text{eff})}^{\text{GB}}/D_n) + 3]} \quad (\text{C.12})$$

C.2 Numerical Evaluation of the Currents

The total generation current in the base is

$$q \int_0^{\infty} \int_0^{\infty} G \, dx \, dz = qG_0 = I_{\text{GB}}^{\text{B}} + I_{\text{QN}}^{\text{B}} + I_{\text{EBIC}} \quad (\text{C.13})$$

where I_{GB}^{B} is the grain-boundary recombination current, I_{QN}^{B} is the quasi-neutral-base recombination current, and I_{EBIC} is the collected junction

current. The values of the current on the right side of (C.13) are calculated numerically and compared with the total generation current qG_0 to serve as a convergence check. The numerical procedure is stopped when (C.13) is satisfied to within 5% accuracy.

We now discuss the numerical evaluation of I_{GB}^B , I_{QN}^B , and I_{EBIC} . The grain-boundary recombination current is given by

$$I_{GB}^B = q \int_0^{\infty} S_{n(\text{eff})}^{GB} N \Big|_{x=0} dz \quad . \quad (\text{C.14})$$

Note that the value of $S_{n(\text{eff})}^{GB}$ at any point along the edge of the grain-boundary space-charge region is dependent on the excitation at that point (see Chapter 2). The integral in (C.14) is evaluated using the trapezoidal rule [57]. The quasi-neutral-base recombination current is obtained by integrating, using the trapezoidal rule [57], the electron density divided by the lifetime in the base:

$$I_{QN}^B = q \int_0^{\infty} \int_0^{\infty} \frac{N}{\tau_n} dx dz \quad . \quad (\text{C.15})$$

The EBIC collected at the junction is given by

$$I_{EBIC} = qD_n \int_{x=0}^{\infty} \frac{\partial N}{\partial z} \Big|_{z=0} dx \quad . \quad (\text{C.16})$$

The derivative of N at $z=0$ in (C.16) is obtained using Newton's forward interpolation formula [58] in the z -direction. Differentiating the three-point version of this formula yields an expression similar to (C.10):

$$\frac{\partial N_{i,1}}{\partial z} = \frac{-N_{i,3} + 4N_{i,2} - 3N_{i,1}}{2\Delta z} \quad . \quad (C.17)$$

The integral in (C.16) is then evaluated using the trapezoidal rule [57] to obtain I_{EBIC} .

The boundaries in the x- and z-directions in our analysis were fixed at about three diffusion lengths away from the center of the generation source. The electron concentration at three diffusion lengths away from the center of the generation source, obtained from the numerical analysis, was at least five orders of magnitude lower than the maximum value, which justifies our choice of the boundaries. The number of coarse and fine mesh points have been chosen by trial and error, and the method yields good convergence. The FORTRAN computer program to solve the continuity equation as well as to calculate the currents is listed below.

```

C THIS PROGRAM SOLVES THE TWO DIMENSIONAL CONTINUITY EQUATION FOR
C THE CASE WHEN AN ELECTRON BEAM IS INCIDENT FROM THE FRONT SURFACE
C THE GENERATION IS MODELED BY EITHER A GAUSSIAN OR A SPHERICAL
C DISTRIBUTION .....RAVL.....21ST FEBRUARY 1983.....
C THE GRAIN BOUNDARY RECOMBINATION VELOCITY CAN BE EITHER CONSTANT
C OR NONLINEAR; IF SGB IS CONSTANT THEN SET IVEL=0; IF SGB IS
C NONLINEAR THEN SET IVEL=1
C THE GENERATION SOURCE CAN BE A GAUSSIAN OR A SPHERICAL SOURCE
C FOR SPHERICAL SOURCE SET IGEN=1; FOR GAUSSIAN SET IGEN=0
C
C REAL NOLD(150,201),NGS(150,201),LN,IEBIC,IEBIC1,IEBIC2,IEBIC3
C $,IGB,IGB1,IGD2,ITOT,NDD,NSTD,NSTA
C COMMON DN,LN,NGS
C DIMENSION SRON(150), VAL(25,201),G(15,201)
C
C INPUT CONSTANTS
C Q = 1.6E-19
C
C SET THE INITIAL CONDITIONS -GAUSSIAN OR SPHERICAL SOURCE
C AND SGB NONLINEAR OR CONSTANT
C
C READ (5,199)IGEN,IVEL
C
C DN IS THE DIFFUSION COEFFICIENT;EKEV IS THE BEAM ENERGY
C IN KEV;LN IS THE DIFFUSION LENGTH IN CM;GVOL IS HALF THE TOTAL
C GENERATION RATE;S IS THE VALUE OF THE RECOMBINATION VELOCITY
C AT THE GB;NDD IS THE DOPING DENSITY
C
C READ (5,200)DN,EKEV,LN,GVOL,S,NDD
C IF (IVEL .EQ. 0)GO TO 1
C
C NSTD IS THE DONOR TRAPS AT THE GB;NSTA IS THE ACCEPTOR
C TRAPS AT THE GB;CN IS THE NEUTRAL CAPTURE RATE;

```

```

C C
C C
C C
1  C I IS THE IONIZED CAPTURE RATE
    READ (5,201) NSTD, NSTA, CN, CI
    XJ=0.8E-4
    XO = 0.0036
    ZO = (1.E-4)*0.0171*((LEKEV)**1.75)
    IF (IGEN.EQ. 1) ZO=ZO/3.
    WRITE (6,203)
    GOUT=2.0*GVOL
    WRITE (6,204) EKEV, GOUT
    WRITE (6,205) NDD, LN, S
    IF (IVEL.EQ. 0 .AND. IGEN.EQ. 0) GO TO 3
    IF (IVEL.EQ. 0 .AND. IGEN.EQ. 1) GO TO 4
    WRITE (6,206)
    WRITE (6,207) NSTD, NSTA, CN, CI
    GO TO 5
4  WRITE (6,210)
C C
C C
C C
C C
5  SET UP COARSE MESH SPACING IN THE Z AND X DIRECTIONS
    XJ IS THE JUNCTION DEPTH AND IS ACCOUNTED FOR IN THE
    ANALYSIS
    HZO = (1.1*ZO-XJ)/3.
    IF (IGEN.EQ. 1) HZO=(3.0*ZO-XJ)/3.
    NZ = INT((ZO+2.5*LN)/HZO)+1
    NVAR = 16
    DUMMY = XO/NVAR
    NTEST = INT((XO+2.5*LN)/DUMMY)+1
    IF (NTEST.LT. 155) GO TO 10
    NVAE = NVAR-1
    GO TO 6
6  HXO = DUMMY
    HX = NTEST
    HX = HXO
    HZ = HZO
10
20

```

```

C
C EPS = 0.1
C CHOOSE THE FINE MESH POINTS; DY PRIOR EXPERIENCE # OF POINTS IS
C CHOSEN HERE
C
C   NZZ = 13
C   NZZ1 = NZZ-1
C   HZZ = (1.1*Z0-XJ)/(NZZ1)
C   NXX = 49
C   HXX = 4.0*HX0/(NXX-1)
C   NAME = INT((HZ/HZZ)+0.1)
C
C NPZ IS THE TOTAL NO OF POINTS IN THE Z DIRECTION;NZZ IS THE # OF
C POINTS IN THE FINE MESH; NZ IN THE COARSE MESH
C NPX IS THE TOTAL NO OF POINTS IN THE X DIRECTION;NXX IS THE # POINTS
C IN THE FINE MESH;NX IN THE COARSE MESH
C THE COARSE MESH IN THE X DIRECTION IS CHOSEN TO BE ABOUT 40M FROM X0
C
C   NPX = NX+NXX-5
C   NPZ = NZ+NZZ-5
C   NROW1 = NZZ
C
C KOL1 IS THE START OF THE FINE MESH;KOL2 IS THE END
C
C   KOLA=INT(0.01+(X0-(2.*HX))/HX))+1
C   KOL1=KOLA
C   IF (KOLA .LT. 1) KOL1=1
C   KCL11 = KOL1-1
C   KOL2 = KCL1+NXX-1
C   INDEX=(NXX-1)/4
C   IF (KOLA .LT. 1) KOL2=KOL1+3*INDEX
C   KCL22 = KOL2+1
C   KCL12 = KOL1+1
C   KCL21 = KOL2-1
C   IF (KOLA .LT. 1) NPX=NPX-INDEX
C   NPX1 = NPX-1

```



```

HZ1 = HZ
GO TO 50
IND1 = 1
HZ1 = HZZ
C
C   IGB1 IS THE CURRENT IN THE REGION BETWEEN 0 AND 1.1Z0
C
50  IGB1 = NGS (1, 1) + NGS (NZZ, 1)
    KO1 = 1 + IND1
    IF (IVEL .EQ. 0) GO TO 55
    IGB1 = NGS (NZZ, 1) * SNON (NZZ)
    DO 60 K = KO1, NZZ1, IND1
    IF (IVEL .NE. 0) GO TO 57
    IGB1 = IGB1 + NGS (K, 1) * 2.0
    GO TO 60
57  IGB1 = IGB1 + NGS (K, 1) * SNON (K) * 2.0
60  CONTINUE
C
C   USE TRAPEZOIDAL RULE TO INTEGRATE TO GET THE TOTAL CURRENT
C
    IF (IVEL .EQ. 0) GO TO 65
    IGB1 = 0 * IGB1 * HZ1 / 2.
    GO TO 67
65  IGB1 = IGB1 * 0 * S * HZ1 / 2.
67  NZZ2 = NZZ + 1
C
C   IGB2 IS THE GB CURRENT FROM 1.1*Z0 TO THE BOUNDARY
C
    IGB2 = NGS (NZZ, 1) + NGS (NPZ, 1)
    IF (IVEL .EQ. 0) GO TO 68
    IGB2 = NGS (NZZ, 1) * SNON (NZZ)
    DO 70 L = NZZ2, NPZ1
    IF (IVEL .NE. 0) GO TO 69
    IGB2 = IGB2 + NGS (L, 1) * 2.0
    GO TO 70
69  IGB2 = IGB2 + NGS (L, 1) * 2.0 * SNON (L)

```

```

70 CONTINUE
C
C INTEGRATE USING TRAPEZOIDAL RULE
C
IF (LEVEL.EQ. 0) GO TO 75
IGB2=Q*IGB2*HZ/2.
GO TO 77
75 IGB2 = IGB2*Q*S*HZ/2.
77 NR1 = 1+NAME
NR2 = 1+2*NAME
IF (KOL1 .EQ. 1) GO TO 85
C
C CALCULATE THE COLLECTED CURRENT
C IEBIC1 IS THE CURRENT COLLECTED FROM GB UP TO KOL1-COARSE REGION
C
IEBIC1=(4.0*(NGS(NR1,1)+NGS(NR1,KOL1))-(NGS(NR2,1)+
$NGS(NR2,KOL1)))/(2.0*HZ)
IF (KOL11.EQ. 1) GO TO 82
DO 80 M=2,KOL11
IEBIC1=IEBIC1+(2.0*(4.0*NGS(NR1,M)-NGS(NR2,M)))/(2.0*HZ)
CONTINUE
80
C
C USE TRAPEZOIDAL RULE TO INTEGRATE
C
IEBIC1=IEBIC1*Q*DN*HX/2.
GO TO 90
85 IEBIC1=0.0
C
C IEBIC2 IS THE CURRENT COLLECTED IN THE FINE MESH REGION
C
IEBIC2=(4.0*(NGS(2,KOL1)+NGS(2,KOL2))-(NGS(3,KOL1)+
$NGS(3,KOL2)))/(2.0*HZZ)
DO 100 MM=KOL12,KOL21
IEBIC2=IEBIC2+(2.0*(4.0*NGS(2,MM)-NGS(3,MM)))/(2.0*HZZZ)
CONTINUE
100 IEBIC2=Q*DN*IEBIC2*HXX/2.

```

```

C
C IEBIC3 IS THE CURRENT COLLECTED FROM THE COARSE REGION BEYOND KOL2
C
C IEBIC3=(4.0*(NGS(NR1,KOL2)+NGS(NR1,NPX))-(NGS(NR2,KOL2)+
$NGS(NR2,NPX)))/(2.0*HZ)
DO 110 N=KOL2,NPX
C IEBIC3=IEBIC3+(2.0*(4.0*NGS(NR1,N)-NGS(NR2,N)))/(2.0*HZ)
CONTINUE
C IEBIC3=IEBIC3*Q*DN*HX/2.
C
C IEBIC IS THE TOTAL JUNCTION CURRENT COLLECTED
C
C IEBIC=IEBIC1+IEBIC2+IEBIC3
C
C IGB IS THE TOTAL GRAIN BOUNDARY CURRENT
C
C IGB=IGB1+IGB2
C
C REC IS THE TOTAL BULK RECOMBINATION CURRENT
C
C REC=RECOMB(KOL1,NZZ,NAME,KOL2,HX,HZ,HXX,HZZ,NPX,NPZ,NXX)
C
C ITOT IS THE TOTAL INPUT GENERATION CURRENT
C
C ITOT IS THE NET INPUT CURRENT I.E. GEN-BULK REC
C
C BULK=Q*REC
C ITOT=Q*2.*GBASE-BULK
C
C CHECKING FOR ACCURACY TO WITHIN 5%
C
C ERROR=ITOT-IEBIC-IGB
C ERRPR= (ERROR/ITOT)*100.
C IF (ABS(ERRPR) .LT. 5.0) GO TO 160
C GO TO 35

```

```

C
C PRINT OUT THE CURRENT VALUES
C THE EBIC CT IS CALCULATED AS THE DIFFERENCE OF
C GEN CT-BULK CT-GB CT
C
160 IEBIC=ITOT-IGB
IF (SNON(5) .EQ. 0) SNON(5) = S
WRITE (6,209) X0,IEBIC,IGB,BULK,SNON(5)
C
C GO TO THE NEXT GRID SPACING AND RECALCULATE THE CURRENTS
C
X0=X0-2*HX0
IF (X0 .LE. 3.0E-4) GO TO 250
GO TO 25
FORMAT (2I3)
200 FORMAT (2F6.0,4E7.0)
201 FORMAT (4E7.0)
203 FORMAT (/,'1',25X,'EBIC RESPONSE OF A PN JUNCTION -',1X,
$'GAUSSIAN SOURCE MODEL',/)
204 FORMAT (/11X,'BEAM ENERGY IN KEV=',F6.0,5X,'# OF E-H PAIRS',
$,1X,'GENERATED/SEC=',E10.3/)
205 FORMAT (11X,'RDD=',E10.3,5X,'DIFF LENGTH IN CM=',E12.3,5X,
$'GB REC VEL IN CM/SEC=',E12.3/)
206 FORMAT (/30X,'*** GB RECOMBINATION VELOCITY IS ',
$'NONLINEAR ***',/)
207 FORMAT (/11X,'NSTD=',E10.3,3X,'NSTA=',E10.3,3X,'CN=',
$,E10.3,3X,'CI=',E10.3)
208 FORMAT (/10X,'DIST FROM GB IN CM',10X,'EBIC CT IN AMPS',10X,
$'GB CT IN AMPS',10X,'BULKREC CT IN AMPS',5X,'MIN VEL CM/S',/)
209 FORMAT (/12X,F11.6,14X,E15.7,9X,E15.7,10X,E15.7,5X,E15.7)
210 FORMAT (/,'1',25X,'EBIC RESPONSE OF A PN JUNCTION -',1X,
$'SPHERICAL SOURCE MODEL',/)
250 STOP
END
FUNCTION SEIDL(A,B,C,D,PHI1,PHI2,PHI3,PHI4,BETA,GAMMA,OLD)
C

```

C THIS FUNCTION SUBPROGRAM CALCULATES THE N VALUES AND THEN OVER
 C RELAXES IT
 C

```

REAL LN
COMMON DN, LN
W=1.9
GS=((A*PHI1+B*PHI2+C*PHI3+D*PHI4)+(BETA*GAMMA/DN))/
  $ (PHI1+PHI2+PHI3+PHI4+(BETA/(LN**2)))
SEIDEL = W*GS+(1.-W)*OLD
RETURN
END
SUBROUTINE GUSVOL(ZO,HZZ,NZZ,HXX,NXX,GVOL,G,KOL1,NAME,
  $HX,XO,KOL2,NPX,HZ,KOLA,XJ,GBASE)

```

C THIS SUBROUTINE CALCULATES THE FACTOR BY WHICH THE INTEGRATED
 C # OF E-H PAIRS OVER THE GRID POINTS DIFFERS FROM THE ACTUAL
 C VALUE GVOL AND CREATES THE MATRIX SUCH THAT GVOL=CONSTANT
 C

```

DIMENSION G(15,201),VAL(25,201)

```

```

PI = 3.141
NA = 1
SUM3 = 0.0
SUM6 = 0.0
SUM9 = 0.0
SUM12 = 0.0
KOL11 = KOL1-1
KOL22 = KOL2+1
NAME1 = NAME+1
KOL12 = KOL1+1
NPX1 = NPX-1
INDEX=(NXX-1)/4

```

C INITIALIZE THE MATRICES TO BE ZERO

```

DO 5 NYU=1,NZZ
DO 5 NYV=1,NPX

```

C
 C
 C

1

```

5 VAL(NYU,NYV)=0.0
6 G(NYU,NYV)=0.0
7 CONTINUE
8
9 A IS THE PRE-EXPONENTIAL COEFFICIENT AND IS GIVEN BY THE
10 GRUEN'S FUNCTION
11
12 NXX2 = ((NXX-1)/2)+1
13 ZETA = ((NA-1)*HZZ*XJ)/ZO
14 IF (ZETA .GT. 1.1) GO TO 20
15 A = (GVOL/ZO)*(0.6+6.21*ZETA-12.4*(ZETA**2)+5.69*(ZETA**3))
16 SIG2 = (0.11*((NA-1)*HZZ*XJ)**3)/ZO+0.36*((1.0E-5)**2)
17
18 FIT A RADIAL GAUSSIAN DISTRIBUTION TO THE MATRIX VAL
19 THE INTEGRAL IS EVALUATED FROM X0 TO INFINITY BY TAKING
20 FINE MESH POINTS NEAR X0 (I.E.UPTO X0-2HX) AND COARSE
21 POINTS BEYOND
22 VAL IS AN INTERMEDIATE MATRIX WHICH FINALLY IS USED TO CREATE
23 THE MATRIX G
24
25 DO 10 NB=1,NXX2
26 DUMMY = (((NB-1)*HXX)**2)/(2*SIG2)
27 IF (DUMMY .GT. 60) GO TO 10
28 VAL(NA,NB) = ((2.0*A)/(SQRT(PI*2.0*SIG2)))*EXP(-DUMMY)
29 CONTINUE
30 NA = NA+1
31 GO TO 7
32
33 NA1 = NA-1
34 NA2 = NA1-1
35 DO 26 NC=1,NZZ,NAME
36 ZETA = ((NC-1)*HZZ*XJ)/ZO
37 A = (GVOL/ZO)*(0.6+6.21*ZETA-12.4*(ZETA**2)+5.69*(ZETA**3))
38 SIG2 = (0.11*((NC-1)*HZZ*XJ)**3)/ZO+0.36*((1.0E-5)**2)
39 DO 25 ND=KOL22,NPX
40 DUMMY = ((2+ND-KOL2)*HX)**2/(2*SIG2)
41 IF (DUMMY .GT. 60) GO TO 25

```

```

25 VAL(NC,ND) = ((2.0*A)/(SQRT(PI*2.*SIG2)))*EXP(-DUMMY)
26 CONTINUE
27 CONTINUE
28 C
29 C INTEGRATE OVER THE GRID POINTS AND EQUATE THE VALUE OF THIS
30 C INTEGRAL TO THE TOTAL VOLUME GENERATION RATE
31 C USE TRAPEZOIDAL RULE TO INTEGRATE
32 C FIRST INTEGRATE OVER THE FINE MESH POINTS
33 C
34 SUM1 = (VAL(1,1)+VAL(1,NXX2))*HXX/2.
35 SUM2 = (VAL(NA1,1)+VAL(NA1,NXX2))*HXX/2.
36 NXX1 = NXX2-1
37 DO 30 NE=2,NXX1
38 SUM1 = SUM1+(2.0*(HXX/2.)*VAL(1,NE))
39 SUM2 = SUM2+(2.0*(HXX/2.)*VAL(NA1,NE))
40 CONTINUE
41 DO 40 NF=2,NA2
42 SUM3 = SUM3+(HXX/2.)*(VAL(NF,1)+VAL(NF,NXX2))
43 DO 40 NG=2,NXX1
44 SUM3 = SUM3+(2.0*(HXX/2.)*VAL(NF,NG))
45 CONTINUE
46 SUM = (SUM1+SUM2+2.0*SUM3)*HZZ/2.
47 C
48 C NOW INTEGRATE OVER THE COARSE MESH POINTS
49 C
50 SUM4 = (VAL(1,NXX2)+VAL(1,NPX))*HX/2.
51 SUM5 = (VAL(NA1,NXX2)+VAL(NA1,NPX))*HX/2.
52 DO 43 NFF=KOL22,NPX1
53 SUM4 = SUM4+(2.0*(HX/2.)*VAL(1,NFF))
54 SUM5 = SUM5+(2.0*(HX/2.)*VAL(NA1,NFF))
55 CONTINUE
56 DO 45 NGG=NAME1,NA2,NAME
57 SUM6 = SUM6+(HX/2.)*(VAL(NGG,NXX2)+VAL(NGG,NPX))
58 DO 45 NFG=KOL22,NPX1
59 SUM6 = SUM6+(2.0*(HX/2.)*VAL(NGG,NFG))
60 CONTINUE
61
62
63
64
65

```

```

C      SUM=SUM+(SUM4+SUM5+2.0*SUM6)*HZ/2.
C      GBASE IS THE TOTAL GENERATION IN THE BASE REGION
C      ZETAJ=XJ/ZO
C      GBASE=GVOL-(GVOL)*(0.6*ZETAJ+6.21*((ZETAJ**2)/2)-12.4*
C      $((ZETAJ**3)/3)+5.69*((ZETAJ**4)/4))
C      FACT IS THE FACTOR BY WHICH THE TOTAL GENERATED # OF
C      E-H PAIRS DIFFERS FROM THAT CALCULATED ABOVE
C      FACT = GBASE/SUM
C      GENERATE THE MATRIX G BY MULTIPLYING VAL BY FACT
C      IDUM=KOL1+NX*2
C      IF (KOLA .LT. 1) IDUM=KOL1+INDEX+1
C      DO 50 NH=1,NZZ
C      DO 50 NI=1,NXX2
C      G(NH,IDUM+NI-2)=VAL(NH,NI)*FACT
C      IF (IDUM-NI)49,49,48
C      G(NH,IDUM-NI) = VAL(NH,NI)*FACT
C      GO TO 50
C      ITER=IABS(IDUM-NI-2)
C      G(NH,ITER)=VAL(NH,NI)*FACT+G(NH,ITER)
C      CONTINUE
C      DO 80 NQ=1,NZZ,NAME
C      ITER=KOL1
C      ITE=KOL1
C      DO 80 NS=KOL22,NPX
C      G(NQ,NS)=FACT*VAL(NQ,NS)
C      ITER=ITER-1
C      IF (ITER)60,60,70
C      ITE1=IABS(ITER-2)
C      IF (ITE1 .LE. KOL1)GO TO 63
C      IF (ITE1 .GT. KOL1 .AND. ITE .LE. KOL2) INC=INDEX

```

48

49

50

60

```

IF (ITE .GE. KOL2) INC=1
ITE=ITE+INC
GO TO 65
IIE=ITE1
G(NQ,ITE)=FACT*VAL(NQ,NS)+G(NQ,ITE)
GO TO 80
G(NQ,ITER)=FACT*VAL(NQ,NS)
CONTINUE
RETURN
END
FUNCTION RECOMB(KOL1,NZZ,NAME,KOL2,HX,HZ,HXX,HZZ,NPX,NPZ,
$NXX)
C
C THIS FUNCTION SUBPROGRAM CALCULATES THE TOTAL BULK RECOMBINATION
C
COMMON DN,LN,NGS
REAL NGS(150,201),LN
C
C SETUP PARAMETERS
C
KOL11=KOL1-1
NAME1=NAME+1
NZZ1=NZZ-1
TAU=(LN**2)/DN
KOL21=KOL2-1
KOL12=KOL1+1
KOL22=KOL2+1
NPX1=NPX-1
NZZ2=NZZ+1
INDEX=(NXX-1)/4
KOL1=KOL1+INDEX
NPZ1=NPZ-1
R3=0.0
R6=0.0
R9=0.0
R12=0.0

```

```

C
C
C
    REC1 IS THE RECOMBINATION FROM 1 TO KOL11
    IF (KOL11 .LE. 0) GO TO 22
    R1=(NGS(1,1)+NGS(1,KOL1))*HX/2.
    R2=(NGS(NZZ,1)+NGS(NZZ,KOL1))*HX/2.
    IF (KOL11 .EQ. 1) GO TO 25
    DO 10 I1=2,KOL11
    R1=R1+2.0*(HX/2.)*NGS(1,I1)
    R2=R2+2.0*(HX/2.)*NGS(NZZ,I1)
    CONTINUE
    DO 20 I2=NAME1,NZZ1,NAME
    R3=R3+(HX/2.)*(NGS(I2,1)+NGS(I2,KOL1))
    DO 20 I3=2,KOL11
    R3=R3+2.0*(HX/2.)*NGS(I2,I3)
    CONTINUE
    REC1=(R1+R2+2.0*R3)*(HZ/2.)*(1./TAU)
    GO TO 25
    REC1=0.0
    20
    22
    C
    C
    REC2 IS THE RECOMBINATION IN THE FINE MESH REGION
    25
    R4=(NGS(1,KOL1)+NGS(1,KOL2))*HXX/2.
    R5=(NGS(NZZ,KOL1)+NGS(NZZ,KOL2))*HXX/2.
    DO 30 I4=KOL12,KOL21
    R4=R4+2.0*(HXX/2.)*NGS(1,I4)
    R5=R5+2.0*(HXX/2.)*NGS(NZZ,I4)
    CONTINUE
    DO 40 I5=2,NZZ1
    R6=R6+(NGS(I5,KOL1)+NGS(I5,KOL2))*HXX/2.
    DO 40 I6=KOL12,KOL21
    R6=R6+2.0*(HXX/2.)*NGS(I5,I6)
    CONTINUE
    REC2=(R4+R5+2.0*R6)*(HZZ/2.)*(1/TAU)
    30
    40
    C
    C
    REC3 IS THE RECOMBINATION RATE IN THE REGION BETWEEN KOL2 AND NPX

```

```

C
R7=(NGS(1,KOL2)+NGS(1,NPX))*HX/2.
R8=(NGS(NZZ,KOL2)+NGS(NZZ,NPX))*HX/2.
DO 50 I6=KOL2,NPX1
R7=R7+2.0*(HX/2.)*NGS(1,I6)
R8=R8+2.0*(HX/2.)*NGS(NZZ,I6)
CONTINUE
50
DO 60 I7=NAME1,NZZ1,NAME
R9=R9+(NGS(I7,KOL2)+NGS(I7,NPX))*HX/2.
DO 60 I8=KOL2,NPX1
R9=R9+2.0*(HX/2.)*NGS(I7,I8)
CONTINUE
60
REC3=(R7+R8+2.0*R9)*(HZ/2.)*(1./TAU)
C
REC4 IS THE RECOMBINATION BEYOND 1.120
C
R10=(NGS(NZZ,1)+NGS(NZZ,NPX))*HX/2.
R11=(NGS(NPZ,1)+NGS(NPZ,NPX))*HX/2.
IF (KOL1.LE.0)GO TO 75
DO 70 J1=2,KOL1
R10=R10+2.0*(HX/2.)*NGS(NZZ,J1)
R11=R11+2.0*(HX/2.)*NGS(NPZ,J1)
CONTINUE
70
DO 80 J2=KOL1,KOL2,INDEX
R10=R10+2.0*(HX/2.)*NGS(NZZ,J2)
R11=R11+2.0*(HX/2.)*NGS(NPZ,J2)
CONTINUE
80
DO 90 J3=KOL2,NPX1
R10=R10+2.0*(HX/2.)*NGS(NZZ,J3)
R11=R11+2.0*(HX/2.)*NGS(NPZ,J3)
CONTINUE
90
DO 120 J4=NZZ2,NPZ1
R12=R12+(NGS(J4,1)+NGS(J4,NPX))*HX/2.
IF (KOL1.LE.0)GO TO 105
DO 100 J5=2,KOL1
R12=R12+2.0*(HX/2.)*NGS(J4,J5)

```

```

100 CONTINUE
105 DO 110 J6=KOLI,KOL2,INDEX
    R12=R12+2.0*(HX/2.)*NGS(J4,J6)
    CONTINUE
110 DO 120 J7=KOL2,NPX1
    R12=R12+2.0*(HX/2.)*NGS(J4,J7)
    CONTINUE
120 REC4=(R10+R11+2.0*R12)*(HZ/2.)*(1./TAU)
C
C RECOMB IS THE TOTAL BULK RECOMBINATION
C
C RECOMB=REC1+REC2+REC3+REC4
C RETURN
C END
C SUBROUTINE GAUSS(NPX,NPZ,NZZ,HZZ,HXX,HZ,S,HX,KOL1,
$KOL2,EPS,Z0,NZ,NX,G,NXX,SNON,IVEL,NDD,NSTD,NSTA,CN,CI)
C
C THIS SUBROUTINE SOLVES THE DIFFERENTIAL EQUATION BY A FINITE
C DIFFERENCE APPROXIMATION;THE RESULTING SIMULTANEOUS EQUATION IS
C SOLVED BY GAUSS SEIDEL ELIMINATION METHOD WITH OVERRELAXATION
C THE ARRAY SNON IS USED ONLY WHEN SGB IS NONLINEAR AND CONTAINS
C THE VALUES OF SGB ALONG THE GRAIN BOUNDARY; THE ALGORITHM IN THIS
C SUBROUTINE IS SUCH THAT WHEN IVEL=0 SGB IS TAKEN TO BE A CONSTANT
C AND WHEN IVEL=1 SGB IS NONLINEAR
C
C REAL NGS(150,201),NOLD(150,201),LN,NDD,NI,G(15,201)
$ ,NSTD,NSTA
C DIMENSION SNON(150)
C COMMON DN,LN,NGS
C
C SET UP PARAMETERS
C SKL IS THE UPPER LIMIT FOR THE VELOCITY AT THE GRAIN
C BOUNDARY AND COULD BE SET TO ANY VALUE DEPENDING ON THE
C CONDITIONS AT THE GB-PASSIVATED OR UNPASSIVATED
C
C SKL=5.0E06

```

```

NI=1.33E10
KOL11 = KOL1-1
KOL12 = KOL1+1
KOL22 = KOL2+1
KOL21 = KOL2-1
INDEX = (NXX-1)/4
NPX1 = NPX-1
NPZ1 = NPZ-1
NZZ1 = NZZ-1
NZZ2 = NZZ+1
HX2 = (HXX**2)
HXX2 = (HXX**2)
RATIO1 = (HX/HZ)**2
RATIO2 = (HXX/HZZ)**2
RATIO3 = (HXX/HX)
RATIO4 = HXX2/(HZZ*HZ)
IROW=INT((HZ/HZZ)+0.1)
IFLAG = 0
HXA=HX
KOP=3
DW=0.5E-4
IF (KOL11 .EQ. 1) KOP=2+INDEX
IF (KOL11 .LE. 0) HXA=HXX

C
C IF SGB IS NONLINEAR THEN CALCULATE THE PREEXPONENTIAL
C COEFFICIENT SO FOR GIVEN NSTD AND NSTA
C
MUL1=1
MUL2=1
IF (IVEL .EQ. 0) GO TO 5
DEN1=(((NDD/1.0E15)**ALOG10(2.))**SQRT(5.E10))
DEN2=(((1.0E15/NDD)**ALOG10(2.))**SQRT(1./5E10))
MUL1=0
IF (NSTD .NE. 0) GO TO 1
DEND=1.0
GO TO 2

```

```

1  DEND=(CN*DEN1/SQRT(NSTD)) + (CI*DEN2*SQRT(NSTD))
2  IF (NSTA .NE. 0) GO TO 3
   MUL2=0
   DENA=1.0
   GO TO 4
3  DENA=(CI*DEN1/SQRT(NSTA)) + (CN*DEN2*SQRT(NSTA))
4  SO=(CN*CI*SQRT(NDD/NI)/2.)*((MUL1*NSTD/DEND) +
   $ (MUL2*NSTA/DENA))
C
C  REWRITE THE CURRENT VALUES OF NGS INTO ANOTHER ARRAY FOR
C  COMPARISON
C
5  DO 10 I=1,NPZ
   DO 10 J=1,NPX
   NOLD(I,J)=NGS(I,J)
   CONTINUE
10
C
C  SOLVE FIRST IN THE REGION BETWEEN 0 AND 1.120 IN THE Z DIRECTION
C  FROM 1 TO K01 IN THE X DIRECTION
C
   DO 50 K=2,NZZ1
C
C  CHECKING IF THE PINE MESH SIZE IS AT THE GRAIN BOUNDARY
   FLG = (K-1)*HZZ/HZ
   IFLG = INT(FLG)
   IF ((FLG-IFLG) .GT. 1.E-4) IFLAG=1
   IF (K011 .LE. 0) GO TO 15
   IF (IFLAG .EQ. 1) GO TO 25
C
C  BOUNDARY CONDITION AT THE GRAIN BOUNDARY
   IF (LEVEL .EQ. 0) GO TO 19
   IF (NGS(K,1) .LE. 0) GO TO 17
   S=SQ*SQRT(NI)/(NGS(K,1)/2.)
   IF (S .GT. SKL) S=SKL
15

```

```

17 GO TO 18
18 S=SKL
19 SNOW(K,1)=(-NGS(K,KOP)+4.*NGS(K,2)+4.*HXA*DW*G(K,1)/DN)
$/((S/DN)*2.*HXA+3.0)
IF (KOL1.EQ. 1) GO TO 25
IF (KOL1.LE. 0) GO TO 27
DO 20 L=2,KOL1
C
C SEIDEL IS THE FUNCTION WHICH SOLVES FINITE DIFFERENCE EQUATION
C AND THEN OVERRELAXES IT
C
NGS(K,L)=SEIDEL(NGS(K,L+1),NGS(K,L-1),NGS(K-IROW,L),
$NGS(K+IROW,L),1.,1.,RATIO1,RATIO1,HX2,G(K,L),NOLD(K,L))
CONTINUE
20
C
C CALCULATE THE N VALUES IN THE FINE MESH REGION
C
25 NGS(K,KOL1)=SEIDEL(NGS(K,KOL1+1),NGS(K,KOL1-1),NGS(K-1,KOL1),
$NGS(K+1,KOL1),1.,RATIO3,RATIO2,RATIO2,HXX2,G(K,KOL1),
$NOLD(K,KOL1))
DO 30 LL=KOL12,KOL21
NGS(K,LL)=SEIDEL(NGS(K,LL+1),NGS(K,LL-1),NGS(K-1,LL),
$NGS(K+1,LL),1.,1.,RATIO2,RATIO2,HXX2,G(K,LL),
$NOLD(K,LL))
CONTINUE
30
C
C CALCULATE THE N VALUES BEYOND KOL2
C
NGS(K,KOL2)=SEIDEL(NGS(K,KOL2+1),NGS(K,KOL2-1),NGS(K-1,KOL2),
$NGS(K+1,KOL2),RATIO3,1.,RATIO2,RATIO2,HXX2,G(K,KOL2),
$NOLD(K,KOL2))
IF (IFLAG.EQ. 1) GO TO 45
DO 40 MM=KOL22,NPX1
NGS(K,MM)=SEIDEL(NGS(K,MM+1),NGS(K,MM-1),NGS(K-IROW,MM),
$NGS(K+IROW,MM),1.,1.,RATIO1,RATIO1,HX2,G(K,MM),NOLD(K,MM))

```

```

40 CONTINUE
45 IFLAG = 0
50 CONTINUE
C
C
C CALCULATE ALONG THE ROW NZZ (Z=1..1*Z0)
C
IF (IVEL.EQ. 0) GO TO 58
IF (NGS(NZZ, 1) - LE. 0) GO TO 56
S=SQ*SQRT(NI/(NGS(NZZ, 1)/2.))
IF (S.GT. SKL) S=SKL
GO TO 57
S=SKL
56 SNOW(NZZ)=S
57 NGS(NZZ, 1) = (-NGS(NZZ, KOP) + 4.*NGS(NZZ, 2) + 4.*HXA*DW*G(NZZ, 1)
58 $/DN)/(S/DN)*2.*HXA+3.)
IF (KOL11.EQ. 1) GO TO 63
IF (KOL11.LE. 0) GO TO 65
DO 60 N=2, KOL11
NGS(NZZ, N) = SEIDEL(NGS(NZZ, N+1), NGS(NZZ, N-1), NGS(NZZ-I*ROW, N),
$NGS(NZZ+1, N), 1., 1., RATIO1, RATIO1, HX2, G(NZZ, N), NOLD(NZZ, N))
CONTINUE
60
63 NGS(NZZ, KOL1) = SEIDEL(NGS(NZZ, KOL1+1), NGS(NZZ, KOL1-1),
$NGS(NZZ-1, KOL1), NGS(NZZ+1, KOL1), 1., RATIO3, RATIO2, RATIO4,
$HXX2, G(NZZ, KOL1), NOLD(NZZ, KOL1))
DO 70 NN=KOL12, KOL21
NGS(NZZ, NN) = SEIDEL(NGS(NZZ, NN+1), NGS(NZZ, NN-1), NGS(NZZ+1, NN
$), NGS(NZZ-1, NN), 1., 1., RATIO4, RATIO2, HXX2, G(NZZ, NN),
$NOLD(NZZ, NN))
CONTINUE
70
NGS(NZZ, KOL2) = SEIDEL(NGS(NZZ, KOL2+1), NGS(NZZ, KOL2-1),
$NGS(NZZ-1, KOL2), NGS(NZZ+1, KOL2), RATIO3, 1., RATIO2, RATIO4,
$HXX2, G(NZZ, KOL2), NOLD(NZZ, KOL2))
DO 80 NNN=KOL22, NPX1
NGS(NZZ, NNN) = SEIDEL(NGS(NZZ, NNN+1), NGS(NZZ, NNN-1), NGS(NZZ
$I*FOW, NNN), NGS(NZZ+1, NNN), 1., 1., RATIO1, RATIO1, HX2,
$G(NZZ, NNN), NOLD(NZZ, NNN))

```

```

80 CONTINUE
C SOLVE IN THE REGION BEYOND NZZ1
C
C DO 120 MN=NZZ2,NPZ1
  IF (KOL1 .LE. 0) GO TO 103
  IF (IVEL .EQ. 0) GO TO 95
  IF (NGS(MN,1) .LE. 0) GO TO 90
  S=S0*SQRT(NI/(NGS(MN,1)/2.))
  IF (S .GT. SKL) S=SKL
  GO TO 93
90 S=SKL
93 SNGN(MN)=S
95 NGS(MN,1)=(-NGS(MN,KOP)+4.*NGS(MN,2))/((S/DN)*2.*HXA*3.)
  IF (KOL1 .EQ. 1) GO TO 101
  DO 100 NM=2,KOL1
    NGS(MN,NM)=SEIDEL(NGS(MN,NM+1),NGS(MN,NM-1),NGS(MN-1,NM),
    $NGS(MN+1,NM),1.,1.,RATIO1,HX2,0.0,NOLD(MN,NM))
    CONTINUE
  IJ1=KOL1
  GO TO 109
100 IJ1=KOL1+INDEX
  IF (IVEL .EQ. 0) GO TO 108
  IF (NGS(MN,1) .LE. 0) GO TO 106
  S=S0*SQRT(NI/(NGS(MN,1)/2.))
  IF (S .GT. SKL) S=SKL
  GO TO 107
106 S=SKL
107 SNGN(MN)=S
108 NGS(MN,1)=(-NGS(MN,KOL1+2*INDEX)+4.*NGS(MN,KOL1+INDEX))/
  $((S/DN)*2.*HX+3.)
109 DO 110 IJ=IJ1,KOL2,INDEX
  ICCL1 = INDEX
  ICCL2 = INDEX
  IF (IJ .EQ. KOL1) ICOL1=1
  IF (IJ .EQ. KOL2) ICOL2=1

```

```

110      NGS(MN, IJ) = SEIDEL(NGS(MN, IJ + ICOL2), NGS(MN, IJ - ICOL1), NGS(MN - 1, IJ),
      $ NGS(MN + 1, IJ), 1., 1., RATIO1, RATIO1, HX2, 0.0, NOLD(MN, IJ))
      CONTINUE
      DO 120 IK = KOL22, NPX1
      NGS(MN, IK) = SEIDEL(NGS(MN, IK + 1), NGS(MN, IK - 1), NGS(MN - 1, IK),
      $ NGS(MN + 1, IK), 1., 1., RATIO1, RATIO1, HX2, 0.0, NOLD(MN, IK))
      CONTINUE
120      CHECK FOR CONVERGENCE
      C
      C
      DO 140 MA = 2, NPZ1
      DO 140 MB = 2, NPX1
      ERR = NOLD(MA, MB) - NGS(MA, MB)
      VAL = EPS * NOLD(MA, MB)
      IF (ABS(ERR) .GT. VAL) GO TO 150
      CONTINUE
      GO TO 220
140      C
      C
      C IF THERE IS NO CONVERGENCE THEN REPEAT CALCULATIONS
      C SETUP ARRAY VALUES ALONG KOL11, KOL22, NZZ2
      C THE VALUES ALONG KOL11, KOL22 ARE OBTAINED BY TAKING THE AVERAGE
      C OF THE ARRAY VALUES ABOVE AND BELOW IT
      DO 160 NAA = 3, NZZ1, 4
      IF (KOL11 .LE. 0) GO TO 155
      NGS(NA, KOL11) = (NGS(NA - 2, KOL11) + NGS(NA + 2, KOL11)) / 2.
      NGS(HA, KOL22) = (NGS(HA - 2, KOL22) + NGS(HA + 2, KOL22)) / 2.
      CONTINUE
155      DO 165 NAB = 2, NZZ1, 4
      IF (KOL11 .LE. 0) GO TO 163
      NGS(NAA, KOL11) = (NGS(NAA - 1, KOL11) + NGS(NAA + 1, KOL11)) / 2.
      NGS(NAA, KOL22) = (NGS(NAA - 1, KOL22) + NGS(NAA + 1, KOL22)) / 2.
      CONTINUE
163      DO 167 NAB = 4, NZZ1, 4
      IF (KOL11 .LE. 0) GO TO 166
      NGS(NAB, KOL11) = (NGS(NAB - 1, KOL11) + NGS(NAB + 1, KOL11)) / 2.
165

```

```

166   NGS(NAB,KOL22) = (NGS(NAB-1,KOL22) + NGS(NAB+1,KOL22)) / 2.
167   CONTINUE
C
C   THE VALUES ALONG THE ROW NZZ1 ARE OBTAINED BY A WEIGHTED AVERAGE
C   SCHEME
C
      KOL3=KOL1+INDEX
      KOL4=KOL3-1
      KOL5=KOL3+1
      KOL6=KOL3+INDEX
      KOL7=KOL6-1
      KOL8=KOL6+1
      KOL9=KOL6+INDEX
      KOL15=KOL9-1
      KOL16=KOL9+1
      NORM1=0
      NORM2=0
      NORM3=0
      NORM4=0
      DO 190 NE=KOL12,KOL4
      NORM1=NORM1+1
      NGS(NZZ2,NE) = (FLOAT(INDEX-NORM1)/INDEX) * NGS(NZZ2,KOL1) +
      $ (FLOAT(NORM1)/INDEX) * NGS(NZZ2,KOL3)
      CONTINUE
190
      DO 192 NE=KOL5,KOL7
      NORM3=NORM3+1
      NGS(NZZ2,NE) = (FLOAT(INDEX-NORM3)/INDEX) * NGS(NZZ2,KOL3) +
      $ (FLOAT(NORM3)/INDEX) * NGS(NZZ2,KOL6)
      CONTINUE
192
      DO 194 NFF=KOL8,KOL15
      NORM4=NORM4+1
      NGS(NZZ2,NFF) = (FLOAT(INDEX-NORM4)/INDEX) * NGS(NZZ2,KOL6) +
      $ (FLOAT(NORM4)/INDEX) * NGS(NZZ2,KOL9)
      CONTINUE
194
      DO 200 NF=KOL16,KOL21
      NORM2=NORM2+1

```

```

200      NGS(NZZ2,NP)= (FLOAT(INDEX-NORM2)/INDEX) *NGS(NZZ2,KOL9) +
      $(FLOAT(NORM2)/INDEX)*NGS(NZZ2,KOL2)
      CONTINUE
      GO TO 5
220      IF (IVEL .EQ. 0) GO TO 250
      C
      C
      C      CALCULATE THE LATEST VALUES OF SGB
      IROW1=IROW+1
      DO 225 NAK=IROW1,NZZ,IROW
      SNON(NAK)=S0*SQRT(NI/(NGS(NAK,1)/2.))
      IF (SNON(NAK) .GT. SKL) SNON(NAK)=SKL
      CONTINUE
225      DO 227 NAL=NZZ,NPZ1
      SNON(NAL)=S0*SQRT(NI/(NGS(NAL,1)/2.))
      IF (SNON(NAL) .GT. SKL) SNON(NAL)=SKL
      CONTINUE
227      SNON(1)=SKL
      SNON(NPZ)=SKL
250      RETURN
      END
      SUBROUTINE SPHGEN(NZZ,KOL1,KOL2,HXX,X0,HZZ,Z0,RGV,
      $GVCL,G,GEASE,NPY,HX)
      DIMENSION VAL(25,201),G(15,201)
      C
      C      THIS SUBROUTINE CALCULATES THE MATRIX G TO BE USED
      C      IN THE CONTINUITY EQUATION AT EACH GRID POINT; THE
      C      SOURCE IS ASSUMED TO BE A CIRCLE WITH CONSTANT GENERATION
      C      RATE; TO CALL THIS SET IGEN=1
      KOL12=KOL1+1
      KOL21=KOL2-1
      NZZ1=NZZ-1
      SUM3=0.0
      CUP= ((KOL1-1) *HX-X0)
      C

```



```
FACT=2.*GVOL/SUM
C
C GENERATE THE MATRIX G
C
DO 50 NF=1, NZZ
DO 50 NG=1, NPY
G(NF, NG)=FACT*VAL(NF, NG)
CONTINUE
GBASE=GVCL
RETURN
END
```

50

C
C
C

APPENDIX D POLYSILICON CELL FABRICATION

We describe below the processing steps involved in the fabrication of the large- and small-area polysilicon cells used in bulk and thin-film aluminum diffusion studies (see Chapter 4). The standard cell cleaning procedure, which was common to all the processes, is described first. The photolithographic process (D.3) was used in the fabrication of the small-area cells.

D.1 Standard Cleaning Process

1. Degrease the wafers by scrubbing them with cotton swabs dipped in hot trichlorethylene (TCE).
2. Immerse the wafers in boiling TCE for five minutes.
3. Immerse in a second solution of boiling TCE for five minutes.
4. Immerse in boiling acetone for five minutes.
5. Immerse in boiling methanol for five minutes.
6. Rinse in deionized (DI) water for ten minutes.

D.2 Bulk Process (Large-Area Cells)

1. Clean the wafers using the standard process.
2. Polish using 2:15:5 (HF:HNO₃:CH₃COOH) Si-etch solution for 10-20 minutes.

3. Clean using a proxy solution; immerse the wafers in a solution of $\text{H}_2\text{SO}_4 + \text{H}_2\text{O}_2$ (3:1) for about 10 minutes, then dip in HF for about 10 seconds.
4. Predeposit phosphorous (n^+) at 875°C for 30 minutes.
5. Lap the back surface.
6. Evaporate 1.5- μm -thick aluminum onto the back surface.
7. Anneal at 800°C for one hour in the presence of forming gas.
8. Remove the phosphorous glass from the front surface using buffered-oxide-etch (BOE) solution.
9. Evaporate about 6000 Å of aluminum onto the back surface.
10. Sinter, if necessary, at 450°C for 15 minutes in forming gas.
11. Etch edge using 6:1:1 ($\text{HNO}_3:\text{HF}:\text{CH}_3\text{COOH}$) Si-etch solution.
12. Evaporate aluminum onto the front surface (~ 300-Å-thick).

D.3 Photolithography

1. Bake the wafers at 300°C for 30 minutes.
2. Spin on negative photoresist.
3. Prebake the wafers at 65°C for about 20 minutes.
4. Expose, using the appropriate mask, for about 15 seconds.
5. Develop the wafers using the negative-resist developer for about 20 seconds.
6. Postbake the wafers at 135°C for about 20 minutes.

D.4 Bulk Process (Small-Area Cells)

1. Clean the wafers using the standard process.
2. Polish using 2:15:5 Si-etch solution.
3. Clean using proxy solution.

4. Grow a thermal oxide about 5000-Å-thick at 1100°C: 10 minutes dry O₂, 22 minutes wet O₂, and 10 minutes dry O₂.
5. Open windows for the n⁺ diffusion using the photolithography process (1st mask).
 6. Etch off the oxide in the windows using BOE solution.
 7. Remove photoresist using proxy solution (~ 8 min).
 8. Clean using proxy solution.
 9. Predeposit phosphorous at 950°C for 40 minutes.
 10. Clean using proxy solution.
 11. Drive the emitter in at 1000°C for 27 minutes: 10 minutes dry O₂, 12 minutes wet O₂, 5 minutes dry O₂.
 12. Lap the back surface.
 13. Evaporate about 1.5 μm-thick aluminum onto the back surface.
 14. Anneal at 800°C for one hour in forming gas.
 15. Open windows for the front contacts using the photolithography process (2nd mask).
 16. Etch off the oxide in the windows using BOE solution.
 17. Remove photoresist using proxy solution (~ 8 min.)
 18. Clean using proxy solution.
 19. Evaporate aluminum onto the front surface (~ 5000-Å-thick).
 20. Define the front metallization pattern using the photolithography process.
 21. Remove aluminum using aluminum etch.
 22. Remove photoresist using plasma etch.
 23. Evaporate aluminum onto the back surface (~ 6000-Å-thick).
 24. Sinter, if necessary, at 450°C for 15 minutes in forming gas.

D.5 Thin-Film Process (Large-Area Cells)

1. Clean the wafers using the standard process.
2. Polish using 2:15:5 Si-etch solution.
3. Clean using proxy solution.
4. Evaporate 1.5 μm of aluminum onto the front surface.
5. Anneal at 450°C for 3-6 hours in forming gas.
6. Remove aluminum using aluminum etch.
7. Etch the front surface (0-2 μm) using 1:2:9 (HF:CH₃COOH:HNO₃) Si-etch solution.
8. Clean using proxy solution.
9. Predeposit phosphorous at 875°C for 30 minutes.
10. Lap the back surface.
11. Evaporate aluminum onto the back surface (~ 6000-Å-thick).
12. Edge etch using 6:1:1 Si-etch solution.
13. Evaporate aluminum onto the front surface (~ 300Å-thick).

REFERENCES

1. L. L. Kazmerski, Polycrystalline and Amorphous Thin Films and Devices, New York: Academic Press, 1980.
2. G. E. Pike and C. H. Seager, "The dc voltage dependence of semiconductor grain-boundary resistance," J. Appl. Phys., vol. 50, pp. 3414-3422, May 1979.
3. T. Shibata, K. F. Lee, J. F. Gibbons, T. J. Magee, J. Peng, and J. D. Hong, "Resistivity reduction in heavily-doped polysilicon using cw-laser and pulsed laser annealing," J. Appl. Phys., vol. 52, pp. 3625-3632, May 1981.
4. N. C.-C. Lu, L. Gerzberg, C.-Y. Lu, and J. D. Meindl, "Modeling and optimization of monolithic polycrystalline silicon resistors," IEEE Trans. Electron Devices, vol. ED-28, pp. 818-830, July 1981.
5. J. G. Fossum and A. Ortiz, "Effects of grain boundaries on the channel conductance of SOI MOSFETs," to be published in IEEE Trans. Electron Devices, vol. ED-30, Aug. 1983.
6. G. Baccarani, B. Ricco, and G. Spadini, "Transport properties of polycrystalline silicon films," J. Appl. Phys., vol. 49, pp. 5565-5570, Nov. 1978.
7. H. C. Card and E. S. Yang, "Electronic processes at the grain boundaries in polycrystalline semiconductors under optical illumination," IEEE Trans. Electron Devices, vol. ED-24, pp. 397-402, Apr. 1977.
8. J. G. Fossum and F. A. Lindholm, "Theory of grain-boundary and intragrain recombination currents in polysilicon p-n-junction solar cells," IEEE Trans. Electron Devices, vol. ED-27, pp. 692-700, Apr. 1980.
9. P. Panayatos and H. C. Card, "Recombination velocity at grain boundaries in polycrystalline Si under optical illumination," IEEE Electron Device Lett., vol. EDL-1, pp. 263-266, Dec. 1980.
10. C. H. Seager, "Grain-boundary recombination: theory and experiment in silicon," J. Appl. Phys., vol. 52, pp. 3960-3968, June 1981.
11. W. Hwang, E. Poon, and H. C. Card, "Carrier recombination at grain boundaries and the effective recombination velocity," Solid-State Electron., vol. 26, pp. 599-603, June 1983.

12. T. L. Chu, S. S. Chu, K. Y. Duh, and H. I. Yoo, "Silicon solar cells on unidirectionally recrystallized metallurgical silicon," IEEE Trans. Electron Devices, vol. ED-24, pp. 442-446, Apr. 1977.
13. C. Lanza and H. J. Hovel, "Efficiency calculations for thin-film polycrystalline semiconductor p-n junction solar cells," IEEE Trans. Electron Devices, vol. ED-27, pp. 2085-2088, Nov. 1980.
14. P. Lester, S. J. Fonash, and S. Ashok, "Performance study of p⁺n and n⁺p solar cell structures on polycrystalline material," in Rec. 14th IEEE Photovoltaic Specialists Conf., IEEE Cat. No. 80CHI508-1, pp. 82-85, 1980.
15. F. N. Gonzalez and A. Neugroschel, "Design of quasi-grain-boundary free (QGBF) polycrystalline solar cell," IEEE Electron Device Lett., vol. EDL-2, pp. 141-143, June 1981.
16. A. Neugroschel and J. A. Mazer, "Effects of grain boundaries on the current-voltage characteristics of polycrystalline silicon solar cells," IEEE Trans. Electron Devices, vol. ED-29, pp. 225-236, Feb. 1982.
17. R. T. Young, M. C. Lu, R. D. Westbrook, and G. E. Jellison, Jr., "Effect of lithium on the electrical properties of grain boundaries in silicon," Appl. Phys. Lett., vol. 38, pp. 628-630, Apr. 1981.
18. C. H. Seager, D. S. Ginley, and J. D. Zook, "Improvement of polycrystalline silicon solar cells with grain-boundary hydrogenation techniques," Appl. Phys. Lett., vol. 30, pp. 831-833, May 1980.
19. N. M. Johnson, D. K. Biegelson, and M. D. Moyer, "Deuterium passivation of grain-boundary dangling bonds in silicon thin films," Appl. Phys. Lett., vol. 40, pp. 882-884, May 1982.
20. C. H. Seager and T. G. Castner, "Zero-bias resistance of grain boundaries in neutron-transmutation-doped polycrystalline silicon," J. Appl. Phys., vol. 49, pp. 3879-3889, July 1978.
21. M. Watanabe, G. Actor, and H. C. Gatos, "Determination of minority-carrier lifetime and surface recombination velocity with high spacial resolution," IEEE Trans. Electron Devices, vol. ED-24, pp. 1172-1177, Sept. 1977.
22. C. H. Seager, "The determination of grain-boundary recombination rates by scanned spot excitation methods," J. Appl. Phys., vol. 53, pp. 5968-5971, Aug. 1982.
23. F. A. Lindholm and J. G. Fossum, "Strategies for the analysis of the effects of grain boundaries on the performance of polysilicon solar cells," in Rec. 15th IEEE Photovoltaic Specialists Conf., IEEE Cat. No. 81CH1644-4, pp. 422-431, 1981.

24. J. Marek, "Evaluation of EBIC images at grain boundaries," in Rec. 16th IEEE Photovoltaic Specialists Conf., IEEE Cat. No. 82CH1821-8, pp. 627-632, 1982.
25. F. Berz and H. K. Kuiken, "Theory of lifetime measurements with the scanning electron microscope: steady state," Solid-State Electron., vol. 19, pp. 437-445, June 1976.
26. J. D. Zook, "Effects of grain boundaries in polycrystalline solar cells," Appl. Phys. Lett., vol. 37, pp. 223-226, July 1980.
27. H. J. Hovel, Semiconductors and Semimetals, vol. 11, New York: Academic Press, 1975.
28. F. M. Roberts and E. L. G. Wilkinson, "The effects of alloying material on regrowth-layer structure in silicon power devices," J. Mat. Sci., vol. 6, pp. 189-199, Mar. 1971.
29. E. Sirtl, "Current aspects of silicon material processing for solar cell application," Semiconductor Silicon, vol. 81-5, pp. 157-161, 1981.
30. F. N. Gonzalez, "Studies of p/n junction polysilicon solar cells," Ph.D. Dissertation, University of Florida, Gainesville, FL, 1982.
31. S. K. Gandhi, The Theory and Practice of Microelectronics, Appendix C, New York: Wiley, 1968.
32. W. Shockley, "A unipolar field effect transistor," Proc. IRE, vol. 40, pp. 1365-1376, Nov. 1952.
33. J. G. Fossum and F. A. Lindholm, "Effects on the open-circuit voltage of grain boundaries within the junction space-charge region of polycrystalline solar cells," IEEE Electron Device Lett., vol. EDL-1, pp. 267-269, Dec. 1980.
34. C. H. Seager and D. S. Ginley, "Fundamental studies of grain-boundary passivation with application to improved photovoltaic devices," in Abstracts of SERI Polycrystalline Silicon Subcontractors' Review Meet., SERI/CP-614-1263, pp. 125-139, June 1981.
35. W. Shockley and W. T. Read, Jr., "Statistics of the recombination of holes and electrons," Phys. Rev., vol. 87, pp. 835-842, Sept. 1952. R. N. Hall, "Electron-hole recombination in germanium," Phys. Rev., vol. 87, p. 387, July 1952.
36. A. G. Milnes, Deep Impurities in Semiconductors, p. 119, New York: Wiley, 1973.
37. Harwell Subroutine Library, Harwell, England.
38. C. H. Seager and G. E. Pike, "Grain boundary states and varistor behavior in silicon bicrystals," Appl. Phys. Lett., vol. 35, pp. 709-711, Nov. 1979.

39. P.-J. Chen, "Determination of electronic parameters of the diffused layer and substrate of p-n junction diodes and solar cells," Ph.D. Dissertation, University of Florida, Gainesville, FL, 1978.
40. J. G. Fossum, R. D. Nasby, and S. C. Pao, "Physics underlying the performance of back-surface field solar cells," IEEE Trans. Electron Devices, vol. ED-27, pp. 785-791, Apr. 1980.
41. C. T. Sah, R. N. Noyce, and W. Shockley, "Carrier generation and recombination in p-n junctions and p-n junction characteristics," Proc. IRE, vol. 45, pp. 1228-1243, Sept. 1957.
42. J. I. Goldstein and H. Yakowitz, Practical Scanning Electron Microscopy, New York: Plenum, 1975.
43. G. E. Possin and C. G. Kirkpatrick, "Electron-beam measurements of minority-carrier lifetime distributions in ion-beam-damaged silicon," J. Appl. Phys., vol. 50, pp. 4033-4041, June 1979.
44. W. H. Hackett, Jr., "Direct measurement of very short minority-carrier diffusion lengths in semiconductors," J. Appl. Phys., vol. 42, pp. 3249-3251, July 1971.
45. H. K. Kuiken, "Theory of lifetime measurements with the scanning electron microscope: transient analysis," Solid-State Electron., vol. 19, pp. 447-450, June 1976.
46. G. E. Possin and C. G. Kirkpatrick, "Recombination in heavily doped planar diodes," J. Appl. Phys., vol. 50, pp. 3478-3483, May 1979.
47. D. E. Burk, "The importance of the excitation volume in determination of surface recombination velocity," IEEE Trans. Electron Devices, vol. ED-29, pp. 1887-1896, Dec. 1982.
48. P. Panayatatos, E. S. Yang, and W. Hwang, "Determination of the grain-boundary recombination velocity in polycrystalline silicon as a function of illumination from photoconductance measurements," Solid-State Electron., vol. 25, pp. 417-422, May 1982.
49. T. Daud and L. J. Cheng, "Surface recombination velocity measurement for silicon solar cells," in Rec. 15th Photovoltaic Specialists Conf., IEEE Cat. No. 81CH1644-4, pp. 1183-1188, 1981.
50. C. Donolato, "An analytical model of SEM and STEM charge collection images of dislocations in thin semiconductor layers," Phys. Stat. Sol. (A), vol. 65, 649-658, June 1981.
51. O. von Roos, "Analysis of the interaction of an electron beam with a solar cell-I," Solid-State Electron., vol. 21, pp. 1063-1067, Aug. 1978.
52. W. van Roosbroeck, "Injected current carrier transport in a semi-infinite semiconductor and the determination of lifetimes and surface recombination velocities," J. Appl. Phys., vol. 26, pp. 380-391, Apr. 1955.

53. C. Donolato, "Theory of beam induced current characterization of grain boundaries in polycrystalline solar cells," J. Appl. Phys., vol. 54, pp. 1314-1322, Mar. 1983.
54. T. E. Everhart and P. H. Hoff, "Determination of kilovolt electron energy dissipation vs. penetration distance in solid materials," J. Appl. Phys., vol. 42, pp. 5837-5846, Dec. 1971.
55. R. Shimizu, T. Ikuta, T. E. Everhart, and W. J. de Vore, "Experimental and theoretical study of energy dissipation profiles of keV electrons in polymethylmethacrylate," J. Appl. Phys., vol. 46, pp. 1581-1584, Apr. 1975.
56. D. B. Wittry, "Resolution of electron probe microanalyzers," J. Appl. Phys., vol. 29, pp. 1543-1548, Nov. 1958.
57. E. F. Beckenbach, Modern Mathematics for the Engineer, New York: McGraw-Hill Book Company, Inc., 1956.
58. J. B. Scarborough, Numerical Mathematical Analysis, London: Oxford University Press, 1950.
59. H. J. Queisser, K. Hubner, and W. Shockley, "Diffusion along small-angle grain boundaries in silicon," Phys. Rev., vol. 123, pp. 1245-1254, Aug. 1961.
60. K. V. Ravi, Imperfections and Impurities in Semiconductors, New York: Wiley, 1981.
61. J. Mandelkorn and J. H. Lamneck, Jr., "Simplified fabrication of back surface electric field silicon cells and novel characteristics of such cells," in Rec. 9th IEEE Photovoltaic Specialists Conf., IEEE Cat. No. 72CH0613-OED, 1972.
62. J. C. M. Hwang, P. S. Ho, J. E. Lewis, and D. R. Campbell, "Grain boundary diffusion of aluminum in polycrystalline silicon films," J. Appl. Phys., vol. 51, pp. 1576-1581, Mar. 1980.
63. W. A. Orr and M. Arienzo, "Investigation of polycrystalline silicon back surface field solar cells," IEEE Trans. Electron Devices, vol. ED-29, pp. 1151-1155, Aug. 1982.
64. J. del Alamo, J. Eguren, and A. Luque, "Operating limits of Al-alloyed high-low junctions for BSF solar cells," Solid-State Electron., vol. 24, pp. 415-420, May 1981.
65. R. D. Nasby, C. M. Garner, H. T. Weaver, F. W. Sexton, and J. L. Rodriguez, "Characterization of $p^{+}nn^{+}$ silicon concentrator solar cells," in Rec. 15th Photovoltaic Specialists Conf., IEEE Cat. No. 81CH1644-4, pp. 132-135, 1981.
66. K. Nakamura, M.-A. Nicolet, J. W. Mayer, R. J. Blattner, and C. A. Evans, Jr., "Interactions of Al layers with polycrystalline Si," J. Appl. Phys., vol. 46, pp. 4678-4684, Nov. 1975.

67. S. K. Agarwal, Harsh, S. C. Jain, P. DePauw, R. Mertens, and R. van Overstraeten, "Effect of injection level on minority-carrier lifetime," in Rec. 16th Photovoltaic Specialists Conf., IEEE Cat. No. 82CH1821-8, pp. 366-370, 1982.
68. A. Neugroschel, F. A. Lindholm, and C. T. Sah, "A method for determining the emitter and base lifetimes in p-n junctions diodes," IEEE Trans. Electron Devices, vol. ED-24, pp. 662-671, June 1977.
69. A. S. Grove, Physics and Technology of Semiconductor Devices, New York: Wiley, 1967.
70. L. L. Kazmerski, P. E. Russell, P. J. Ireland, C. R. Herrington, J. R. Dick, R. J. Matson, and K. M. Jones, "Grain boundaries in silicon solar cells," in Rec. 16th Photovoltaic Specialists Conf., IEEE Cat. No. 82CH1821-8, pp. 622-626, 1982.
71. S. Krishna, "The influence of post-emitter processing on the current gain of bipolar transistors," IEEE Trans Electron Devices, vol. ED-29, pp. 430-435, Mar. 1982.
72. R. D. Thompson and K. N. Tu, "Low temperature gettering of Cu, Ag, and Au across a wafer of Si by Al," Appl. Phys. Lett., vol. 41, pp. 440-442, Sept. 1982.
73. A. J. Learn, "Evolution of current status of aluminum metallization," J. Electrochem. Soc., vol. 123, pp. 894-906, June 1976.
74. R. D. Stoeva, A. L. Popova, and V. F. Gancheva, "Effect of temperature treatment on Al/Si and Al/poly-Si contacts," C. R. Acad. Bulg. Sci., (Bulgaria), vol. 34, pp. 977-980, July 1981.
75. J. Dietl, D. Helmreich, and E. Sirtl, Solar Silicon, Private communication: E. Elkin, Wacker Siltronic Corporation, Portland, Oregon.
76. R. N. Legge and N. G. Sakiotis, "Effects of oxygen impurities upon solar cell performance," in Rec. 15th Photovoltaic Specialists Conf., IEEE Cat. No. 81CH1644-4, pp. 1428-1431, 1981.
77. A. Goetzberger and W. Shockley, "Metal precipitates in silicon p-n junctions," J. Appl. Phys., vol. 31, pp. 1821-1824, Oct. 1960.
78. J. E. Lawrence, "Metallographic analysis of gettered silicon," AIME Trans. Met. Soc., vol. 242, pp. 484-489, Mar. 1968.
79. S. W. Ing., Jr., R. E. Morrison, L. L. Alt, and R. W. Aldrich, "Gettering of metallic impurities from planar silicon diodes," J. Electrochem. Soc., vol. 110, pp. 533-537, June 1963.
80. J. L. Lambert and M. Reese, "The gettering of gold and copper from silicon," Solid-State Electron, vol. 11, pp. 1055-1061, Nov. 1968.

81. J. G. Fossum and D. S. Lee, "A physical model for the dependence of carrier lifetime on doping density in nondegenerate silicon," Solid-State Electron., vol. 25, pp. 741-747, Aug. 1982.
82. V. Cazarra and P. Zunino, "Influence of oxygen on silicon resistivity," J. Appl. Phys., vol. 51, pp. 4206-4211, Aug. 1980.
83. L. Jastrzebski, "Origin and control of material defects in silicon VLSI technologies: an overview," IEEE Trans. Electron Devices, vol. ED-29, pp. 475-487, Apr. 1982.
84. J. R. Davis, Jr., A. Rohatgi, R. H. Hopkins, P. D. Blais, P. Rai-Chaudhury, J. R. McCormick, and H. C. Mollenkopf, "Impurities in silicon solar cells," IEEE Trans. Electron Devices, vol. ED-27, pp. 677-687, Apr. 1980.
85. V. G. Weizer, M. P. Godlewski, and R. J. Trivisonno, "The effect of minority carrier mobility variations on solar cell spectral response," in Rec. 15th Photovoltaic Specialists Conf., IEEE Cat. No. 81CH1644-4, pp. 892-897, 1981.
86. D. B. Holt, Quantitative Scanning Electron Microscopy, New York: Academic Press, 1974.
87. J. G. Fossum and M. A. Shibib, "A minority-carrier transport model for polysilicon contacts to silicon bipolar devices, including solar cells," in Rec. of Int. Electron Devices Meeting, IEEE Cat. No. 80CH1616-2, pp. 280-283, 1980.
88. L. Fox, Numerical solution of two-point boundary value problems, New York: Pergamon Press, 1962.
89. D. Young, "Iterative methods for solving partial difference equations of elliptic type," Trans. Amer. Math. Soc., vol. 76, pp. 92-111, Jan. 1954.

BIOGRAPHICAL SKETCH

Ravishankar Sundaresan was born in Kumbakonam, India, on September 25, 1955. In June 1978 he received his B.E. degree in electronics and communication engineering from the University of Madras, India. He graduated with an M.E. degree in electrical engineering from the University of Florida in March 1981. Since 1981 he has been working towards his Ph.D. degree in electrical engineering.

He has been working as a Graduate Teaching and Research Assistant at the University of Florida. His research interests are in the area of semiconductor devices and integrated circuits.

He is a member of Eta Kappa Nu and the Institute of Electrical and Electronics Engineers.

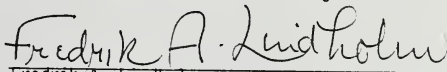
I certify that I have read this study and that in my opinion it conforms to acceptable standards of scholarly presentation and is fully adequate, in scope and quality, as a dissertation for the degree of Doctor of Philosophy.


Jerry G. Fossum, Chairman
Professor of Electrical Engineering

I certify that I have read this study and that in my opinion it conforms to acceptable standards of scholarly presentation and is fully adequate, in scope and quality, as a dissertation for the degree of Doctor of Philosophy.


Dorothea E. Burk, Co-Chairman
Assistant Professor of Electrical Engineering

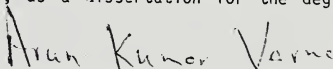
I certify that I have read this study and that in my opinion it conforms to acceptable standards of scholarly presentation and is fully adequate, in scope and quality, as a dissertation for the degree of Doctor of Philosophy.


Fredrik A. Lindholm
Professor of Electrical Engineering

I certify that I have read this study and that in my opinion it conforms to acceptable standards of scholarly presentation and is fully adequate, in scope and quality, as a dissertation for the degree of Doctor of Philosophy.


Arnost Neugroschel
Professor of Electrical Engineering

I certify that I have read this study and that in my opinion it conforms to acceptable standards of scholarly presentation and is fully adequate, in scope and quality, as a dissertation for the degree of Doctor of Philosophy.


Arun K. Varma
Professor of Mathematics

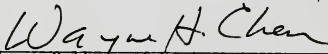
I certify that I have read this study and that in my opinion it conforms to acceptable standards of scholarly presentation and is fully adequate, in scope and quality, as a dissertation for the degree of Doctor of Philosophy.



Paul H. Holloway
Professor of Materials Science
and Engineering

This dissertation was submitted to the Graduate Faculty of the College of Engineering and to the Graduate School, and was accepted as partial fulfillment of the requirements for the degree of Doctor of Philosophy.

December 1983



Dean, College of Engineering

Dean, Graduate School

